



저작자표시-비영리-변경금지 2.0 대한민국

이용자는 아래의 조건을 따르는 경우에 한하여 자유롭게

- 이 저작물을 복제, 배포, 전송, 전시, 공연 및 방송할 수 있습니다.

다음과 같은 조건을 따라야 합니다:



저작자표시. 귀하는 원저작자를 표시하여야 합니다.



비영리. 귀하는 이 저작물을 영리 목적으로 이용할 수 없습니다.



변경금지. 귀하는 이 저작물을 개작, 변형 또는 가공할 수 없습니다.

- 귀하는, 이 저작물의 재이용이나 배포의 경우, 이 저작물에 적용된 이용허락조건을 명확하게 나타내어야 합니다.
- 저작권자로부터 별도의 허가를 받으면 이러한 조건들은 적용되지 않습니다.

저작권법에 따른 이용자의 권리는 위의 내용에 의하여 영향을 받지 않습니다.

이것은 [이용허락규약\(Legal Code\)](#)을 이해하기 쉽게 요약한 것입니다.

[Disclaimer](#)

Ph.D Thesis
박사 학위논문

The role of imide electrolytes on the interfacial
reactions with electrodes for lithium ion batteries
and lithium metal batteries

Kisung Park(박 기 성 朴 基 成)

Department of
Energy Science & Engineering

DGIST

2020

The role of imide electrolytes on the interfacial reactions with electrodes for lithium ion batteries and lithium metal batteries

Advisor: Professor Hochun Lee
Co-advisor: Professor Hyun-Kon Song

by

Kisung Park
Department of Energy Science & Engineering
DGIST

A thesis submitted to the faculty of DGIST in partial fulfillment of the requirements for the degree of Doctor of Philosophy in the Department of Energy Science & Engineering. The study was conducted in accordance with Code of Research Ethics¹

12. 30. 2019

Approved by

Professor Hochun Lee (Advisor)	(signature)
Professor Hyun-Kon Song (Co-Advisor)	(signature)

¹ Declaration of Ethical Conduct in Research: I, as a graduate student of DGIST, hereby declare that I have not committed any acts that may damage the credibility of my research. These include, but are not limited to: falsification, thesis written by someone else, distortion of research findings or plagiarism. I affirm that my thesis contains honest conclusions based on my own careful research under the guidance of my thesis advisor.

The role of imide electrolytes on the interfacial
reactions with electrodes for lithium ion batteries
and lithium metal batteries

Kisung Park

Accepted in partial fulfillment of the requirements
for the degree of Doctor of Philosophy.

12. 30. 2019

Head of Committee Prof. Seungtae Hong (signature)

Committee Member Prof. Hochun Lee (signature)

Committee Member Prof. Yongmin Lee (signature)

Committee Member Prof. Hongkyung Lee (signature)

Committee Member Prof. Hyun-Kon Song (signature)

Ph.D/ES
201434006

박 기 정. Kisung Park. The role of imide electrolytes on the interfacial reactions with electrodes for lithium ion batteries and lithium metal batteries. Department of Energy Science & Engineering. 2020. 94p. Advisors Prof. Hochun Lee, Co-Advisors Prof. Hyun-Kon Song

ABSTRACT

This study investigates the availability of lithium (Li) imide salt based electrolytes for lithium ion batteries (LIBs) and lithium metal batteries (LMBs) and the role of imide electrolytes on the interfacial reactions with electrodes. Li imide salts such as lithium bis(fluorosulfonyl)imide (LiFSI) and lithium bis(trifluoromethanesulfonyl)imide (LiTFSI) are the promising candidate for LIBs and LMBs as compared with the widely used Li salt, lithium hexafluorophosphate (LiPF_6) due to its improved solubility, thermal stability, HF contamination resistivity and comparable ionic conductivity.

I firstly study the suitability of Li imide electrolytes in LIBs which consist of two electrodes, Li metal oxide cathode and graphite anode. In terms of graphite/electrolyte, it has been reported that Li imide electrolyte presents slightly/far better electrochemical performances at ambient/elevated temperature, resulting from reduced internal charge transfer resistance and thermally stable solid electrolyte interphase (SEI) formation on graphite/electrolyte interface.

However, a severe corrosion issue of aluminum (Al) cathode current collector is a bottleneck for the use of Li imide salt with cathodes. Through a systematic comparison of Al corrosion behavior in the electrolyte with Li imide salt and various borate Li salt additives, Al corrosion is largely suppressed by the addition of those additives and the inhibition ability is revealed to be in the following order: lithium difluoro(oxalato)borate (LiDFOB) > lithium tetrafluoroborate (LiBF_4) \approx LiPF_6 > lithium bis(oxalato)borate. Particularly, the corrosion inhibition ability of Li imide electrolyte with LiDFOB additive is comparable to Al corrosion-free LiPF_6 electrolyte. As evidenced by X-ray photoelectron spectroscopy (XPS), such superior inhibition ability is attributed to the formation of a passive layer which consists of Al-F, Al_2O_3 , and B-O species on

Al/electrolyte interface. A LiCoO₂/graphite cell with 0.8 M LiFSI+0.2 M LiDFOB electrolyte exhibits a rate capability comparable to a cell with 1 M LiPF₆ solution, whereas a cell with 0.8 M LiFSI solution without LiDFOB suffers from poor power performance resulting from severe Al corrosion.

Li imide electrolytes feature comparable/better advantages in LIBs by prevention of Al corrosion. However, it is still insufficient to satisfy an urgent need in energy market demands. Thus, Li metal anode can possibly be a good candidate of graphite owing to its high theoretical capacity and low redox potential after success of addressing issues such as low Li coulombic efficiency (CE) and dendrite formation. Recently, Li imide electrolytes were introduced with a non-coordinating fluorinated ether. However, very little is known about the performance of LHCEs under harsh temperature conditions. I investigate glyme-based LHCE over a wide temperature range (5–60 °C) with a focus on the beneficial role of the fluorinated ether. Compared to 4 M LiFSI dimethoxyethane (gHCE), 1 M LiFSI dimethoxyethane/fluorinated ether (gLHCE) displays improved physicochemical properties, good wettability toward polyethylene separators, and non-flammability due to the advantageous character of the fluorinated ether. In-depth analysis confirms that in gLHCE, most FSI-anions exist as contact ion pairs and agglomerates, leading to an inorganic-rich solid electrolyte interphase on the Li anode that mitigates the side reactions with the electrolyte and facilitates the interfacial charge transport. The formidable advantages of gLHCE enable an excellent Li cycling behavior and long-term stability of FeS₂/Li and anode-free LiFePO₄/Cu cells over 5–60 °C.

Lastly, the superior rate capability of HCEs and LHCEs is scrutinized in comparison with conventional diluted electrolyte (DE). In LiCoO₂/Li rate test, LiFSI-DMC based DE, HCE, and LHCE are compared at various discharge rates from 0.2C to 20C. Although discharge capacity retentions of LiCoO₂/Li cells with HCE and LHCE are higher than the capacity retention of DE up to 10C, the capacity retention of HCE is drastically decreased at 15C, and eventually the capacity retention of HCE becomes lower than DE. Meanwhile, LHCE features great capacity retention after 15C as compared with HCE. The electrochemical impedance spectroscopy (EIS) study reveals that HCE enables the lower charge transfer resistance (R_{ct}) at LiCoO₂/electrolyte interface. However, during ultrafast discharge, the ohmic resistance and ion transport resistance in the electrode pores (R_{sol} and R_{ion}) and concentration overpotential (η_{conc}) affect the cell performance to a higher extent

than the discharge process at low/moderate rates. Thus, LHCE is found to exhibit the highest rate capability due to the facile charge transfer (from lower activation energy for charge transfer and lower viscosity) and better mass transport (from better ionic conductivity and quite lower viscosity than HCE).

This study indicates that the availability of electrolytes for batteries is not determined by only its physicochemical natures, but it should be considered comprehensively with the nature of electrodes and interphase properties at electrode/electrolyte interface which can affect ionic and charge transport.

Keywords: lithium bis(fluorosulfonyl)imide (LiFSI), lithium ion batteries, lithium metal batteries, passive layer, solid electrolyte interphase (SEI), interface

List of contents

Abstract	i
List of contents	iv
List of tables	viii
List of figures	ix
I. Introduction	1
II. Theory	
2.1 Electrochemistry	6
2.1.1 Electromotive force	6
2.1.2 Electrode potential	6
2.1.3 Energy storage	7
2.2 Battery theory	8
2.3 Lithium batteries	9
2.3.1 Anode materials	11
2.3.2 Electrolytes	12
2.3.3 Solid Electrolyte Interphase (SEI)	13
2.3.4 Additives	14
2.3.5 Cathode materials	14
2.4 References	15

III. Comparative study on lithium borates as corrosion inhibitors of aluminum current collector
in lithium bis(fluorosulfonyl)imide electrolytes

3.1 Introduction	17
3.2 Experimental	
3.2.1 Chemicals	19
3.2.2 Electrochemical experiments	19
3.2.3 XPS	21
3.2.4 LiCoO ₂ cell tests.....	21
3.2.5 EIS	22
3.3 Results and discussion	
3.3.1 Inhibitive effects of borate additives on Al corrosion in LiFSI electrolytes ...	22
3.3.2 XPS study on surface composition of Al electrodes	26
3.3.3 LiCoO ₂ cell performances.....	31
3.3.4 Internal resistance analysis of LiCoO ₂ cell.....	33
3.3.5 Discussion.....	36
3.4 Conclusions	38
3.5 References	39

IV. Wide-temperature operation of lithium metal batteries enabled by localized high-
concentration electrolytes

4.1 Introduction	44
4.2 Experimental	

4.2.1 Chemicals	45
4.2.2 Physicochemical properties	45
4.2.3 Electrochemical and cell tests	46
4.2.4 Microscopy and spectroscopy	47
4.3 Results and discussion	
4.3.1 Physicochemical properties	48
4.3.2 Thermal and electrochemical stability	50
4.3.3 Electrolyte optimization for Li cycling	51
4.3.4 Li cycling performances at various conditions	53
4.3.5 Surface and ionic species analysis	57
4.3.6 FeS ₂ /Li and anode free LFP cell performances	60
4.3.7 Internal resistance analysis	65
4.3.8 Comparison	68
4.4 Conclusions	69
4.5 References	70
V. Analysis of rate performance of high-concentration electrolytes and localized high-concentration electrolytes	
5.1 Introduction	75
5.1.1 Overpotential	77
5.2 Experimental	
5.2.1 Chemicals	79

5.2.2 Methodology.....	80
5.3 Results and discussion	
5.3.1 Physicochemical properties	83
5.3.2 Al corrosion inhibition.....	84
5.3.3 LCO/Li rate performance.....	85
5.3.4 Internal resistance and overpotential.....	86
5.4 Conclusions	91
5.5 References	92
Summary (in Korean)	93

List of tables

Table 2.1 Properties of commonly used solvents in LIBs. All data from the handouts of the “Electrochemistry” class.

Table 3.1 Fitted parameter values for the impedance spectra of Fig. 8

Table 4.1 Contact angle and surface tension of the electrolytes.

Table 4.2 Atomic composition, determined from XPS spectra, of the Li electrodes collected from the Li/Cu cells cycled 30 times in gHCE and gLHCE.

Table 4.3 Fitted resistance values from Nyquist plots of the Li/Li cells measured at a SOC 50 shown in Fig. 4.16.

Table 4.4 Comparison of the Li cycle test, ionic conductivity, viscosity, non-flammability, and electrochemical stability of various LHCEs and HCEs. The values of HCEs are denoted in parenthesis.

Table 5.1 Physicochemical properties of LiFSI-AN electrolytes at 30 °C^[1].

Table 5.2 Explanation of types of overpotential, adapted from the handouts of the “Electrochemistry” class.

Table 5.3 Ionic conductivity and viscosity of DE, HCE, and LHCE at 25 °C.

Table 5.4 The ratio of $i_{o,HCE}$ to $i_{o,LHCE}$ from R_{ct} .

Table 5.5 The ratio of $i_{o,HCE}$ to $i_{o,LHCE}$ from E_a^{ct} of LCO/LCO symmetric cells with HCE and LHCE, viscosity, and EMF of the concentration cells. i_o ratio is obtained by a product of all factor ratios.

List of figures

Fig. 2.1 A general overview of a galvanic cell.

Fig. 2.2 Comparison of the different battery technologies in terms of volumetric and gravimetric energy density.

Fig. 2.3 Schematic of a general Li-ion battery cell with cathode (ex. LiCoO₂), anode (ex. C₆) and electrolyte. The electrons in the external circuit is driven by a voltage source on charge and performs work on discharge. Adapted from the handouts of the “Electrochemistry” class.

Fig. 2.4 Voltage versus capacity for cathode- and anode-electrolyte materials presently used or under serious considerations for the next generation of rechargeable Li-based cells^[2].

Fig. 3.2 (a) CVs of Al electrodes at the 1st cycle in LiFSI, LiFSI+BF₄, LiFSI+BOB, LiFSI+DFOB, (b) expanded view of (a), and (c) expanded view of (b). The CVs of LiFSI+PF₆ and LiPF₆ are also presented for comparison.

Fig. 3.3 CVs of Al electrodes at the first, second, and fifth cycles in (a) LiPF₆ and (b) LiFSI+DFOB.

Fig. 3.4 (a) Chronoamperograms of Al electrodes in LiFSI+BF₄, LiFSI+BOB, LiFSI+DFOB, LiFSI+PF₆, and LiPF₆ and (b) expanded view of (a). The potential was stepped from OCV to 4.8 V (vs. Li/Li⁺) at 45 °C.

Fig. 3.5 Al_{2p} XPS spectra for Al electrodes cycled in (a) LiFSI, (b) LiFSI+BF₄, (c) LiFSI+BOB, and (d) LiFSI+DFOB. The Al electrodes were cycled two times over 3–6 V (vs. Li/Li⁺) before XPS measurements. The depth profiles with increasing sputtering time (20–100

s) are compared.

Fig. 3.6 Al_{2p} XPS spectra for Al electrode cycled in LiFSI+DFOB for longer etching time (100–500 s). Bare Al peak becomes discernable only after 200 s etching.

Fig. 3.7 B_{1s} XPS spectra for Al electrodes cycled in (a) LiFSI, (b) LiFSI+BF₄, (c) LiFSI+BOB, and (d) LiFSI+DFOB. The Al electrodes were cycled two times over 3–6 V (vs. Li/Li⁺) before XPS measurements. The depth profiles with increasing sputtering time (20–100 s) are compared.

Fig. 3.8 Schematic diagram of passive layer formation on an Al electrode cycled in (a) LiFSI+BF₄ or LiFSI+BOB and (b) LiFSI+DFOB.

Fig. 3.9 Ionic conductivities for LiFSI, LiFSI+DFOB, and LiPF₆ measured over 10–60 °C.

Fig. 3.10 Rate performances of LiCoO₂/graphite cells with LiFSI, LiFSI+DFOB, and LiPF₆ (a) specific discharge capacities at various C-rates and (b) cell voltage profiles at 0.1 C and 2 C discharge currents.

Fig. 3.11 Electrochemical impedance spectra of (a) LiCoO₂/LiCoO₂ symmetric cell with LiFSI, LiFSI+DFOB, and LiPF₆, and (b) equivalent circuit employed for the fitting of impedance spectra. The experimental spectra are denoted with circles and the best-fitted results using the equivalent circuit with solid lines.

Fig. 3.12 CVs of Al electrodes at the first cycle in 0.8 M LiFSI+0.03 M LiDFOB (black), 0.8 M LiFSI+0.07M LiDFOB (red), and 0.8 M LiFSI+0.2 M LiDFOB (blue) in EC/DEC (3/7, v/v).

Fig. 4.1 (a) Ionic conductivities and (b) viscosities of gLHCE and gHCE at various tempera-

tures. Photos of (c) gHCE and (d) gLHCE on a PE separator. Photos of a glass filter soaked with (e) gHCE and (f) gLHCE after the flame test.

Fig. 4.2 Vogel-Tammann-Fulcher (VTF) plots of (a) Ionic conductivity and (b) viscosity of gHCE and gLHCE. Solid lines denote the best-fitting results of the VTF equation.

Fig. 4.3 (a) Linear sweep voltammograms in an anodic region on a Pt working electrode. (b) Chronoamperograms on an Al working electrode with an applied potential of 4.8 V (vs. Li/Li⁺).

Fig. 4.4 The Li CE of the Li/Cu cells cycled in (a) various glymes with TTE and (b) fluorinated ethers with DME. Li deposition capacity was 1.0 mAh cm⁻² with a current density of 0.5 mA cm⁻². The chemical structure of (c) DME, diglyme, triglyme and (d) fluorinated ethers: 1,1,2,2-tetrafluoroethyl 2,2,3,3-tetrafluoropropyl ether (TTE), 1,1,2,2-tetrafluoroethyl 2,2,2-trifluoroethyl ether (TTrE), 1,1,2,2-tetrafluoroethyl 2,2,3,3,4,4,5,5-octatetrafluoropentyl ether (TOE), and bis(2,2,2-trifluoroethyl) ether (BTFE). All the electrolytes contain 1 M LiFSI.

Fig 4.5 (a) The Li CE and (b) accumulated Coulombic inefficiency of the Li/Cu cells cycled in DME/TTE with the volume ratio from 1:1 to 1:4. Li deposition capacity was 1.0 mAh cm⁻² with a current density of 0.5 mA cm⁻². All the electrolytes contain 1 M LiFSI.

Fig. 4.6 Coulombic efficiency (CE) of Li/Cu cells at 25 °C cycled with a current density of (a) 0.2 mA cm⁻² and (b) 2.0 mA cm⁻². CE of the Li/Cu cells cycled at (c) 5 °C and (d) 60 °C with a current density of 0.1 mA cm⁻². The Li deposition capacity was 0.5 mAh cm⁻². The cell with gHCE failed during the 135th cycle at 5 °C and during the 132nd cycle at 60 °C.

Fig. 4.7 Accumulated Coulombic inefficiency of the Li/Cu cells cycled at 25 °C with a current

density of (a) 0.2 mA cm^{-2} , (b) at 25°C with 2.0 mA cm^{-2} , (c) at 5°C with 0.1 mA cm^{-2} , and (d) at 60°C with 0.1 mA cm^{-2} . Li deposition capacity was 0.5 mAh cm^{-2} . The cell with gHCE failed during the 135th cycle at 5°C and during the 132nd cycle at 60°C .

Fig. 4.8 Voltage profiles at the 1st, 50th, and 100th cycle in the Li/Cu cells: (a) gLHCE and (b) gHCE. Overpotential difference was defined as the voltage difference at a normalized capacity of 50%.

Fig. 4.9 (a) Voltage profiles of the Li/Li cells cycled 600 times in gHCE and gLHCE. Li deposition/dissolution capacity was 0.5 mAh cm^{-2} with a current density of 1.0 mA cm^{-2} (2 C). (b) Enlarged region of the voltage profiles for the last 10 cycles.

Fig. 4.10 SEM images of the Li electrodes collected from Li/Cu cells cycled 30 times in (a) gHCE and (b) gLHCE. The Li deposition capacity was 1.0 mAh cm^{-2} with a current density of 0.5 mA cm^{-2} .

Fig. 4.11 (a) C_{1s} , (b) F_{1s} , and (c) S_{2p} XPS spectra of the Li electrodes collected from the Li/Cu cells cycled 30 times in gHCE and gLHCE. The Li deposition capacity was 1.0 mAh cm^{-2} with a current density of 0.5 mA cm^{-2} . Raman spectra of (d) gHCE and (e) gLHCE. (f) Fractional composition of the ionic species. The ionic speciation of 1 M LiFSI DME is also presented for comparison.

Fig. 4.12 Possible scheme of the participation of ionic species in the SEI formation. The presence of TTE in gLHCE increases the population of CIP and AGG, resulting in more FSI-driven SEI formation.

Fig. 4.13 Discharge capacities at the 4th and 100th cycle of the (a) FeS_2/Li and (b) LFP/Cu cells

with gHCE and gLHCE at 5 °C, 25 °C, and 60 °C cycling. Discharge capacities of the (c) FeS₂/Li and (d) LFP/Cu cells with gHCE and gLHCE at discharge rates in the range of 0.1–5 C at 25 °C.

Fig. 4.14 Specific capacity of FeS₂/Li cells with gHCE and gLHCE at (a) 5 °C, (c) 25 °C, and (e) 60 °C. Voltage profiles at 4th and 100th cycle for the FeS₂/Li cells with gHCE and gLHCE at (b) 5 °C, (d) 25 °C, and (f) 60 °C. Cycling at 25 °C was performed at a 0.2 C constant current between 1.0 and 2.6 V. Cycling at 5 °C and 60 °C was performed at a 0.5 C constant current between 1.0 and 2.6 V after the cells were cycled three times at 25 °C with a 0.2 C constant current.

Fig. 4.15 Specific capacity of the LFP/Cu cells with gHCE and gLHCE at (a) 5 °C, (c) 25 °C, and (e) 60 °C. Voltage profiles at the 4th and 100th (50th) cycles for the LFP/Cu cells with gHCE and gLHCE at (b) 5 °C, (d) 25 °C, and (f) 60 °C. Cycling at 25 °C was performed at a 0.2 C constant current between 2.8 and 3.8 V. Cycling at 5 °C and 60 °C was performed at a 0.5 C constant current between 2.8 and 3.8 V after the cells were cycled three times at 25 °C with a 0.2 C constant current.

Fig 4.16 Nyquist plots of the Li/Li cells with (a) gHCE and (b) gLHCE over 5–55 °C measured at a state-of-charge (SOC) 50. The Li/Li cells were cycled 3 times before the impedance measurements. (c) An equivalent circuit for fitting of impedance data. (d) Arrhenius plots of the charge transfer resistance (R_{ct}) for Li/Li cells with gHCE and gLHCE. Li deposition/dissolution capacity for the formation process was 1.0 mAh cm⁻² at a current density of 0.2 mA cm⁻². The experimental spectra were plotted as solid dots and the best-fitted data were solid lines. The pa-

parameters, R_S , R_{SEI} , R_{ct} , Q_{SEI} , Q_{ct} , and Q_D were determined by the curve fitting with the equivalent circuit (Fig. 4.16c). Q_{SEI} and Q_{ct} are the constant phase elements (CPEs) coupled with R_{SEI} and R_{ct} , respectively. Q_D represents the finite diffusion of a Warburg element [45, 46].

Fig. 5.1 Charge/discharge profiles of graphite/Li cells with 4.2 M LiTFSI-AN solution. The charge/discharge rate is 0.1C^[1].

Fig. 5.2 (a) Lithium intercalation voltage profiles of graphite/Li cells at various C-rates from 0.05C to 2C. (b) Lithium deintercalation capacity of graphite/Li cells at various C-rates from 0.05C to 5C. The current density during charge and discharge was set to the same C-rate and the cells were charged/discharged with only constant current mode^[1].

Fig. 5.3 Scheme for the types of resistance caused by the overpotential in the cells with porous electrodes. The ionic resistance in electrode pores (R_{ion}) should be considered in the porous electrodes^[2].

Fig. 5.4 The effect of overpotentials in the electrochemical performance of the cells, adapted from the handouts of the “Electrochemistry” class. η_{ohm} , η_{ion} , and η_{ct} affect at the early stage of discharge process due to the rapid time-scale of ionic conduction and charge transfer reactions while η_{ct} significantly reduces the electrochemical performance at the late time of discharge process due to the cumulative concentration gradient.

Fig. 5.5 Nyquist plots of LiNiO₂ cathode symmetric cells in the conventional electrolyte at 20 °C: (a) SOC 0, and (b) SOC 50. The solid lines are the best-fitted results from the equivalent circuit^[3].

Fig. 5.6 Illustration of concentration cell configuration. Li metal immersed in DE-filled glass

tube with porous vycor tip is a reference electrode, and the other Li metal is immersed in HCE or LHCE-filled beaker as a working electrode. EMFs between two Li metals were measured by a portable digital voltmeter.

Fig. 5.7 (a) Ionic conductivities of DE, HCE, and LHCE at various temperatures. (b) Vogel-Tammann-Fulcher (VTF) plots of ionic conduction for DE, HCE, and LHCE. Solid lines denote the best-fitting results of the VTF equation.

Fig. 5.8 CVs of Al electrodes at the first, second, and third cycle in DE, HCE, and LHCE. The current density decreases in the subsequent cycles after first cycle, which indicates the passive film layer is formed on the Al electrodes.

Fig. 5.9 The discharge capacity of LCO/Li cells with DE, HCE, and LHCE at various C-rates from 0.2C to 20C.

Fig 5.10 Voltage profiles of LCO/Li cells at 0.2C, 5C, 10C, and 20C with DE, HCE, and LHCE.

Fig. 5.11 Nyquist plots of LCO/LCO symmetric cells at SOC 50 for DE, HCE, and LHCE. Left and middle are expanded view of right plot. Each resistance is described as a bar with various length and thickness in Nyquist plots and accumulated column bar graph.

Fig. 5.12 Arrhenius plots for E_a^{ct} of HCE and LHCE. The solid lines are the best-fitted result from the equivalent circuit in Fig. 4.16c.

Fig. 5.13 Voltage profiles of LCO/Li cells at 5C with DE, HCE, and LHCE using CC only and GITT method. The intermittent rest time is 20 min.

I. INTRODUCTION

Current Li-ion batteries (LIBs) are forced to achieve both higher energy density and extreme long-term stability for the reliable operation of IT devices and electric vehicles [1-4]. Most of the current LIBs are employing lithium hexafluorophosphate (LiPF₆)-based electrolytes due to high ionic conductivity, decent safety, and innate immunity to aluminum (Al) current collectors [5]. Nevertheless, LiPF₆ electrolytes are inevitably contaminated by hydrogen fluoride (HF), a byproduct of LiPF₆ hydrolysis, which facilitates metal dissolution from cathode materials [6, 7] and exacerbates unwanted side reactions at the anode side [8].

As an alternative candidate to LiPF₆, lithium bis(fluorosulfonyl)imide (LiFSI) has been reported to exhibit comparable or higher ionic conductivity to LiPF₆ while maintaining HF-free nature, which suggests that LiFSI can offer both the superior energy density and long-term stability of LIBs [9, 10]. LiFSI, however, is subjected to severe corrosion of Al current collector [10, 11], a common chronic issue of lithium imide salts [1, 12].

To mitigate Al corrosion issue of LiFSI salt, thus, I performed a systematic comparison on the inhibition effects of Li-borate (LiBF₄, LiDFOB, and LiBOB) and LiPF₆ additives on Al corrosion in LiFSI EC/DEC (3/7, v/v) solutions. Among the additives, LiDFOB was revealed to be the most efficient inhibitor of Al corrosion in LiFSI-based electrolytes. The Al corrosion behavior in 0.8 M LiFSI+0.2 M LiDFOB was determined to be comparable to that of 1 M LiPF₆ solution, an Al corrosion-immune medium. The excellent inhibition ability of LiDFOB additive was further examined using the X-ray photoelectron spectroscopy (XPS) analysis of the Al surface layer and was also confirmed through the rate capability/electrochemical impedance spectroscopy (EIS) measurements of LiCoO₂ cells.

Yet, these solutions for LiFSI electrolyte in LIBs are still insufficient to accomplish the improvement on the cell performances for rapidly increased demand on higher energy density in the batteries markets. There is an urgent need to replace current LIBs with Li metal batteries (LMBs) to exploit the high theoretical capacity (3860 mAh g⁻¹) and low redox potential (-3.0 V vs. NHE) of the Li metal anode. However, the Li anode suffers from poor cyclability due to low Coulombic efficiency (CE) and severe Li dendrite formation.

In the previous reports, high-concentration electrolytes (HCEs) containing unconventionally high salt

content were introduced to resolve the aforementioned issues of the Li anode. HCEs feature critical advantages, including enhanced electrochemical stability and dendrite-free Li deposition with high CE [13–24]. Nevertheless, HCEs face several critical issues, including high salt concentration, high material cost, and high viscosity.

Recently, localized high-concentration electrolytes (LHCEs) employing diluent co-solvents that hardly solvate Li-ions were thus introduced to address the drawbacks of HCEs [25–28]. Compared to the case with HCEs, LHCEs exhibit markedly low viscosity, which improves their ionic conductivity and wettability at ambient temperature. Despite their immense potential, LHCEs, however, have not been fully exploited. In particular, the possible benefits of LHCEs under harsh temperature conditions, which would drive LMBs closer to practical applications, are scarcely examined [25]. Moreover, the influence of the main solvent and co-solvent on the overall properties of LHCEs needs to be further elucidated.

I investigated glyme-based HCE and LHCE over the temperature range relevant to practical applications (5–60 °C). A representative HCE consisting of a glyme solvent (1,2-dimethoxyethane, DME) with 4 M LiFSI (hereinafter denoted as gHCE) [14] was employed. DME and 1,1,2,2-tetrafluoroethyl 2,2,3,3-tetrafluoropropyl ether (TTE) (1/2, v/v) with 1 M LiFSI was selected as a model LHCE (hereinafter denoted as gLHCE). It is found that compared to the case with gHCE, gLHCE enables stable Li cycling with a high Li CE at 5 °C, 25 °C, and 60 °C. As evidenced by XPS and Raman spectroscopy, the beneficial impact of gLHCE was ascribed to increased fractions of ion pairs and agglomerates, which can help to derive an inorganic-rich solid electrolyte interphase (SEI) on the Li anode. Finally, it was confirmed that gLHCE markedly improves the long-term cyclability and rate capability of FeS₂/Li and anode-free LiFePO₄ (LFP)/Cu cells over 5–60 °C.

Also, it has been reported that HCEs exhibited excellent capacity retention at high charge/discharge rate, contrast to the belief that such viscous electrolyte exhibits poor electrochemical performances as compared to the conventional electrolytes with high ionic conductivity and low viscosity. Nevertheless, the exact reason for excellent rate capability of HCEs still remains elusive.

To assess the relation between the characteristics of the electrolyte and the rate capability of cells, LiFSI-DMC DE, HCE, and LHCEs are utilized with electrochemical techniques including EIS, electromotive force

(EMF) of concentration cells, and galvanostatic intermittent titration technique (GITT).

References

- [1] S.T. Myung, Y. Hitoshi, Y.K. Sun, Electrochemical behavior and passivation of current collectors in lithium-ion batteries, *J. Mater. Chem.* 21 (2011) 9891–9911.
- [2] J.M. Tarascon, M. Armand, Issues and challenges facing rechargeable lithium batteries, *Nature* 414 (2001) 359–367.
- [3] J.M. Tarascon, M. Armand, Building better batteries, *Nature* 451 (2008) 652–657.
- [4] Y.K. Sun, S.T. Myung, B.C. Park, J. Prakash, I. Belharouak, K. Amine, High-energy cathode material for long-life and safe lithium batteries, *Nat. Mater.* 8 (2009) 320–324.
- [5] M. Morita, T. Shibata, N. Yoshimoto, M. Ishikawa, Anodic behavior of aluminum in organic solutions with different electrolytic salts for lithium ion batteries, *Electrochim. Acta* 47 (2002) 2787–2793.
- [6] D.H. Jang, S.M. Oh, Electrolyte effects on spinel dissolution and cathodic capacity losses in 4 V Li/Li_xMn₂O₄ rechargeable cells, *J. Electrochem. Soc.* 144 (1997) 3342–3348.
- [7] J. Vetter, P. Novak, M.R. Wagner, C. Veit, K.C. Moller, J.O. Besenhard, M. Winter, M. Wohlfahrt-Mehrens, C. Vogler, A. Hammouche, Ageing mechanisms in lithium-ion batteries, *J. Power Sources* 147 (2005) 269–281.
- [8] E. Wang, D. Ofer, W. Bowden, N. Iltchev, R. Moses, K. Brandt, Stability of lithium ion spinel cells, *J. Electrochem. Soc.* 147 (2000) 4023–4028.
- [9] A. Guerfi, S. Duchesne, Y. Kobayashi, A. Vijn, K. Zaghbi, LiFePO₄ and graphite electrodes with ionic liquids based on bis(fluorosulfonyl)imide (FSI)⁻ for Li-ion batteries, *J. Power Sources* 175 (2008) 866–873.
- [10] L. Li, S. Zhou, H. Han, H. Li, J. Nie, M. Armand, Z. Zhou, X. Huang, Transport and electrochemical properties and spectral features of non-aqueous electrolytes containing LiFSI in linear carbonates solvents, *J. Electrochem. Soc.* 158 (2011) A74–A82.

- [11] A. Abouimrane, J. Ding, I.J. Davidson, Liquid electrolytes based on lithium bis-fluorosulfonyl imide salt: Aluminum corrosion studies and lithium ion battery investigations, *J. Power Sources* 189 (2009) 693–696.
- [12] E. Kramer, S. Passerini, M. Winter, Dependency of aluminum collector corrosion in lithium ion batteries on the electrolyte solvent, *ECS Electrochem. Lett.* 1 (2012) C9–C11.
- [13] S.-K. Jeong, H.-Y. Seo, D.-H. Kim, H.-K. Han, J.-G. Kim, Y. B. Lee, Y. Iriyama, T. Abe, Z. Ogumi, Suppression of dendritic lithium formation by using concentrated electrolyte solutions, *Electrochem. Commun.* 10 (2008) 635–638.
- [14] J. Qian, W. A. Henderson, W. Xu, P. Bhattacharya, M. Engelhard, O. Borodin, J.-G. Zhang, High rate and stable cycling of lithium metal anode, *Nat. Commun.* 6 (2015) 6362.
- [15] Q. Ma, Z. Fang, P. Liu, J. Ma, X. Qi, W. Feng, J. Nie, Y.-S. Hu, H. Li, X. Huang, L. Chen, Z. Zhou, Improved cycling stability of lithium-metal anode with concentrated electrolytes based on lithium (fluorosulfonyl)(trifluoromethanesulfonyl)imide, *ChemElectroChem* 3 (2016) 531–536.
- [16] Z. Fang, Q. Ma, P. Liu, J. Ma, Y.-S. Hu, Z. Zhou, H. Li, X. Huang, L. Chen, Novel concentrated Li[(FSO₂)(n-C₄F₉SO₂)N]-based ether electrolyte for superior stability of metallic lithium anode, *ACS Appl. Mater. Interfaces* 9 (2017) 4282–4289.
- [17] Z. Zeng, V. Murugesan, K. S. Han, X. Jiang, Y. Cao, L. Xiao, X. Ai, H. Yang, J.-G. Zhang, M. L. Sushko, J. Liu, Non-flammable electrolytes with high salt-to-solvent ratios for Li-ion and Li-metal batteries, *Nat. Energy* 3 (2018) 674–681.
- [18] P. Zhang, J. Zhu, M. Wang, N. Imanishi, O. Yamamoto, Lithium dendrite suppression and cycling efficiency of lithium anode, *Electrochem. Commun.* 87 (2018) 27–30.
- [19] S. Jiao, X. Ren, R. Cao, M. H. Engelhard, Y. Liu, D. Hu, D. Mei, J. Zheng, W. Zhao, Q. Li, N. Liu, B. D. Adams, C. Ma, J. Liu, J.-G. Zhang, W. Xu, Stable cycling of high-voltage lithium metal batteries in ether electrolytes, *Nat. Energy* 3 (2018) 739–746.
- [20] X. Fan, L. Chen, X. Ji, T. Deng, S. Hou, J. Chen, J. Zheng, F. Wang, J. Jiang, K. Xu, C. Wang, Highly fluorinated interphases enable high-voltage Li-metal batteries, *Chem.* 4 (2018) 174–185.

- [21] L. Suo, W. Xue, M. Gobet, S. G. Greenbaum, C. Wang, Y. Chen, W. Yang, Y. Li, J. Li, Fluorine-donating electrolytes enable highly reversible 5-V-class Li metal batteries, *Proc. Natl. Acad. Sci. U.S.A.* 115(6) (2018) 1156–1161.
- [22] J. Zhou, Y. Guo, C. Liang, L. Cao, H. Pan, J. Yang, J. Wang, A new ether-based electrolyte for lithium sulfur batteries using a S@PAN cathode, *Chem. Commun.* 54 (2018) 5478–5481.
- [23] B. Liu, W. Xu, P. Yan, X. Sun, M. E. Bowden, J. Read, J. Qian, D. Mei, C.-M. Wang, J.-G. Zhang, Enhanced cycling stability of rechargeable Li-O₂ batteries using high-concentration electrolytes, *Adv. Funct. Mater.* 26 (2016) 605–613.
- [24] L.Suo, Y.-S. Hu, H. Li, M. Armand, L. Chen, A new class of solvent-in-salt electrolyte for high-energy rechargeable metallic lithium batteries, *Nat. Commun.* 4 (2013) 1481.
- [25] X. Ren, S. Chen, H. Lee, D. Mei, M. H. Engelhard, S. D. Burton, W. Zhao, J. Zheng, Q. Li, M. S. Ding, M. Schroeder, J. Alvarado, K. Xu, Y. S. Meng, J. Liu, J.-G. Zhang, W. Xu, Localized high-concentration sulfone electrolytes for high-efficiency lithium-metal batteries, *Chem* 4(8) (2018) 1877–1892.
- [26] S. Chen, J. Zheng, D. Mei, K. S. Han, M. H. Engelhard, W. Zhao, W. Xu, J. Liu, J.-G. Zhang, High-voltage lithium-metal batteries enabled by localized high-concentration electrolytes, *Adv. Mater.* 30(21) (2018) 1706102.
- [27] S. Chen, J. Zheng, L. Yu, X. Ren, M. H. Engelhard, C. Niu, H. Lee, W. Xu, J. Xiao, J. Liu, J.-G. Zhang, High-efficiency lithium metal batteries with fire-retardant electrolytes, *Joule* 2(8) (2018) 1548–1558.
- [28] X. Ren, L. Zou, X. Cao, M. H. Engelhard, W. Liu, S. D. Burton, H. Lee, C. Niu, B. E. Matthews, Z. Zhu, C. Wang, B. W. Arey, J. Xiao, J. Liu, J.-G. Zhang, W. Xu, Enabling high-voltage lithium-metal batteries under practical conditions, *Joule* 3(7) (2019) 1662–1676.

II. THEORY

2.1 Electrochemistry

The electrochemistry theory is excellently presented in the book “ELECTROCHEMICAL METHODS, Fundamentals and Applications” by Allen J. Bard and Larry R. Faulkner ^[1] and the handouts of the “Electrochemistry” course by Hochun Lee in DGIST. Here is a summary of the most important aspects of this paper.

2.1.1 Electromotive Force

The term electromotive force (EMF), was introduced to describe the force that the current flows through a conductor in a closed loop in the early 1800s. This can come from many sources, but for the scope of this paper only describes in terms of galvanic cells. In the case of galvanic cells, Faraday assumed that the chemical reactions taking place at the electrodes are the 'seat of the EMF', i.e. these reactions induce currents. The term is used to describe the cell potential, E , of a battery system. This is measured in volts (V) where the SI unit is Joule/Coulomb ($J/C=[kgm^2/s^3A]$). When the total reaction occurs in an electrochemical cell with negative ΔG ($-\Delta G$), it is termed a galvanic cell and the corresponding EMF of that reaction would be;

$$E = \frac{-\Delta G}{nF} \quad (2.1)$$

where n is the charge transfer in a reaction and nF is the total charge, in C (coulomb), produced per M (mol).

2.1.2 Electrode Potential

A total reaction can be divided to at least two reactions in an electrochemical cell, one happening at the positive electrode (the cathode), and the other happening at the negative electrode (the anode). By

convention, these reactions are used as reduction reactions and the corresponding electrode potentials are associated with each of these reactions. The electrode potential cannot be measured in absolute quantity, but is always measured relative to a reference electrode, such as SHE (standard hydrogen electrode), the reaction of $H^+/\frac{1}{2}H_2$.

For example, for the potential of lithium we have the reaction



where the electrode potential (E) at standard conditions is -3.00 V vs. SHE. When Li^+/Li itself is used as a reference in a Li-ion battery system, E of this reaction is 0.0 V.

For most reactions, standard electrode potential (E^0) has been defined. The actual electrode potential of a reaction usually differs from E^0 , and several factors influences the actual electrode potential, such as; concentration, solvent and temperature. These factors are summarized in the literature as activity (a) and the corresponding electrode potential is

$$E = E^0 + \left(\frac{RT}{nF}\right) \ln \frac{a_O}{a_R} \quad (2.3)$$

where a_O and a_R denotes the activity of the oxidation and reduction, respectively.

The total EMF at zero current, also called the open circuit voltage (OCV) of a galvanic cell would then be

$$E = E_a - E_c \quad (2.4)$$

where E_a and E_c denotes the electrode potential of the anode and the cathode, respectively. In this paper, the activity of a given specie will not be discussed, since only electrode potentials of systems are being investigated.

2.1.3 Energy Storage

The energy of a galvanic cell is operated by having two reactants separated by a media with low voltage and high voltage. The energy will be released after an electronic pathway is created between the

reactants completing the circuit. Fig. 2.1 shows a general overview of a galvanic cell ($\Delta G_c < \Delta G_a$ and $E_c > E_a$). The total cell potential of this cell is $E = E_c - E_a$. The electrons are released through the external circuit as the chemical reaction of electrical work.

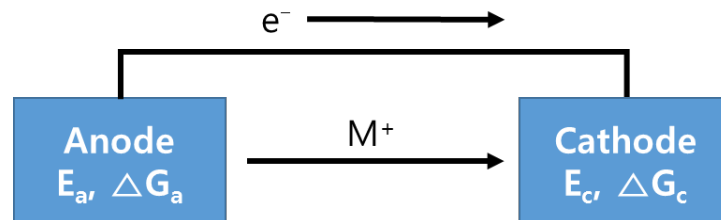


Fig. 2.1 A general overview of a galvanic cell.

The total amount of charge that can be stored depends directly on the amount of electrode material in the battery.

2.2 Battery Theory

A battery generally refers to one or more electrochemical cells capable of storing chemical energy and releasing it as electrical energy. They are divided into two types (primary and secondary batteries). Primary batteries are commonly known as disposable batteries. It is based on irreversible electrochemical reactions and should be replaced after one discharge. These types of batteries include very common alkaline batteries and more speculative zinc/air batteries. However, secondary batteries are composed of reversible cells and are also referred to as rechargeable batteries. Common types of secondary batteries include lithium-ion, lead-acid, and nickel-metal hydride batteries.

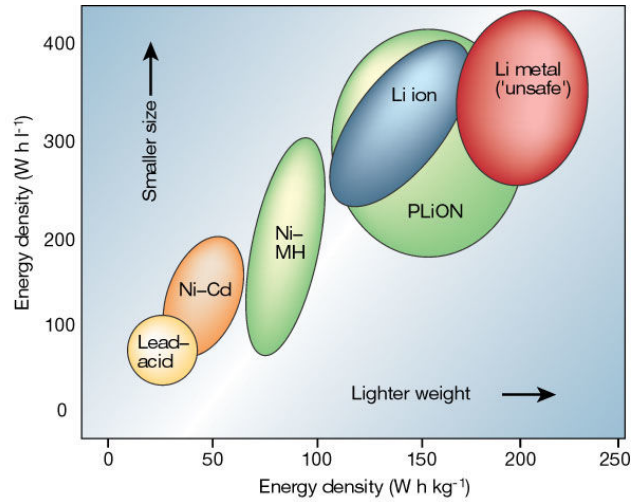


Fig. 2.2 Comparison of the different battery technologies in terms of volumetric and gravimetric energy density.^[2]

2.3 Lithium Batteries

The normal operation of a lithium-ion batteries will be a good basis for the understanding of rechargeable batteries. Fig. 2.2 shows a typical lithium-ion cell which contains three basic elements: the anode, the cathode and the electrolyte. In most modern batteries, a porous membrane is also present between the anode and the cathode to eliminate the possibility of electronic short-circuit, minimize the electrolyte usage and increase the structural integrity of the batteries. The anode and cathode are the negative and positive electrodes, respectively, meaning that upon discharge, electrons and cations w from the anode to the cathode. Connecting the electrodes to the complete circuit is what is collectively called current collectors.

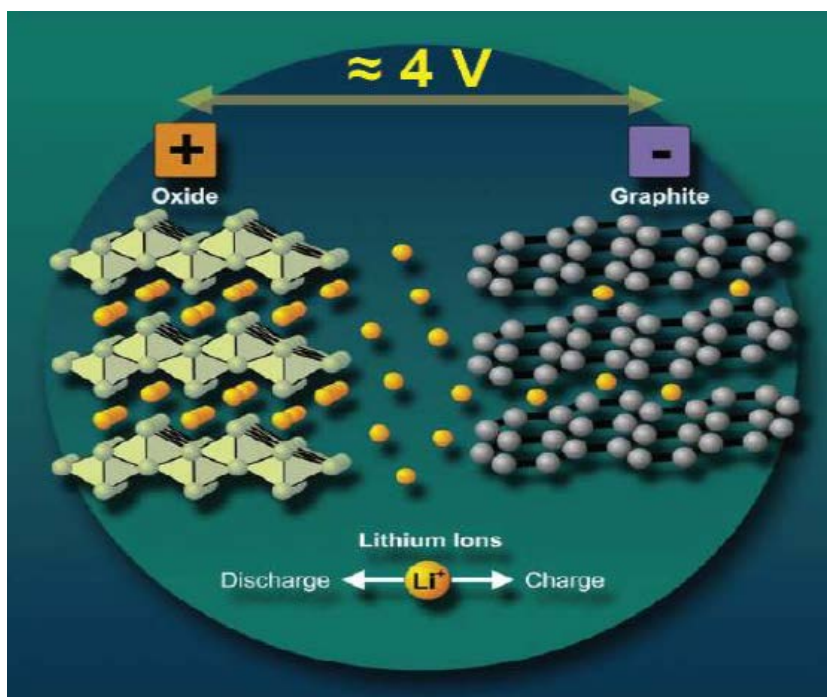


Fig. 2.3 Schematic of a general Li-ion battery cell with cathode (ex. LiCoO_2), anode (ex. C_6) and electrolyte. The electrons in the external circuit is driven by a voltage source on charge and performs work on discharge. Adapted from the handouts of the “Electrochemistry” class.

Li-ion batteries are a so-called structural or ion-transfer batteries, meaning that they have a structure that allows ions to enter and exit the electrode material in the process called intercalation. When the Li-ion battery is charged, Li-ions are de-intercalated from the cathode, through the electrolyte and onto, or into, the anode. When the Li-ions flow out of the cathode, the cathode material itself must be oxidized to supply the charge. For example, for a LiCoO_2 cathode, one Co ion should be oxidized from +III to +IV for all Li ions leaving the structure. This occurs at an electrode potential of about 3.8 V (vs. Li). At the other end, in the anode, Li ions are reduced to Li atoms. When the anode is pure Li metal, it happens at the electrode potential of Li^+/Li , 0 V (vs. Li). If a more commonly used graphite anode is used, the reduction occurs at a slightly higher potential than Li metal, around 0.1–0.3 V (vs. Li). The overall applied voltage should be higher than the combined voltage required to reduce Li ions and oxidize cathode material due to the over-potential. So for example, a standard cell with a LiCoO_2 cathode and a graphite anode has an approximate

voltage of $0\text{ V} - -3.8\text{ V} = 3.8\text{ V}$ using the Equation 2.4. This voltage is influenced by various factors such as the electrolyte, the state of charge (SOC) and etc.

The last ion removed from the cathode requires much more energy than the initial ion and the oxidation voltage increases. Furthermore, as the graphite is more intercalated, the reduction potential of Li-ions in graphite drops towards the electrode potential of Li^+/Li and further increases the total voltage.

2.3.1 Anode Materials

Anode material is the material that stores the reduced lithium atom. The performance of the electrode is affected by several factors: (1) the voltage to store lithium, (2) the kinetics of electron transfer, (3) the ability to store lithium, (4) the available surface area, and (5) the structural integrity of the material.

2.3.1.1 Metal

The most obvious choice for an anode of LIB system is pure Li metal. This is the densest material of the Li atoms and the reduction potential for Li^+/Li is zero (0) V. There was a limit to the use of pure Li metal in consumer products. Li re-deposition is inherently difficult because the best electrolytes for a LIB creates an SEI-layer on the electrodes. The redeposited Li has been shown to grow dendritic structures, which ultimately pose a risk of short-circuit and explosion^[3]. This dendrite is created by the uneven re-deposition of the metal. During cycling, the elevated structure of the metal will have a higher current density than the lower part, so more metal will be deposited on the elevated structure. This is a self-reinforcing mechanism that promotes the growth of the dendrites. The reactivity of dendrites in water and air is also very high and dangerous for use in consumer products.

2.3.1.2 Graphite

The most common anode material is carbon in the form of graphite. The average reduction potential for Li^+ in graphite is 50–250 mV versus Li^+/Li . This reduces the energy and power output by slightly reducing the overall battery voltage, but the cyclability and stability of graphite is much greater than the Li

metal anodes that overcome the drawback of the voltage reduction. The charging of these materials is based on intercalation, which means that the material does not alloy with Li and stores only Li atoms between the graphene sheets. The fully lithiated graphite generally represented by the formula LiC_6 , which stores one Li atom per six C atoms ($\text{Li}^+ + \text{C}_6 \rightarrow \text{LiC}_6$), and the theoretical gravimetric capacity is 372 mAh/g.

2.3.2 Electrolytes

The electrolyte consists of two parts, a solvent and a Li-containing salt.

2.3.2.1 Salt

There are three main factors that determine the choice of salt; Conductivity, chemical and thermal stability and toxicity. To achieve high conductivity, it is important that the salt completely dissociates and dissolves, and that the solvated ions, especially the Li cations, have high mobility. Multiple electrolyte salts can be used in LIBs, among others, LiBF_4 , LiClO_4 , LiAsF_6 , LiFSI , LiPF_6 , and etc.

2.3.2.2 Solvent

Since Li and the Li salts have high reactivity to water, organic solvents should be used and several factors, such as salt, determines the choice of solvent. The primary selecting factor is that it needs to be polar to dissolve sufficient amounts of lithium salts, such as organic compounds with either carbonyl groups, nitrile groups, sulfonyl groups or ether-linkages. In addition, it should exhibit high stability, both thermally and electrochemically, and as LIBs often operate at voltage differences of up to 4.5 V it requires a wide operating voltage. Finally, the composition of the solvent also determines the composition of the SEI layer.

Ethylene carbonate (EC) was used for the first time as a battery co-solvent by Elliot (1964) due to its low viscosity and high dielectric constant. Until the early 1970s, it was considered unusable for the purpose due to its high melting point (ca. 36 °C) when it was found that a co-solvent would lower the melting

point and after Sony's initial launch of LIBs (1993), it was found that mixing EC with a linear carbonate would provide the required electrochemical and temperature window^[4]. Linear carbonates such as dimethyl carbonate (DMC), ethyl methyl carbonate (EMC), and diethyl carbonate (DEC) have proved a good match and most batteries uses a 1:1 or a 3:7 mixture of EC:linear carbonate as the solvent.

Table 2.1 Properties of commonly used solvents in LIBs. All data from the handouts of the “Electrochemistry” class.

	<i>EC</i>	<i>DMC</i>	<i>EMC</i>	<i>DEC</i>
Molecular weight	88.07	90.08	104.11	118.13
Boiling point (°C)	244	90	107	126
Melting point (°C)	39	0.5	-55	-74
Density	1.32	1.07	1.007	0.975
Dielectric constant	90	3.1	2.8	2.8
Viscosity (cP)	1.92 (40°C)	0.625 (20°C)	0.665 (25°C)	0.736 (25°C)

2.3.3 Solid Electrolyte Interphase (SEI)

Li metal anodes are known to react with both liquid and polymer electrolytes and are covered with a passive film that delays Li corrosion and decomposition of the electrolyte. This film is called solid electrolyte interphase (SEI) because it acts an interface between the anode and the electrolyte. The SEI thickness is limited by the electron tunneling range because this film is electronically non-conductive and electrons are required for the decomposition and deposition of the SEI^[5]. The film is conductive for Li ions, but has a certain resistivity, so a very thick SEI layer can increase cell resistance. In a normal LIBs, the SEI layer is formed on the anode (Li or graphite) electrodes when Li ions is first applied to the anode during the first charge. The chemistry of SEI layer formation is inherently complex and not well understood. The SEI

composition is not fully understood but it generally consists of decomposed electrolyte, solvent and salt. Generally, the SEI layer contains LiPF_6 , LiF , Li_2O , Li_2CO_3 , $(\text{CH}_2\text{OCO}_2\text{Li})_2$, and ROCO_2Li ^[6].

2.3.4 Additives

Use of electrolyte additive is one of the most effective and economic methods for the improvement of Li-ion battery performance. Usually, the amount of an additive in the electrolyte is no more than 5% either by weight or by volume while its presence significantly improves the cycle life and rate performance of Li-ion batteries. For better LIBs performance the additives are able to: (1) facilitate formation of SEI on the surface of graphite. (2) reduce irreversible capacity and gas generation for the SEI formation and long-term cycling, (3) enhance thermal stability of LiPF_6 against the organic electrolyte solvents, (4) protect cathode material from dissolution, and (5) improve physical properties of the electrolyte such as ionic conductivity, viscosity, wettability to the polyolefin separator, and so forth. For better battery safety, the additives are able to: (1) lower flammability of organic electrolytes, (2) provide overcharge protection or increase overcharge tolerance, and (3) terminate battery operation in abuse conditions.

2.3.5 Cathode Materials

Cathodes in a secondary LIBs are so-called intercalation cathodes. The cathode material is a crystal structure containing lithium, which is one of the main components. The key factors for cathode materials are high ionic conductivity of Li, high electronic conductivity, favorable volume expansion at discharge, high energy density, and excess tension remaining in the structure when Li ions are removed from the structure. As you can see, the high ionic conductivity and electronic conductivity of the cathode are very important for the charging rate. For each Li ion de-intercalated in the structure, electrons must move from the cathode material to the current collector to complete the charge balance. This is significant because many of the best cathode materials are very poor electronic conductors. The electronic conductivity is increased by adding small amounts of electrical conductors, such as carbon black, to the cathode in most

commercial LIBs. When Li ions are de-intercalated from the cathode material, the internal stress of the structure increases for two reasons. First, the residual ions must be oxidized to balance the charge and change the extent of the electron orbitals of these ions. Second, the space previously occupied by a Li ion is now a defect, for which the structure itself must compensate for this.

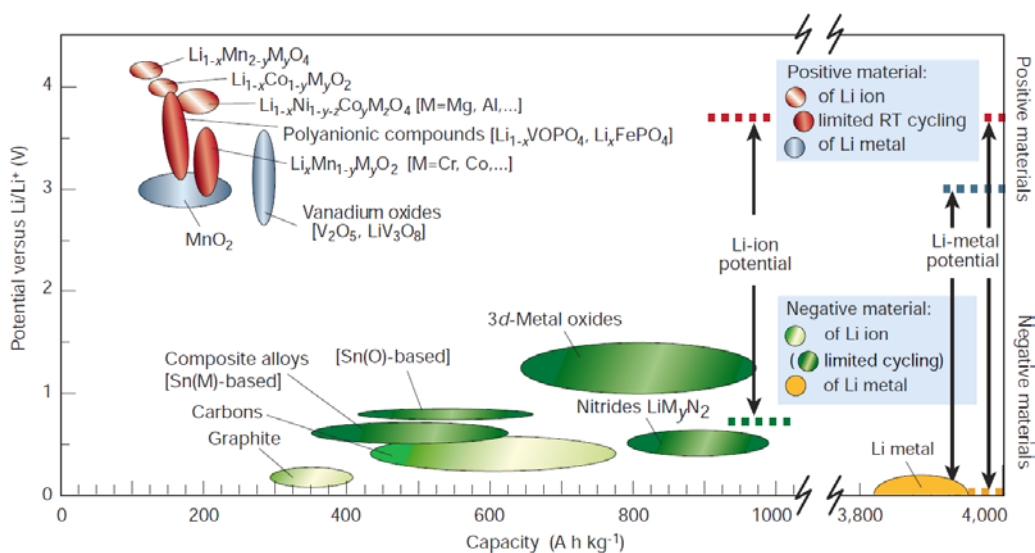


Fig. 2.4 Voltage versus capacity for cathode- and anode-electrode materials presently used or under serious considerations for the next generation of rechargeable Li-based cells^[2].

2.4 References

- [1] A.J. Bard, L.R. Faulkner, J. Leddy, C.G. Zoski, *Electrochemical methods: fundamentals and applications*, Wiley, New York, 1980.
- [2] J.-M. Tarascon, M. Armand, Issues and challenges facing rechargeable lithium batteries, *Nature*, 414 (2001) 359-367.
- [3] F. Orsini, A. Du Pasquier, B. Beaudoin, J. Tarascon, M. Trentin, N. Langenhuizen, E. De Beer, P. Notten, In situ scanning electron microscopy (SEM) observation of interfaces within plastic lithium batteries, *J. Power Sources*, 76 (1998) 19-29.
- [4] K. Xu, Nonaqueous liquid electrolytes for lithium-based rechargeable batteries, *Chem. Rev.*, 104

(2004) 4303-4418.

[5] P.B. Balbuena, Y. Wang, Lithium-ion batteries: solid-electrolyte interphase, World, Scientific, 2004.

[6] P. Verma, P. Maire, P. Novák, A review of the features and analyses of the solid electrolyte interphase in Li-ion batteries, *Electrochim. Acta*, 55 (2010) 6332-6341.

III. Comparative study on lithium borates as corrosion inhibitors of aluminum current collector in lithium bis(fluorosulfonyl)imide electrolytes

3.1 Introduction

Nowadays, Li-ion batteries (LIBs) are forced to achieve both higher energy density and extreme long-term stability for the reliable operation of IT devices and electric vehicles ^[1-4]. Most of the current LIBs are employing lithium hexafluorophosphate (LiPF₆)-based electrolytes due to high ionic conductivity, decent safety, and innate immunity to aluminum (Al) current collectors ^[5]. Nevertheless, LiPF₆ electrolytes are inevitably contaminated by hydrogen fluoride (HF), a byproduct of LiPF₆ hydrolysis, which facilitates metal dissolution from cathode materials ^[6, 7] and exacerbates unwanted side reactions at the anode side ^[8].

As an alternative candidate to LiPF₆, various Li salts that are inherently free from HF contamination (e.g., lithium bis(oxalato)borate (LiBOB), lithium difluoro(oxalato)borate (LiDFOB), lithium bis(pentafluoroethanesulfonyl)imide (LiBETI), and lithium bis(trifluoromethanesulfonyl)imide (LiTFSI)) have been extensively investigated ^[9-16]. None of the Li salts, however, have been successful to replace LiPF₆, mainly due to their low ionic conductivity. Recently, lithium bis(fluorosulfonyl)imide (LiFSI) has been reported to exhibit comparable or higher ionic conductivity to LiPF₆ while maintaining HF-free nature, which suggests that LiFSI can offer both the superior energy density and long-term stability of LIBs ^[17, 18]. LiFSI, however, is subjected to severe corrosion of Al current collector ^[18, 19], a common chronic issue of lithium imide salts ^[1, 20].

So far, a vast amount of effort has been directed toward the prevention of Al corrosion in imide-based electrolytes ^[20-29]. Some recent studies have tried to inhibit the Al corrosion by employing new types of solvents other than carbonates. It was reported that Al corrosion in LiTFSI solutions is significantly suppressed in solvents, such as adiponitrile, tetrahydrofuran, dimethoxyethane, methyl difluoroacetate, and γ -butyrolactone, compared to conventional ethylene carbonate (EC)-based electrolytes ^[20-23]. These solvents commonly show low dielectric constants compared to EC, which suggests a possibility that low solubilities of

corrosion products ($\text{Al}(\text{TFSI})_n^{n-3}$, $n=1-3$) are beneficial in Al corrosion suppression [24-26]. It was also claimed that fluorinated solvents such as methyl difluoroacetate, fluoroethylene carbonate (FEC), and fluorodiethyl carbonate (FDEC) exhibit suppressed Al corrosion by forming a protective fluoride surface layer [23, 27]. In addition, the concentration of Li salts has been found to have substantial influence on Al corrosion behavior. It was reported that Al corrosion is alleviated in highly concentrated ($> 1.8 \text{ M}$) LiTFSI solutions [28, 29]. Even though these studies are quite informative, altering the solvent nature and salt concentration are bound to affect not only Al corrosion behavior, but also the other physicochemical properties of the electrolyte (e.g., ionic conductivity, wettability, compatibility with active materials), which significantly depreciates their practical potential.

In this regard, employing electrolyte additive is a promising strategy because it hardly affects the bulk properties of original electrolyte systems. In particular, it has widely been known that the addition of LiPF_6 to LiTFSI electrolytes can notably suppress Al corrosion [5]. LiPF_6 was also used as an Al corrosion inhibitor in FSI-based ionic liquids [30]. The presence of LiPF_6 , however, even if the amount is limited (ca. 0.1-0.2 M), can cause unwanted HF generation, which again raises all of the drawbacks of LiPF_6 -based electrolytes. The addition of Li-borate salts like LiBF_4 and LiBOB were also claimed to mitigate Al corrosion [31-33], but the inhibition abilities of the borates seem to be inferior to that of LiPF_6 additive. Moreover, quantitative comparison among the borate additives has been deterred because prior studies employed different experimental conditions (e.g., solvent composition, additive content, Al pretreatment method, electrochemical measurement conditions). Also, the study on the corrosion inhibition of Al in LiFSI solutions is scarce in contrast to that in LiTFSI ones [30, 34].

In this work, we performed a systematic comparison on the inhibition effects of Li-borate (LiBF_4 , LiDFOB , and LiBOB) and LiPF_6 additives on Al corrosion in LiFSI EC/DEC (3/7, v/v) solutions. Among the additives, LiDFOB was revealed to be the most efficient inhibitor of Al corrosion in LiFSI-based electrolytes. The Al corrosion behavior in 0.8 M LiFSI+0.2 M LiDFOB was determined to be comparable to that of 1 M LiPF_6 solution, an Al corrosion-immune medium. The excellent inhibition ability of LiDFOB additive was further examined using the X-ray photoelectron spectroscopy (XPS) analysis of the Al surface layer and was

also confirmed through the rate capability/electrochemical impedance spectroscopy (EIS) measurements of LiCoO₂ cells.

3.2 Experimental

3.2.1 Chemicals

Battery grade LiFSI, LiDFOB, LiBOB, EC, dimethyl carbonate (DMC), and diethyl carbonate (DEC) were provided by LG Chem. Reagent grade LiBF₄ and Al rod (99.999%, 3 mm diameter) were purchased from Aldrich. The studied electrolytes are 0.8 M LiFSI (hereafter called LiFSI), 0.8 M LiFSI+0.2 M LiBF₄ (LiFSI+BF₄), 0.8 M LiFSI+0.2 M LiBOB (LiFSI+BOB), 0.8 M LiFSI+0.2 M LiDFOB (LiFSI+DFOB), 0.8 M LiFSI+0.2 M LiPF₆ (LiFSI+PF₆), and 1 M LiPF₆ (LiPF₆) in EC/DEC (3/7, v/v). All the electrolytes were prepared in an Ar-filled globe box (H₂O and O₂ levels < 5 ppm and 25 ± 1 °C). The water content of the electrolytes was in the range of 18–45 ppm.

3.2.2 Electrochemical experiments

All the electrochemical experiments were carried out using a three-electrode system with a flooded cell (polyethylene round bottle) with 2.5 ± 0.1 mL of electrolyte in an Ar-filled glove box. An Al rod (0.07 cm²) was used as a working electrode. Li foil and Pt wire were used as a reference electrode and counter electrode, respectively.

Before investigation of the corrosion inhibition abilities of additives, the effects of surface roughness on the Al corrosion behavior were examined (Fig. 3.1). One side of Al rod was polished with emery papers (#1200, 15 μm grit size, and #3000, 7 μm grit size), and with alumina slurry (0.3 μm grit size) on a polishing pad.

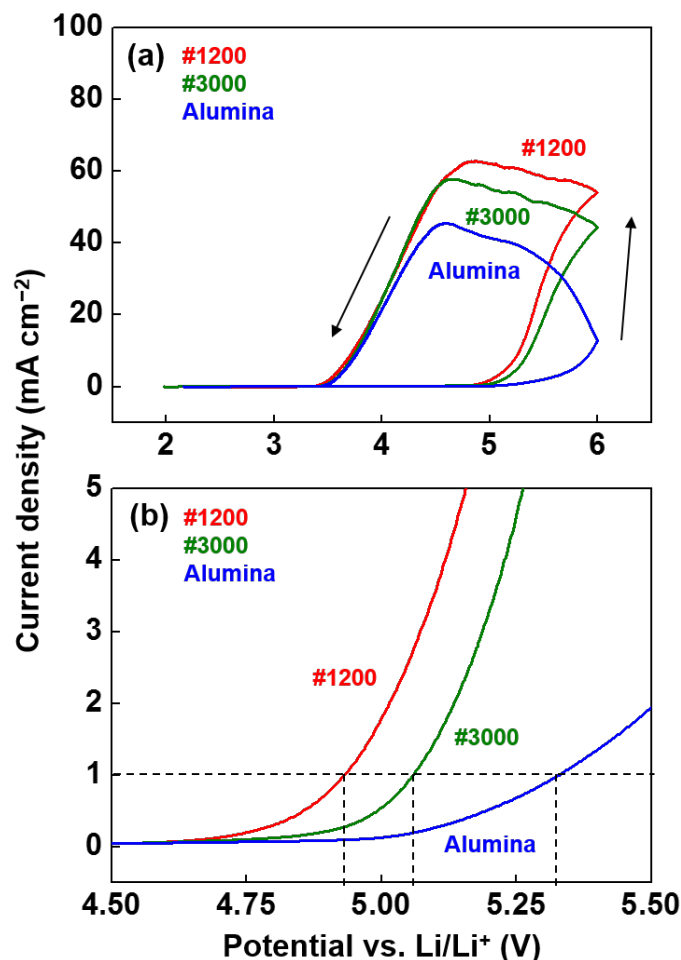


Fig. 3.1 (a) Cyclic voltammograms (CVs) of 1 M LiFSI EC/DMC (3/7, v/v) to examine the effects of polishing method of Al working electrode and (b) expanded view of (a). Emery paper (#1200, 15 μm grit), Emery paper (#3000, 7 μm grit), and alumina slurry (0.3 μm grit).

To compare the extent of Al corrosion quantitatively, the corrosion onset is assumed to be the potential value at which the anodic current reaches 1 mA cm^{-2} . In this manner, the extent of Al corrosion can be ordered in the following order: emery #1200 > emery #3000 > alumina (Fig. 3.1b). Also, the maximum current at the first cathodic scan follows the same order.

In this study, the Al working electrode was polished on emery paper (#1200, 15 μm grit size) to examine the Al corrosion/inhibition behaviors under relatively harsh conditions. After polishing, the Al electrode was

sonicated in double-distilled water for 5 min to remove any residuals. Finally, Al electrode was dried using dry nitrogen flow at room temperature. Cyclic voltammetry (CV) was performed over 3–6 V (vs. Li/Li⁺) with a scan rate of 10 mV s⁻¹. Chronoamperometry (CA) was carried out by applying a potential step from the open circuit voltage to 4.8 V (vs. Li/Li⁺) for 2 h at 45 °C. The ionic conductivities of electrolytes were measured over 10–60 °C with an ionic conductometer (Thermo Scientific). The deviations in the temperature and the ionic conductivity were ± 0.2 °C and ± 0.04 mS cm⁻¹, respectively. Before each measurement, the electrolyte sample was kept for 30 min at a given temperature. Although molality (mol kg⁻¹) is the more appropriate unit than molarity (mol L⁻¹) in determining the ionic conductivity over the temperature range, this study adopted molarity because it is more popular in the LIB society. In addition, the difference between molarity and molality was not significant (less than 5 % over 10–60 °C).

3.2.3 XPS

XPS measurements were performed to examine the composition of the Al surface layer using ESCALAB 250Xi (Thermo Scientific). For the preparation of samples, Al foils (battery grade, 45 μ m thickness) were subjected to two cycles over 3–6 V (vs. Li/Li⁺) in four different electrolytes: LiFSI, LiFSI+BF₄, LiFSI+BOB, and LiFSI+DFOB. After the cycling, the Al foils were rinsed in DMC to eliminate residual electrolyte and then dried for 24 h inside a glove box. For depth profiles measurements, the Al foils were sputtered for 100 s with an etching rate of 7 nm min⁻¹ calibrated for SiO₂. In the case of LiFSI+DFOB, the sputtering process was extended to 500 s due to the thick surface film compared to the others.

3.2.4 LiCoO₂ cell tests

2032-type coin cells were employed to evaluate LiCoO₂ cell performances. Al-coated coin cells were used at the cathode side to prevent the corrosion in LiFSI and LiFSI+DFOB electrolytes. The cathode electrode was fabricated with 95 wt % LiCoO₂ (18.26 mg cm⁻²), 2.5 wt % conductive carbon, and 2.5 wt % polyvinylidene difluoride (PVDF) binder. The anode electrode was prepared with artificial graphite (9.43 mg

cm⁻²), 2.0 wt % conductive carbon, and 3 wt % PVDF. These cathode and anode electrodes, polyethylene separator (Tonen), and three types of electrolytes (LiFSI, LiFSI+DFOB, and LiPF₆) were used to assemble LiCoO₂/graphite cells. All the cells were cycled initially at 25 °C over 2.5–4.25 V three times with 0.1 C (first cycle) and 0.2 C (second and third cycles) constant current (CC) followed by 4.25 V constant voltage (CV) charging, and 0.2 C CC discharging to complete the formation process. A rate capability test was carried out with 0.5 C/4.25 V (CC/CV) charging and various CC discharging.

3.2.5 EIS

The EIS measurements were carried out for LiCoO₂/LiCoO₂ symmetric cells. For the fabrication of LiCoO₂ symmetric cells, LiCoO₂ electrodes with a state-of-charge (SOC) of 50 were collected from LiCoO₂/Li cells, which had been cycled three times over 3–4.3 V. The frequency range was 100 kHz–10 mHz, the ac amplitude 5 mV, and the dc bias voltage 0.0 V.

3.3 Results and discussion

3.3.1 Inhibitive effects of borate additives on Al corrosion in LiFSI electrolytes

The CVs of Al in LiFSI, LiFSI+BF₄, LiFSI+BOB, and LiFSI+DFOB at the first cycle are compared in Fig. 3.2. The CVs in LiFSI+PF₆ and LiPF₆ are also presented for comparison. In LiFSI (i.e., the LiFSI solution without any additive), the anodic corrosion current begins to rise steeply above 5.3 V at the first anodic scan and keeps growing even after the scanning direction is reversed at 6.0 V (Fig. 3.2a). After reaching the maximum, the anodic current decreases rapidly and nears zero at around 3.6 V. This counter-clockwise CV shape manifests severe Al corrosion behavior commonly observed in lithium imide solutions [5, 18–22, 33, 34].

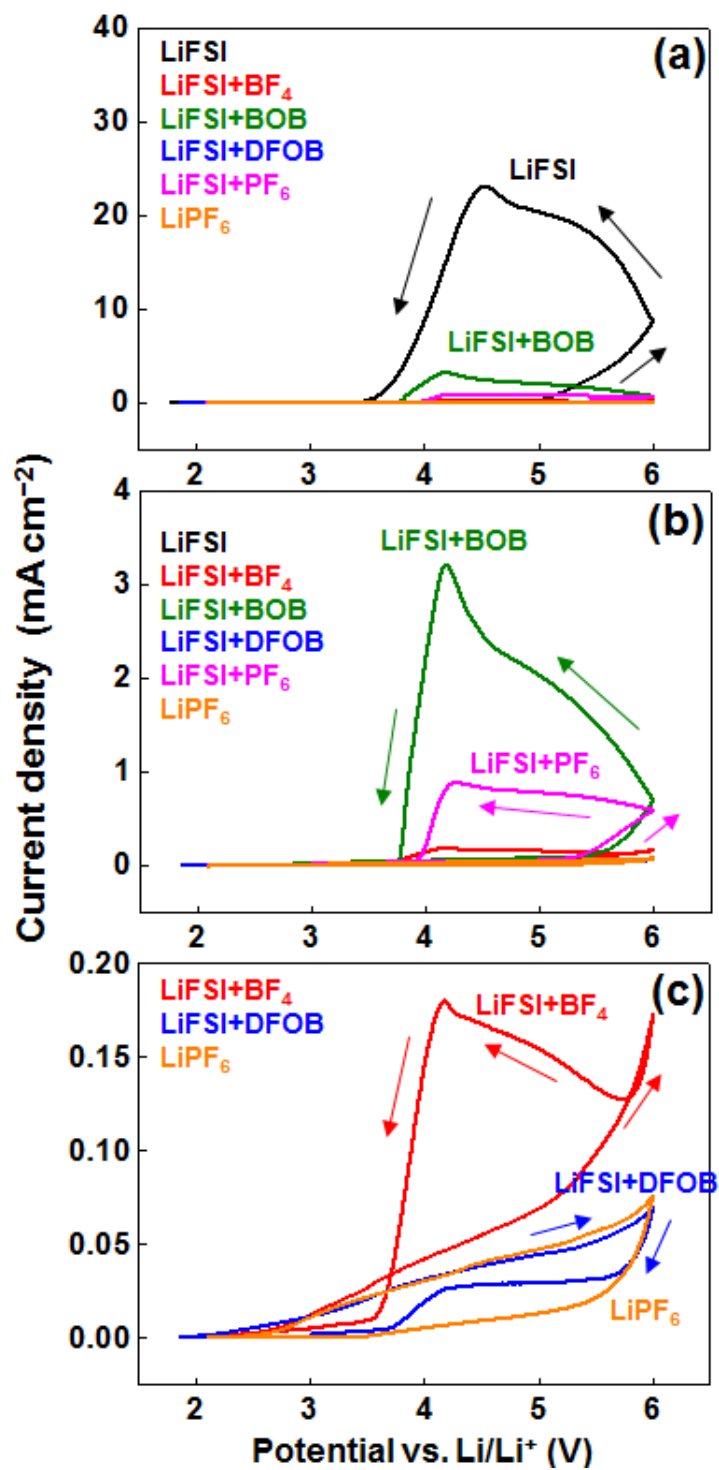


Fig. 3.2 (a) CVs of Al electrodes at the 1st cycle in LiFSI, LiFSI+BF₄, LiFSI+BOB, LiFSI+DFOB, (b) expanded view of (a), and (c) expanded view of (b). The CVs of LiFSI+PF₆ and LiPF₆ are also presented for comparison.

The huge Al corrosion current appearing in LiFSI is significantly reduced by the presence of borate and LiPF₆ additives (Fig. 3.2a). From the expanded views (Fig. 3.2b and 3.2c), it is noted that the corrosion susceptibility decreases in the following order: LiFSI+BOB > LiFSI+PF₆ > LiFSI+BF₄ > LiFSI+DFOB. It is noteworthy that none of LiBOB, LiBF₄, or LiPF₆ additive, previously claimed as effective inhibitors for the Al corrosion in LiTFSI solutions [5, 25, 31–33], is revealed to be promising in LiFSI solutions. However, LiDFOB exhibits outstanding inhibition ability compared to the other borate and LiPF₆ additives (Fig. 3.2c).

The anodic behavior of Al in LiFSI+DFOB is compared in detail with that in LiPF₆, which is an Al corrosion-immune medium (Fig. 3.3). Unlike the other cases, LiFSI+DFOB and LiPF₆ do not show the counter-clockwise current response at the first cycle. In addition, the current at the subsequent cycles keeps decreasing in both solutions, manifesting their excellent passivating nature against Al oxidation [14, 33, 34].

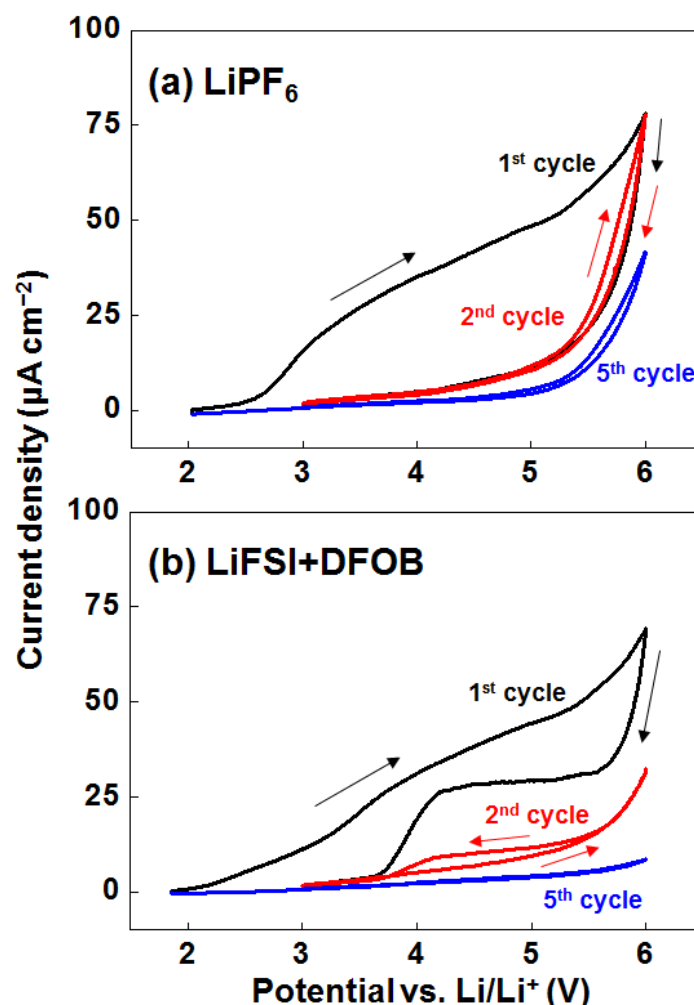


Fig. 3.3 CVs of Al electrodes at the first, second, and fifth cycles in (a) LiPF₆ and (b) LiFSI+DFOB.

The superior inhibition ability of LiDFOB is also confirmed through CA measurements at elevated temperature (45 °C) (Fig. 3.4). The anodic current at an applied potential of 4.8 V is in the following order: LiFSI+BOB > LiFSI+PF₆ > LiFSI+BF₄ > LiFSI+DFOB. The anodic current in LiFSI+BOB, LiFSI+PF₆, or LiFSI+BF₄ drops rapidly upon the potential step, but it increases back after an induction period (ca. 1 min). In sharp contrast, the current in LiFSI+DFOB or LiPF₆ keeps decreasing and remains low up to 2 h. In brief, both the CV and CA results demonstrate that, among the borate and LiPF₆ additives, LiDFOB is the most efficient inhibitor for Al corrosion in LiFSI electrolytes. The corrosion resistance of Al in FSI+DFOB is found to be comparable to that of an Al corrosion-immune LiPF₆ solution.

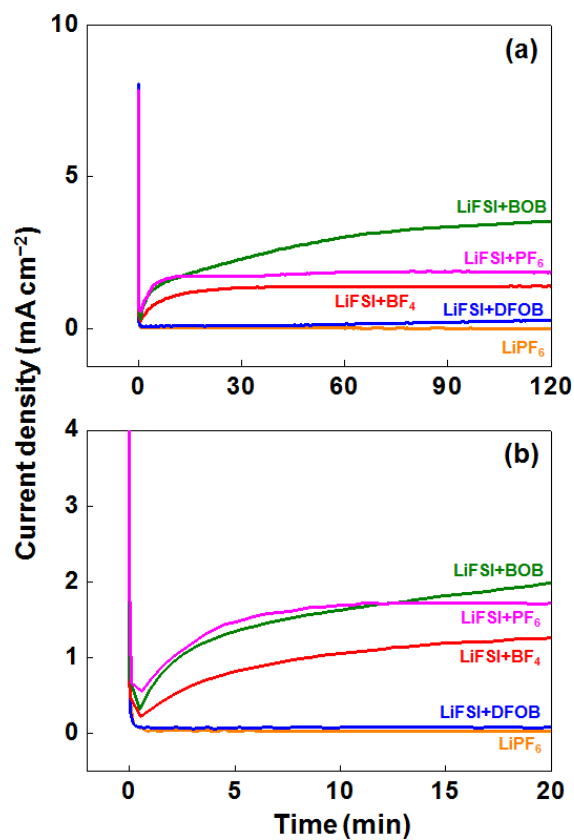


Fig. 3.4 (a) Chronoamperograms of Al electrodes in LiFSI+BF₄, LiFSI+BOB, LiFSI+DFOB, LiFSI+PF₆, and LiPF₆ and (b) expanded view of (a). The potential was stepped from OCV to 4.8 V (vs. Li/Li⁺) at 45 °C.

3.3.2 XPS study on surface composition of Al electrodes

To elucidate the origin of the superior inhibition ability of LiDFOB, the surface compositions of Al electrode were examined using XPS. The depth profiles of the Al_{2p} spectra of Al foils cycled two times over 3–6 V in LiFSI, LiFSI+BF₄, LiFSI+BOB, and LiFSI+DFOB are examined (Fig. 3.5).

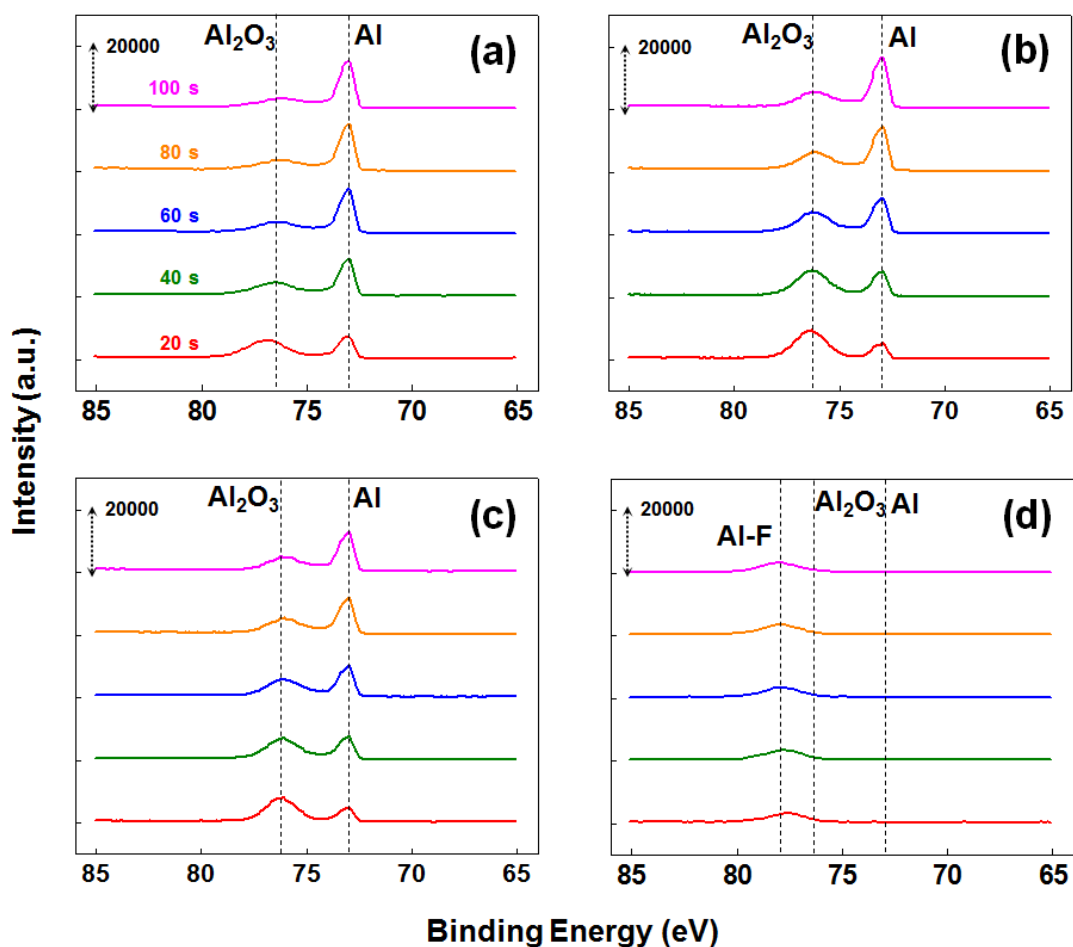


Fig. 3.5 Al_{2p} XPS spectra for Al electrodes cycled in (a) LiFSI, (b) LiFSI+ BF_4 , (c) LiFSI+BOB, and (d) LiFSI+DFOB. The Al electrodes were cycled two times over 3–6 V (vs. Li/Li⁺) before XPS measurements. The depth profiles with increasing sputtering time (20–100 s) are compared.

The spectra before etching are not considered due to possible contamination during sample preparation. The Al electrode cycled in LiFSI shows two Al_{2p} peaks at 73.0 and 76.2 eV (Fig. 3.5a), which are assigned to bare Al metal and Al_2O_3 , respectively^[5]. The presence of bare Al peak even after 20 s etching implies that the thickness of the surface layer is quite thin (less than 1 nm based on SiO_2 etching rate). The ratio of Al_2O_3 to Al peaks decreases with the etching time, as expected. The Al electrodes cycled in LiFSI+ BF_4 and LiFSI+BOB show similar Al_{2p} spectra (Fig. 3.5b and 3.5c) to that cycled in LiFSI (Fig. 3.5a), but somewhat increase the $\text{Al}_2\text{O}_3/\text{Al}$ peak ratio. This implies that a slightly thicker Al_2O_3 layer is formed in LiFSI+ BF_4 or LiFSI+BOB, which may explain the partly mitigated Al corrosion in the corresponding solution. In contrast, the Al sample

subjected to LiFSI+DFOB (Fig. 3.5d) shows a new Al_{2p} peak around 78 eV, which is attributed to Al-F species^[5] while Al_2O_3 and Al peaks diminish significantly. In addition, bare Al peaks become discernable only after 200 s etching (Fig. 3.6), indicating a much thicker surface layer (ca. 24.4 nm based on SiO_2 etching rate) formed in LiFSI+DFOB than in the other three media.

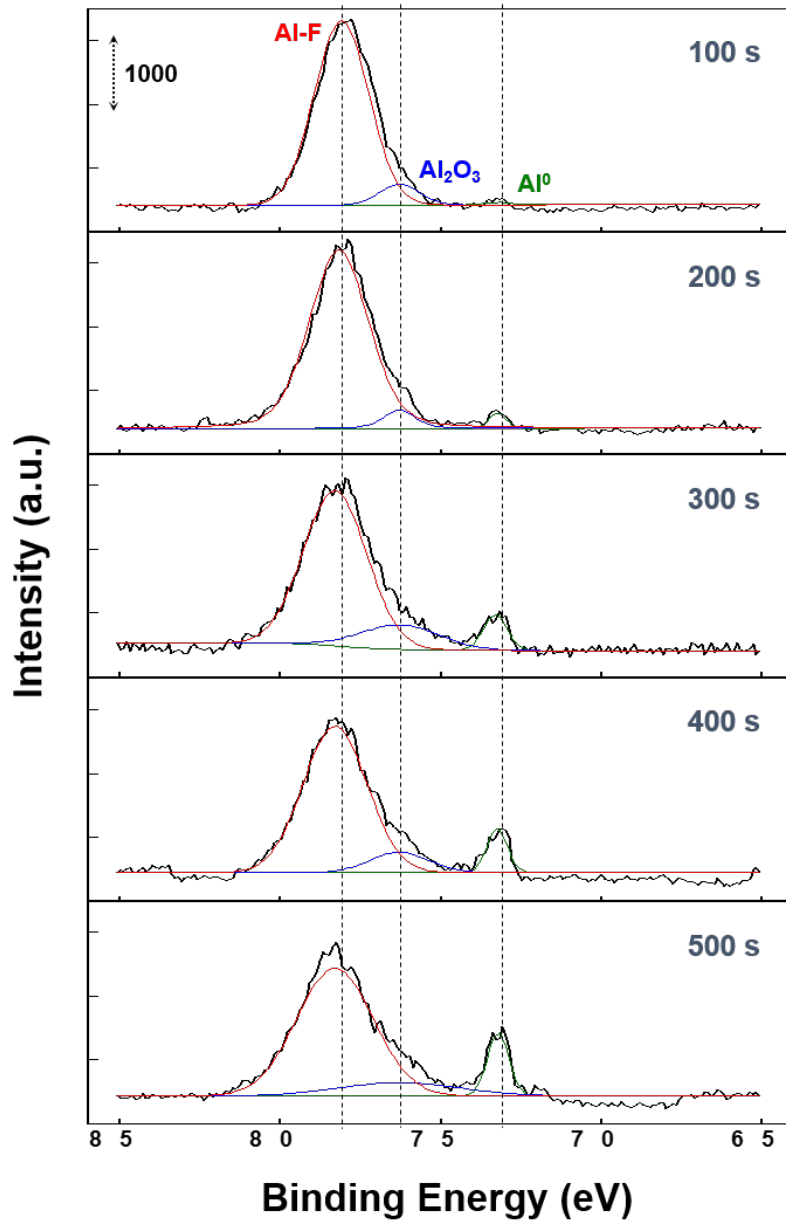


Fig. 3.6 Al_{2p} XPS spectra for Al electrode cycled in LiFSI+DFOB for longer etching time (100–500 s). Bare Al peak becomes discernable only after 200 s etching.

All of the Al electrodes cycled in the borate-added solutions show a signal near 195 eV (Fig. 3.7), which is assigned to B-O/B-F species [35]. However, the B_{1s} peak diminishes notably with etching time for the case of LiFSI+BF₄ and LiFSI+BOB, while it remains, even after 100 s sputtering, for LiFSI+DFOB. This also indicates that LiFSI+DFOB generates a thicker surface layer (ca. 24.4 nm) than the other solutions (less than 1 nm).

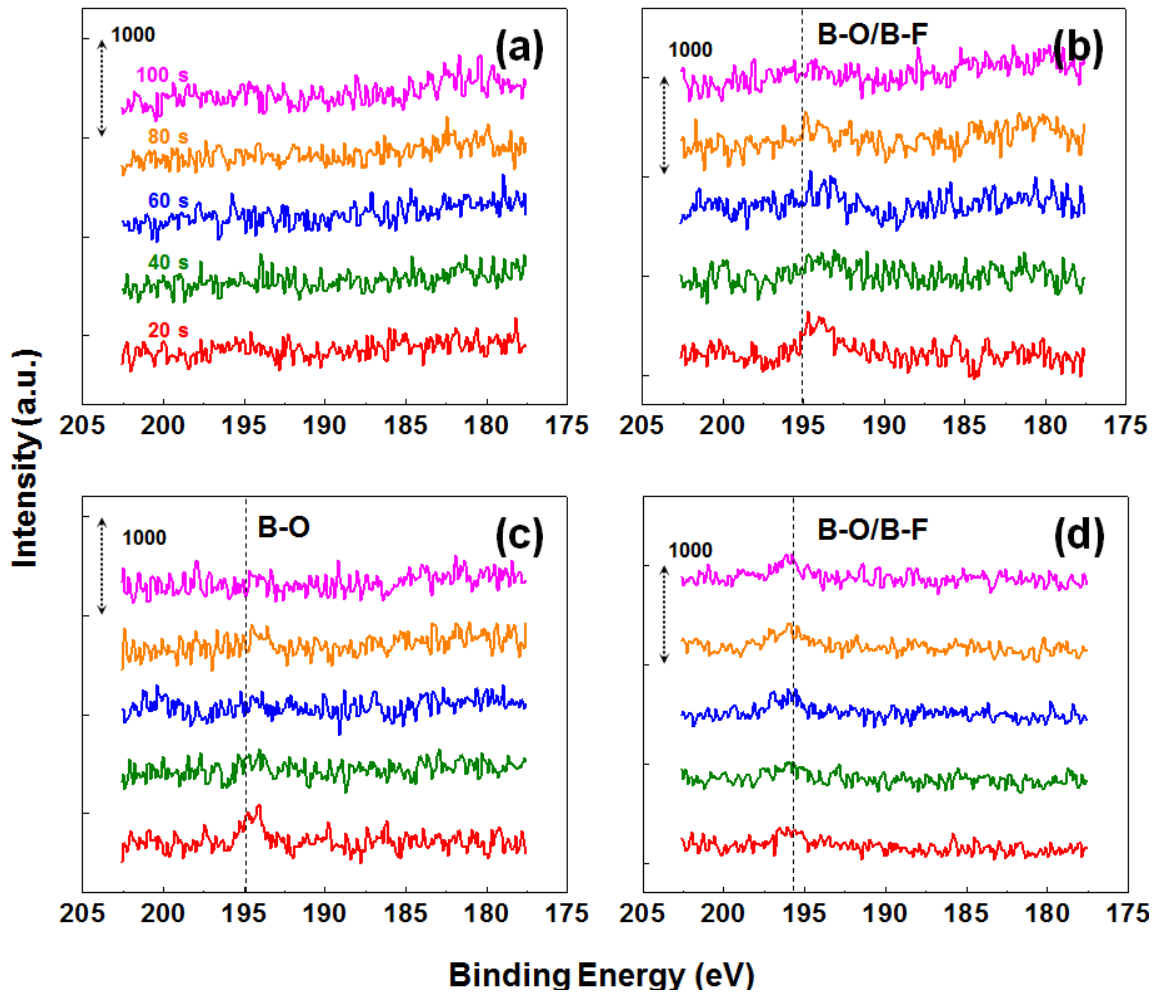


Fig. 3.7 B_{1s} XPS spectra for Al electrodes cycled in (a) LiFSI, (b) LiFSI+BF₄, (c) LiFSI+BOB, and (d) LiFSI+DFOB. The Al electrodes were cycled two times over 3–6 V (vs. Li/Li⁺) before XPS measurements. The depth profiles with increasing sputtering time (20–100 s) are compared.

Based on the analysis of surface composition, a possible explanation for the surface layer formation by borate additives is schematized in Fig. 3.8. It is assumed that LiBF₄ or LiBOB addition forms the surface layer mainly consisted of Al₂O₃ and B-O/B-F species on top of the native Al₂O₃ film. In contrast, LiDFOB additive induces a much thicker surface layer containing Al-F species in addition to Al₂O₃ and B-O/B-F components. Both the increased thickness and the corrosion resistive nature of Al-F/B-O/B-F species seem to contribute to the superior inhibition ability of LiDFOB.

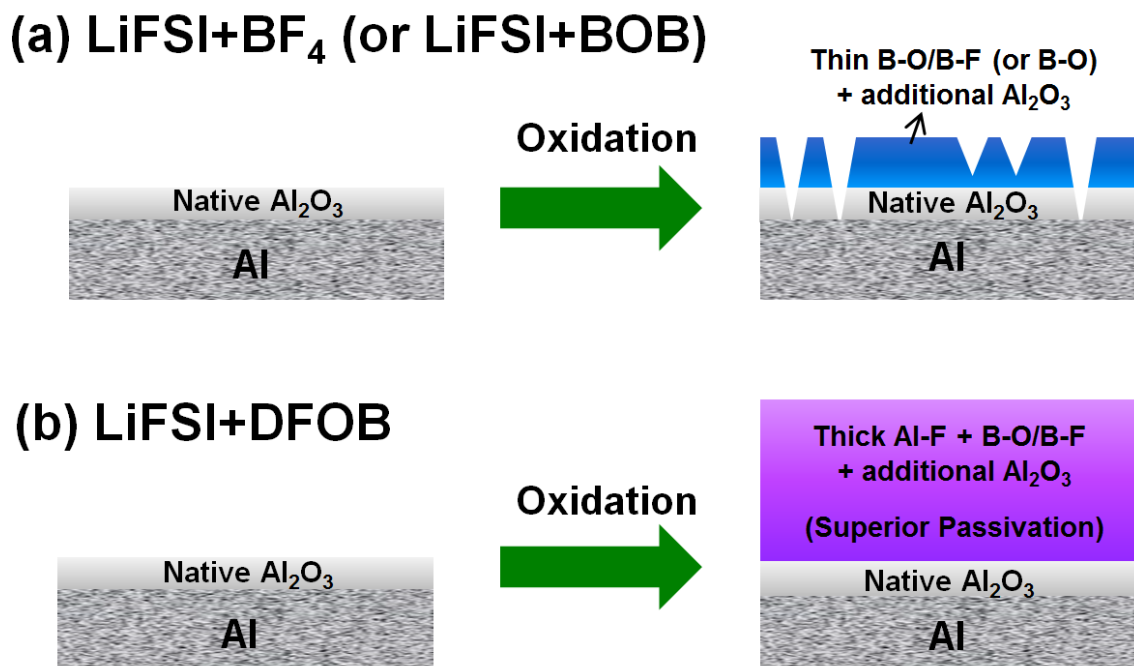


Fig. 3.8 Schematic diagram of passive layer formation on an Al electrode cycled in (a) LiFSI+BF₄ or LiFSI+BOB and (b) LiFSI+DFOB.

3.3.3 LiCoO₂ cell performances

Before performing the LiCoO₂ cell tests, the ionic conductivities of LiFSI, LiFSI+DFOB, and LiPF₆ solutions are examined over 10–60 °C (Fig. 3.9).

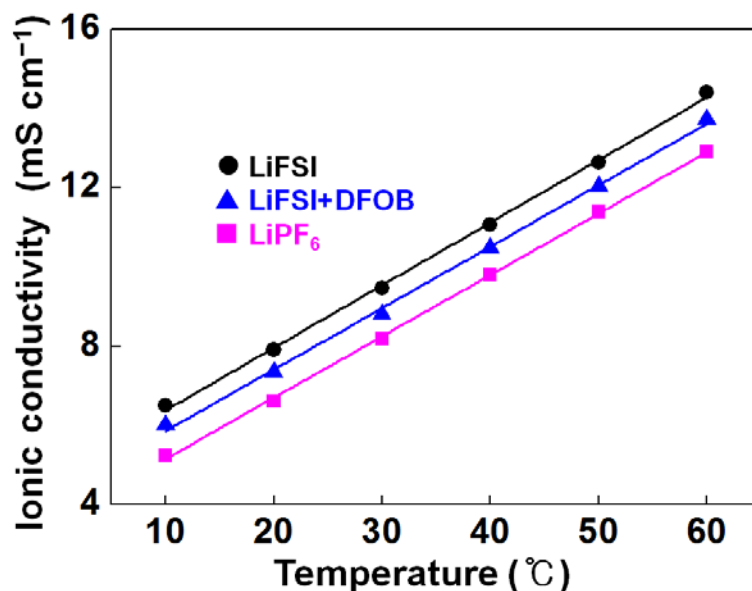


Fig. 3.9 Ionic conductivities for LiFSI, LiFSI+DFOB, and LiPF₆ measured over 10–60 °C.

LiFSI solution shows the higher ionic conductivity than LiPF₆ electrolyte which is consistent with the prior results [18, 34]. Moreover, the ionic conductivity of LiFSI+DFOB electrolyte is still higher than that of LiPF₆ solution indicating that LiDFOB addition does not significantly impair the highly conductive nature of LiFSI-based electrolytes.

The rate capabilities of LiCoO₂/graphite cells were evaluated for LiFSI, LiFSI+DFOB, and LiPF₆ (Fig. 3.10). The specific discharge capacities of the cells are not appreciably altered by the types of the electrolyte up to 0.5 C current (Fig. 3.10a).

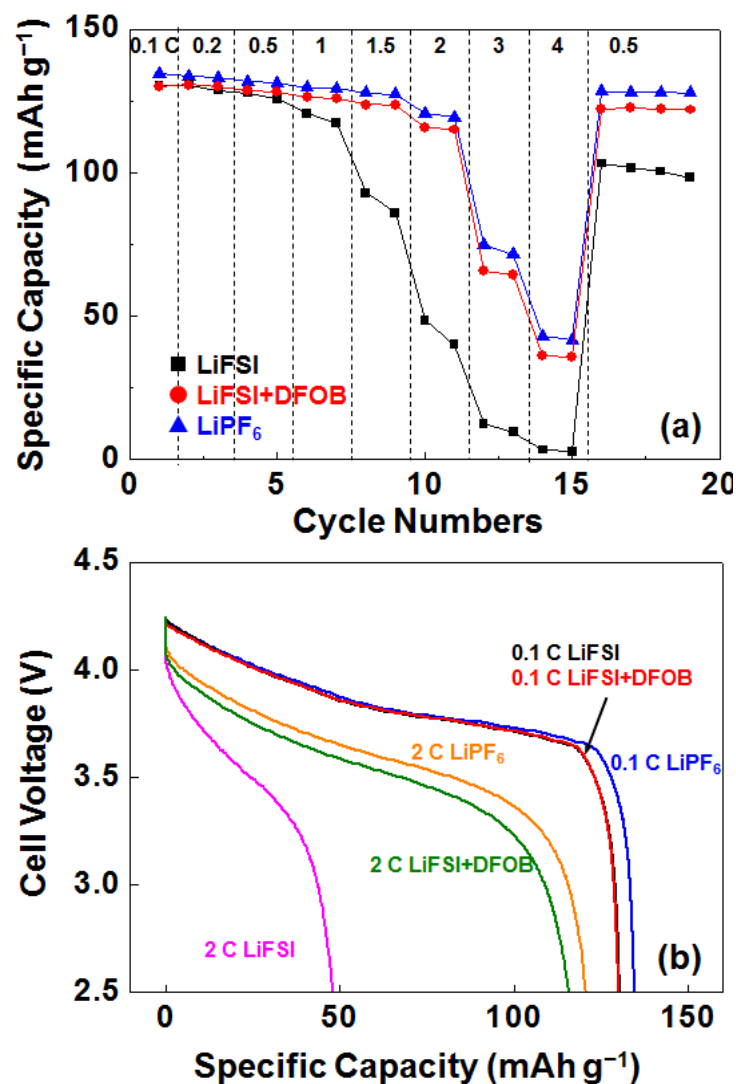


Fig. 3.10 Rate performances of LiCoO₂/graphite cells with LiFSI, LiFSI+DFOB, and LiPF₆ (a) specific discharge capacities at various C-rates and (b) cell voltage profiles at 0.1 C and 2 C discharge currents.

In a cell with LiFSI, however, the capacity decay becomes much more severe, especially above 1.5 C. In contrast, a LiFSI+DFOB and a LiPF₆ cells show much better rate performance than a LiFSI cell. In the discharge profiles (Fig. 3.10b), no significant difference is noted for the three electrolytes at a low current of 0.1 C. As the current density increases, however, a LiFSI cell suffers from huge overpotential, ending up with greatly reduced discharge capacity at 2 C current. Considering the facts that the ionic conductivity of LiFSI is higher than other two electrolytes (Fig. 3.9), and that LiFSI was reported to improve the charge transport rate of a graphite and Li metal anode [17, 36, 37], the poor rate capability of a LiFSI cell is supposed to be due to

sluggish charge transport kinetics at the cathode side.

3.3.4 Internal resistance analysis of LiCoO₂ cell

To confirm this, the charge transport behavior at the cathode was investigated using EIS. LiCoO₂/LiCoO₂ symmetric cells were employed for the EIS measurements to exclude interference from anode responses (Fig. 3.11a). The impedance spectra of a LiCoO₂/LiCoO₂ symmetric cell with LiFSI+DFOB and with LiPF₆ exhibit two semi-circles in the high (characteristic frequency of ca. 4 kHz) and middle (ca. 10 Hz) frequency regions, and an inclined line at the low frequency end (inset in Fig. 3.11a). On the other hand, a LiFSI cell shows a huge semi-circle in a low (ca. 50 mHz) frequency region in addition to one in a high (ca. 10 Hz) frequency regime. The EIS spectra were fitted with an equivalent circuit (Fig. 3.11b), where R_s is the ohmic resistance, R_l the resistance related to the migration of the Li⁺ ion through the surface film, and R_2 the interfacial charge transfer resistance [38, 39]. The capacitances associated with R_l and R_2 are represented by the constant phase elements (CPEs), Q_l and Q_2 , respectively. The finite diffusion by a CPE, Q_D , is used to replace a Warburg element to fit the inclined line at the lowest frequency region [40, 41]. The fitted resistance values are given in Table 3.1.

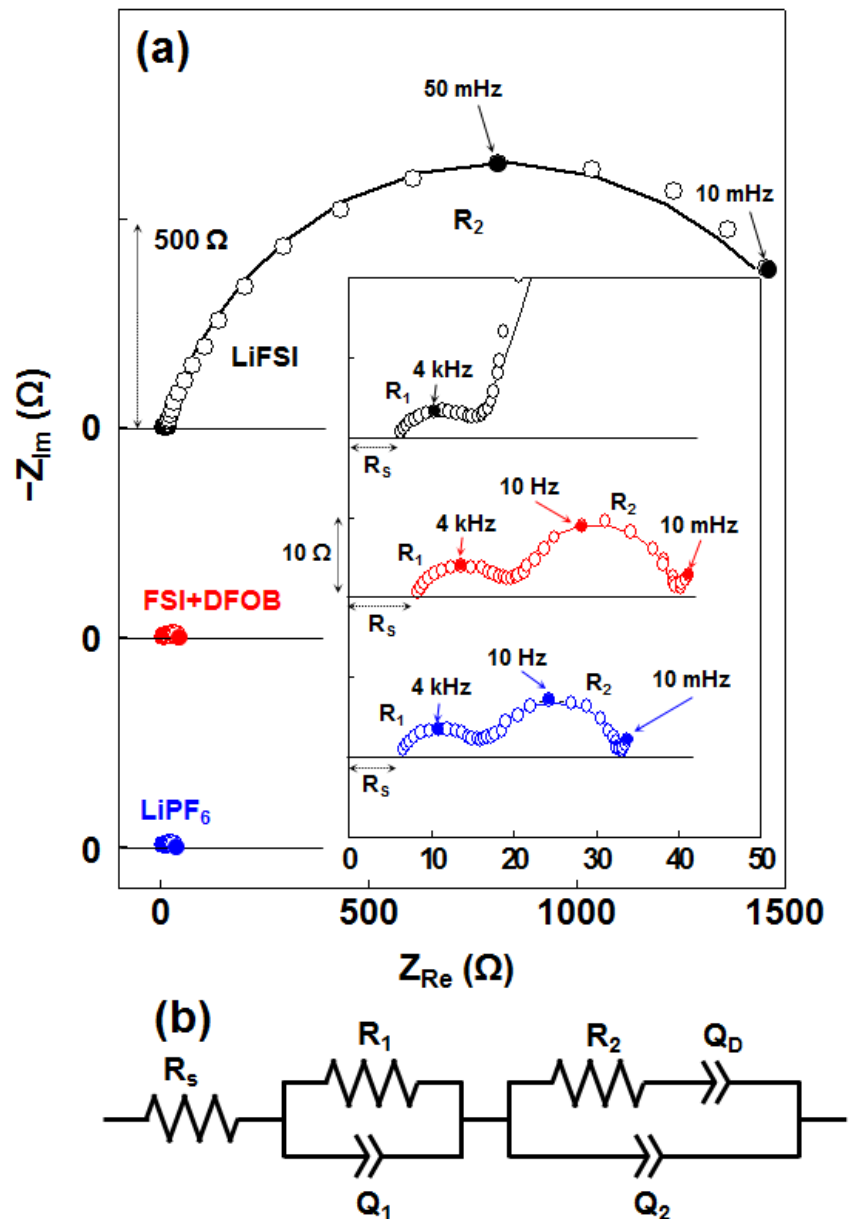


Fig. 3.11 Electrochemical impedance spectra of (a) LiCoO₂/LiCoO₂ symmetric cell with LiFSI, LiFSI+DFOB, and LiPF₆, and (b) equivalent circuit employed for the fitting of impedance spectra. The experimental spectra are denoted with circles and the best-fitted results using the equivalent circuit with solid lines.

Table 3.1 Fitted parameter values for the impedance spectra of Fig. 3.11

Resistance (Ω)	LiFSI	LiFSI+DFOB	LiPF ₆
R_s	6.0	8.0	6.3
R_l	8.7	11.3	8.3
R_2	>1500	16.7	16.3

All the three types of cells show similar R_s and R_l values. A LiFSI cell, however, shows much larger (ca. two order of magnitude) R_2 value than the other cells. In contrast, a LiFSI+DFOB cell shows quite similar R_2 value to a LiPF₆ cell, which is consistent with the comparable rate performances of the two cells. Therefore, it is evident that the poor rate capability of a LiFSI cell is mainly due to the enlarged R_2 value and, thus, the slow interfacial charge transfer at the LiCoO₂ cathode. Based on these results, it can be concluded that the addition of LiDFOB prevents Al corrosion and, thus, the contact loss at Al collector/active material interface, thereby suppressing an increase in the EIS of the cathode and eventually enabling the facile charge transport of LiCoO₂ cells.

3.3.5 Discussion

All the results obtained in this study indicate that the innate highly conductive and HF-free nature of LiFSI solutions and the Al corrosion-immunity can be successfully integrated with the aid of LiDFOB additive. This crucial finding is expected to eventually lead to the superior long-term stability of the current LIBs without compromising the energy/power densities. LiDFOB additive is also expected to be effective in the prevention of Al corrosion in FSI-based ionic liquids as well. In addition, the absence of LiPF₆ may ease the strict regulation of the moisture level in the present fabrication processes, which will contribute to a reduction in LIB manufacturing cost. All of these points could be interesting topics for future study.

As expected, the inhibition effect of LiDFOB additive is proportional to its content: as LiDFOB concentration is reduced below 0.2 M in 0.8 M LiFSI solution, the Al corrosion becomes worse accordingly (Fig. 3.12).

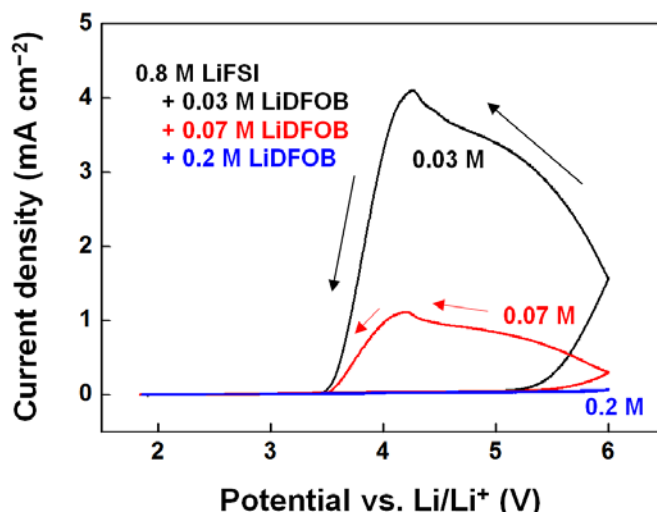


Fig. 3.12 CVs of Al electrodes at the first cycle in 0.8 M LiFSI+0.03 M LiDFOB (black), 0.8 M LiFSI+0.07M LiDFOB (red), and 0.8 M LiFSI+0.2 M LiDFOB (blue) in EC/DEC (3/7, v/v).

This study, however, was not intended to define the threshold concentration of LiDFOB, above which Al corrosion is completely suppressed, because the Al corrosion behavior is subjected to significant variation by the experimental parameters (e.g., the influence of Al surface condition as already confirmed in Fig. 3.1). In-

stead, this study tried to emphasize that, since LiDFOB exhibits the best inhibition ability when used at the same concentration (0.2 M in this study), the threshold amount of LiDFOB will be obviously less than those of the other additives, which will minimize the loss of the ionic conductivity of LiFSI-based electrolytes caused by introducing the additive.

While this study demonstrates the remarkable inhibition ability of LiDFOB, which is seemingly associated with the distinct composition of the surface layer, the fundamental reason for the prominent effect of LiDFOB compared to its borate analogues (i.e., LiBF₄, LiBOB) may well deserve further study. In this context, we could learn lessons from the recent studies on the protective layer formation by LiDFOB on the high voltage cathodes [42–45]. It was reported that LiDFOB decomposes at 4.35 V (vs. Li/Li⁺) and facilitates passivation film formation on LiCoPO₄ electrodes [42]. In addition, an oxidative decomposition mechanism of LiDFOB was proposed to explain a marked improvement in the electrochemical performance of cells containing Li_{1.2}Ni_{0.15}Mn_{0.55}Co_{0.1}O₂-based cathode [43–45]. It was also claimed that LiDFOB can passivate the metal oxide cathode electrodes much more efficiently than LiBOB due to the formation of oxidation-resistant difluoroborane (CO₂BF₂)₂ dimer [44]. In a similar manner, it can be assumed that LiDFOB is oxidized to passivate the Al surface more easily than the other borates, and the resulting surface layer has superior passivating ability. Another possibility is the higher chemical reactivity of LiDFOB. Recent studies have reported the ligand exchange reaction of LiDFOB, which establishes a thermally-induced equilibrium as follows: 2LiDFOB ↔ LiBF₄ + LiBOB [46, 47]. The released ligands (i.e., fluorine and oxalate moiety) from DFOB⁻ anion, owing to their reactive natures, would result in increased surface layer formation. However, the extent of the ligand exchange reaction is supposed to be insignificant at room temperature considering the high activation barrier for the conversion reaction of LiDFOB (ca. 137 kJ mol⁻¹) [46], which causes us to exclude this possibility.

3.4 Conclusions

We systematically investigated the inhibition effects of borate (LiBF_4 , LiDFOB , and LiBOB) and LiPF_6 additives on anodic Al corrosion in LiFSI-based electrolyte. Among the additives, LiDFOB was revealed to be an excellent Al corrosion inhibitor through CV and CA experiments. The anodic corrosion behavior of Al in 0.8 M LiFSI+0.2 M LiDFOB EC/DEC (1/2, v/v) was comparable to that of a corrosion-free 1 M LiPF_6 solution. The XPS depth analysis revealed that, compared to the other borate additives, LiDFOB additive derives a thick surface layer composed of Al-F, B-O/B-F, and Al_2O_3 , which is suggested to contribute the superior inhibition ability against Al corrosion in LiFSI-based electrolyte. The rate performance and EIS measurements confirmed that a cell with 0.8 M LiFSI+0.2 M LiDFOB electrolyte exhibits a comparable rate capability to a cell with 1 M LiPF_6 due to the excellent inhibition ability of LiDFOB for Al corrosion. This study suggests a promising strategy to tune LiFSI-based electrolytes to be free from Al corrosion, a major bottleneck for the wide use of LiFSI.

3.5 References

- [1] S.T. Myung, Y. Hitoshi, Y.K. Sun, Electrochemical behavior and passivation of current collectors in lithium-ion batteries, *J. Mater. Chem.* 21 (2011) 9891–9911.
- [2] J.M. Tarascon, M. Armand, Issues and challenges facing rechargeable lithium batteries, *Nature* 414 (2001) 359–367.
- [3] J.M. Tarascon, M. Armand, Building better batteries, *Nature* 451 (2008) 652–657.
- [4] Y.K. Sun, S.T. Myung, B.C. Park, J. Prakash, I. Belharouak, K. Amine, High-energy cathode material for long-life and safe lithium batteries, *Nat. Mater.* 8 (2009) 320–324.
- [5] M. Morita, T. Shibata, N. Yoshimoto, M. Ishikawa, Anodic behavior of aluminum in organic solutions with different electrolytic salts for lithium ion batteries, *Electrochim. Acta* 47 (2002) 2787–2793.
- [6] D.H. Jang, S.M. Oh, Electrolyte effects on spinel dissolution and cathodic capacity losses in 4 V Li/Li_xMn₂O₄ rechargeable cells, *J. Electrochem. Soc.* 144 (1997) 3342–3348.
- [7] J. Vetter, P. Novak, M.R. Wagner, C. Veit, K.C. Moller, J.O. Besenhard, M. Winter, M. Wohlfahrt-Mehrens, C. Vogler, A. Hammouche, Ageing mechanisms in lithium-ion batteries, *J. Power Sources* 147 (2005) 269–281.
- [8] E. Wang, D. Ofer, W. Bowden, N. Iltchev, R. Moses, K. Brandt, Stability of lithium ion spinel cells, *J. Electrochem. Soc.* 147 (2000) 4023–4028.
- [9] S.Y. Li, P.H. Ma, X.L. Cui, Q.D. Ren, F.Q. Li, Studies on the thermal decomposition kinetics of LiPF₆ and LiBC₄O₈, *J. Chem. Sci.* 120 (2008) 289–292.
- [10] M. Dahbi, F. Ghamouss, F. Trans-Van, D. Lemordant, M. Anouti, Comparative study of EC/DMC LiTFSI and LiPF₆ electrolytes for electrochemical storage, *J. Power Sources* 196 (2011) 9743–9750.
- [11] H. Han, J. Guo, D. Zhang, S. Feng, W. Feng, J. Nie, Z. Zhou, Lithium (fluorosulfonyl)(nonafluorobutanesulfonyl)imide (LiFNFSI) as conducting salt to improve the high-temperature resilience of lithium-ion cells, *Electrochem. Commun.* 13 (2011) 265–268.
- [12] S.T. Myung, H. Natsui, Y.K. Sun, H. Yashiro, Electrochemical behavior of Al in a non-aqueous alkyl carbonate solution containing LiBOB salt, *J. Power Sources* 195 (2010) 8297–8301.

- [13] Z. Chen, Y. Qin, J. Liu, K. Amine, Lithium difluoro(oxalato)borate as additive to improve the thermal stability of lithiated graphite, *Electrochem. Solid-State Lett.* 12 (2009) A69–A72.
- [14] S. Zugmann, D. Moosbauer, M. Amereller, C. Schreiner, F. Wudy, R. Schmitz, R. Schmitz, P. Isken, C. Dippel, R. Muller, M. Kunze, A. Lex-Balducci, M. Winter, H.J. Gores, Electrochemical characterization of electrolytes for lithium-ion batteries based on lithium difluoromono(oxalato)borate, *J. Power Sources* 196 (2011) 1417–1424.
- [15] J. Liu, Z. Chen, S. Busking, K. Amine, Lithium difluoro(oxalato)borate as a functional additive for lithium-ion batteries, *Electrochem. Commun.* 9 (2007) 475–479.
- [16] Q. Wu, W. Lu, M. Miranda, T. K. Honaker-Schroeder, K. Y. Lakhsassi, D. Dees, Effects of lithium difluoro(oxalate)borate on the performance of Li-rich composite cathode in Li-ion battery, *Electrochem. Commun.* 24 (2012) 78–81.
- [17] A. Guerfi, S. Duchesne, Y. Kobayashi, A. Vijn, K. Zaghib, LiFePO₄ and graphite electrodes with ionic liquids based on bis(fluorosulfonyl)imide (FSI)[−] for Li-ion batteries, *J. Power Sources* 175 (2008) 866–873.
- [18] L. Li, S. Zhou, H. Han, H. Li, J. Nie, M. Armand, Z. Zhou, X. Huang, Transport and electrochemical properties and spectral features of non-aqueous electrolytes containing LiFSI in linear carbonates solvents, *J. Electrochem. Soc.* 158 (2011) A74–A82.
- [19] A. Abouimrane, J. Ding, I.J. Davidson, Liquid electrolytes based on lithium bis-fluorosulfonyl imide salt: Aluminum corrosion studies and lithium ion battery investigations, *J. Power Sources* 189 (2009) 693–696.
- [20] E. Kramer, S. Passerini, M. Winter, Dependency of aluminum collector corrosion in lithium ion batteries on the electrolyte solvent, *ECS Electrochem. Lett.* 1 (2012) C9–C11.
- [21] M. Morita, T. Shibata, N. Yoshimoto, M. Ishikawa, Anodic behavior of aluminum current collector in LiTFSI solutions with different solvent compositions, *J. Power Sources* 119–121 (2003) 784–788.
- [22] X. Wang, E. Yasukawa, S. Mori, Inhibition of anodic corrosion of aluminum cathode current collector on recharging in lithium imide electrolytes, *Electrochim. Acta* 45 (2000) 2677–2684.
- [23] T. Kawamura, T. Tanaka, M. Egashira, I. Watanabe, S. Okada, J. Yamaki, Methyl difluoroacetate inhibits corrosion of aluminum cathode current collector for lithium ion cells, *Electrochem. Solid-State Lett.* 8 (2005) A459–A463.

- [24] H. Louis, Y.G. Lee, K.M. Kim, W.I. Cho, J.M. Ko, Suppression of aluminum corrosion in lithium bis(trifluoromethanesulfonyl)imide-based electrolytes by the addition of fumed silica, *Bull. Korean Chem. Soc.* 34 (2013) 1795–1799.
- [25] A. Hofmann, M. Schulz, V. Winkler, T. Hanemann, Anodic aluminum dissolution in conducting salt containing electrolytes for lithium-ion batteries, *J. Electrochem. Soc.* 161 (2014) A431–A438.
- [26] R.S. Kuhnel, M. Lubke, M. Winter, S. Passerini, A. Balducci, Suppression of aluminum current collector corrosion in ionic liquid containing electrolytes, *J. Power Sources* 214 (2012) 178–184.
- [27] J. Kalhoff, D. Bresser, M. Bolloli, F. Alloin, J.Y. Sanchez, S. Passerini, Enabling LiTFSI-based electrolytes for safer lithium-ion batteries by using linear fluorinated carbonates as (co)solvent, *ChemSusChem* 7 (2014) 2939–2946.
- [28] K. Matsumoto, K. Inoue, K. Nakahara, R. Yuge, T. Noguchi, K. Utsugi, Suppression of aluminum corrosion by using high concentration LiTFSI electrolyte, *J. Power Sources* 231 (2013) 234–238.
- [29] D.W. McOwen, D.M. Seo, O. Borodin, J. Vatamanu, P.D. Bolye, W.A. Henderson Concentrated electrolytes: decrypting electrolyte properties and reassessing Al corrosion mechanisms, *Energy Environ. Sci.* 7 (2014) 416–426.
- [30] E. Cho, J. Mun, O.B. Chae, O. Kwon, H. Kim, J. Ryu, Y. Kim, S.M. Oh, Corrosion/passivation of aluminum current collector in bis(fluorosulfonyl) imide-based ionic liquid for lithium-ion batteries, *Electrochem. Commun.* 22 (2012) 1–3.
- [31] S.W. Song, T.J. Richardson, G.V. Zhuang, T.M. Devine, J.W. Evans, Effect on aluminum corrosion of LiBF₄ addition into lithium imide electrolyte; a study using the EQCM, *Electrochim. Acta* 49 (2004) 1483–1490.
- [32] X. Zhang, T.M. Devine, Passivation of aluminum in lithium-ion battery electrolytes with LiBOB, *J. Electrochem. Soc.* 153 (2006) B365–B369.
- [33] X. Chen, W. Xu, M.H. Engelhard, J. Zheng, Y. Zhang, F. Ding, J. Qian, J.G. Zhang, Mixed salts of LiTFSI and LiBOB for stable LiFePO₄-based batteries at elevated temperatures, *J. Mater. Chem. A* 2 (2014) 2346–2352.
- [34] H. Han, S. Zhou, D. Zhang, S. Feng, L. Li, K. Liu, W. Feng, J. Nie, H. Li, X. Huang, M. Armand, Z.

Zhou, Lithium bis(fluorosulfonyl)imide (LiFSI) as conducting salt for nonaqueous liquid electrolytes for lithium-ion batteries: Physicochemical and electrochemical properties, *J. Power Sources* 196 (2011) 3623–3632.

[35] M. Markovsky, F. Amalraj, H.E. Gottlieb, Y. Gofer, S.K. Martha, D. Aurbach, On the electrochemical behavior of aluminum electrodes in nonaqueous electrolyte solutions of lithium salts, *J. Electrochem. Soc.* 157 (2010) A423–A429.

[36] H. Yoon, G.H. Lane, Y. Shekibi, P.C. Howlett, M. Forsyth, A.S. Best, D.R. MacFarlane, Lithium electrochemistry and cycling behavior of ionic liquids using cyano based anions, *Energy Environ. Sci.* 5 (2013) 979–986.

[37] L. Zhang, L. Chai, L. Zhang, M. Shen, X. Zhang, V.S. Battaglia, T. Stephenson, H. Zheng, Synergistic effect between lithium bis(fluorosulfonyl)imide (LiFSI) and lithium bis-oxalato borate (LiBOB) salts in LiPF₆-based electrolyte for high-performance Li-ion batteries, *Electrochim. Acta* 127 (2014) 39–44.

[38] D. Aurbach, K. Gamolsky, B. Markovsky, Y. Gofer, M. Schmidt, U. Heider, On the use of vinylene carbonate (VC) as an additive to electrolyte solutions for Li-ion batteries, *Electrochim. Acta* 47 (2002) 1423–1439.

[39] T. Abe, H. Fukuda, Y. Iriyama, Z. Ogumi, Solvated Li-ion transfer at interface between graphite and electrolyte, *J. Electrochem. Soc.* 151 (2004) A1120–A1123.

[40] Q.C. Zhuang, T. Wei, L.L. Du, Y.L. Cui, L. Fang, S.G. Sun, An electrochemical impedance spectroscopic study of the electronic and ionic transport properties of spinel LiMn₂O₄, *J. Phys. Chem. C* 114 (2010) 8614–8621.

[41] X.Y. Qiu, Q.C. Zhuang, Q.Q. Zhuang, R. Cao, P.Z. Ying, Y.H. Qiang, S.G. Sun, Electrochemical and electronic properties of LiCoO₂ cathode investigated by galvanostatic cycling and EIS, *Phys. Chem. Chem. Phys.* 14 (2012) 2617–2630.

[42] M. Hu, J. Wei, L. Xing, Z. Zhou, Effect of lithium difluoro(oxalate)borate (LiDFOB) additive on the performance of high-voltage lithium-ion batteries, *J. Appl. Electrochem.* 42 (2012) 291–296.

[43] Y. Zhu, Y. Li, M. Bettge, D.P. Abraham, Positive electrode passivation by LiDFOB electrolyte additive in high-capacity lithium-ion cells, *J. Electrochem. Soc.* 159 (2012) A2109–A2117.

[44] I.A. Shkrob, Y. Zhu, T.W. Marin, D.P. Abraham, Mechanistic insight into the protective action of

bis(oxalato)borate and difluoro(oxalato)borate anions in Li-ion batteries, *J. Phys. Chem. C* 117 (2013) 23750–23756.

[45] Y. Zhu, Y. Li, M. Bettge, D.P. Abraham, Electrolyte additive combinations that enhance performance of high-capacity $\text{Li}_{1.2}\text{Ni}_{0.15}\text{Mn}_{0.55}\text{Co}_{0.1}\text{O}_2$ -graphite cells, *Electrochim. Acta* 110 (2013) 191–199.

[46] L. Zhou, W. Li, M. Xu, B. Lucht, Investigation of the disproportionation reactions and equilibrium of lithium difluoro(oxalato) borate (LiDFOB), *Electrochem. Solid-State Lett.* 14 (2011) A161–A164.

[47] T. Schedlbauer, U.C. Rodehorst, C. Schreiner, H.J. Gores, M. Winter, Blends of lithium bis(oxalato)borate and lithium tetrafluoroborate: Useful substitutes for lithium difluoro(oxalato)borate in electrolytes for lithium metal based secondary batteries?, *Electrochim. Acta* 107 (2013) 26–32.

IV. Wide-temperature operation of lithium metal batteries enabled by localized high-concentration electrolytes

4.1 Introduction

There is an urgent need to replace current Li-ion batteries (LIBs) with Li metal batteries (LMBs) to exploit the high theoretical capacity (3860 mAh g^{-1}) and low redox potential (-3.0 V vs. NHE) of the Li metal anode. However, the Li anode suffers from poor cyclability due to low Coulombic efficiency (CE) and severe Li dendrite formation. Recently, high-concentration electrolytes (HCEs) containing unconventionally high salt content were introduced to resolve the aforementioned issues of the Li anode. HCEs feature critical advantages, including enhanced electrochemical stability and dendrite-free Li deposition with high CE ^[1-12]. In HCEs, most solvent molecules are engaged in the solvation of Li-ions so that unwanted side reactions of uncoordinated free solvents are markedly suppressed, leading to improved Li cyclability without dendrite formation ^[2]. Nevertheless, HCEs face several critical issues, including high salt concentration, high material cost, and high viscosity. The high viscosity of HCEs results in low ionic conductivity and poor wettability of the separators and thick electrodes, which jointly impair the rate capability, particularly below room temperature ^[13].

Recently, to address the drawbacks of HCEs, localized high-concentration electrolytes (LHCEs) employing diluent co-solvents that hardly solvate Li-ions were introduced ^[13-16]. Compared to the case with HCEs, LHCEs exhibit markedly low viscosity, which improves their ionic conductivity and wettability at ambient temperature. A series of LHCE systems employing linear carbonate, trialkyl phosphate, sulfone, and glyme as the main solvent and fluorinated ether as the co-solvent ensured stable Li cycling, and thus excellent cyclability of practical high-energy LMBs. Furthermore, the flammability of LHCEs can be readily regulated by adopting non-flammable main or co-solvents, which can greatly mitigate the safety concerns associated with LMBs ^[13-15, 17-19]. Thus far, LHCEs have not been fully exploited, despite their immense potential. In particular, the possible benefits of LHCEs under harsh temperature conditions, which would drive LMBs closer to practical applications, are scarcely examined ^[13]. Moreover, the influence of the main solvent and co-solvent on the overall properties of

LHCEs needs to be further elucidated.

Therefore, in this study, we investigated glyme-based HCE and LHCE over the temperature range relevant to practical applications (5–60 °C). We employed a representative HCE consisting of a glyme solvent (1,2-dimethoxyethane, DME) with 4 M LiFSI (hereinafter denoted as gHCE) [2]. DME and 1,1,2,2-tetrafluoroethyl 2,2,3,3-tetrafluoropropyl ether (TTE) (1/2, v/v) with 1 M LiFSI was selected as a model LHCE (hereinafter denoted as gLHCE). We found that compared to the case with gHCE, gLHCE enables stable Li cycling with a high Li CE at 5 °C, 25 °C, and 60 °C. As evidenced by X-ray photoelectron spectroscopy (XPS) and Raman spectroscopy, the beneficial impact of gLHCE was ascribed to increased fractions of ion pairs and agglomerates, which can help to derive an inorganic-rich solid electrolyte interphase (SEI) on the Li anode. Finally, it was confirmed that gLHCE markedly improves the long-term cyclability and rate capability of FeS₂/Li and anode-free LiFePO₄ (LFP)/Cu cells over 5–60 °C.

4.2 Experimental

4.2.1 Chemicals

LiFSI and TTE (battery grade) were provided by Panax Etec (Korea). Anhydrous DME and FeS₂ powder (325 mesh) were purchased from Sigma-Aldrich. LFP powder ($D_{50} = 11 \mu\text{m}$) was provided by LG Chem. The preparation of gHCE and gLHCE was conducted in an Ar-filled globe box (H_2O and O_2 levels < 5 ppm and 25 ± 1 °C), and their water contents, measured by Karl-Fisher (Metrohm), were less than 20 ppm. FeS₂ and LFP powders were dried at 120 °C under vacuum for over 12 h prior to use.

4.2.2 Physicochemical properties

The ionic conductivity and viscosity of the electrolytes were measured at various temperatures using an ionic conductivity meter (MCS 10, Biologic) and a viscometer (A&D), respectively. Prior to each measurement, the electrolytes were maintained for at least 30 min at a given temperature. To assess the wettability of the electrolytes, the contact angle on the polyethylene (PE) separator (Tonen) and surface free energies of the electro-

lytes were measured using a DSA100 drop shape analyzer and K100 tensiometer (KRUSS), respectively. To evaluate the flame resistance, glass filters (Whatman) soaked in gHCE and gLHCE were directly exposed to a torch flame.

4.2.3 Electrochemical and cell tests

A three-electrode system was employed to determine the anodic stability and Al corrosion behaviors of the electrolytes. A Pt disk (1.6 mm diameter) electrode or Al rod (99.999% purity, 3.0 mm diameter) was used as the working electrode, and a Li chip and Pt wire were employed as the reference and counter electrodes, respectively. To evaluate the oxidative stability of the electrolytes, linear sweep voltammetry (LSV) was conducted at a scan rate of 1 mV s^{-1} from OCV to 5.5 V (vs. Li/Li⁺), and the Al corrosion behavior was examined via chronoamperometric measurements by applying 4.5 V (vs. Li/Li⁺) for 20 min.

Battery tests were carried out using 2032-type coin cells assembled in an Ar-filled glove box. Li/Cu cells were fabricated with a Cu disk (1.54 cm²), Li disk (2.01 cm², 450 μm thickness), PE separator, and electrolyte (100 μL). During the Li/Cu cells cycling, a fixed amount of Li was deposited on Cu and subsequently stripped up to a cutoff voltage of 1 V with a designated current density. The Li CE was calculated at each cycle, and each CE value was averaged over the total cycles to obtain an average CE. Li/Li cells were employed by integrating two identical Li disks. The cycle test of Li/Li cells was performed with a current density of 1.0 mA cm^{-2} and a capacity of 0.5 mAh cm^{-2} .

The FeS₂/Li cells were composed of an FeS₂ electrode (1.54 cm²) and Li disk. The composition of the cathode electrode was 75 wt% FeS₂ (ca. $4.3 \pm 0.1 \text{ mg cm}^{-2}$), 10 wt% conductive carbon (super-C), and 15 wt% polyvinylidene difluoride (PVDF) binder. The slurry was coated on a Cu foil and dried at 80 °C in a vacuum oven for 24 h. The cells were cycled three times at 25 °C with a 0.2 C current over a voltage range of 1–2.6 V for the formation process. A current density of 0.2 C was employed for the cycling tests at 25 °C, 0.5 C for the cycling tests at 5 °C and 60 °C, and 0.1–5 C for the rate capability tests.

For the anode-free LFP/Cu cells, coin cells with Al-clad cases (Welcos) were employed. LFP/Cu cells were composed of an LFP cathode (1.54 cm²) and a Cu disk (2.01 cm²). The cathode was fabricated on an Al foil

using LFP (ca. $13.9 \pm 0.1 \text{ mg cm}^{-2}$) with 5 wt% conductive carbon (super-C) and 5 wt% PVDF binder, followed by drying at $100 \text{ }^\circ\text{C}$ under vacuum for 24 h. The cells were cycled three times at $25 \text{ }^\circ\text{C}$ with a 0.2 C current within a cutoff voltage range of 2.8–3.8 V to complete the formation process. A current density of 0.2 C was employed for the cycling tests at $25 \text{ }^\circ\text{C}$, 0.5 C for the tests at $5 \text{ }^\circ\text{C}$ and $60 \text{ }^\circ\text{C}$, and 0.1–5 C for the rate capability tests.

4.2.4 Microscopy and spectroscopy

The surface morphologies of the Li electrodes were characterized by high-resolution field-emission scanning electron microscopy (HR FE-SEM, Hitachi) at 3 kV and $10 \text{ } \mu\text{A}$. XPS measurements were performed to analyze the composition of the Li electrode surface using ESCALAB 250Xi (Thermo Scientific). For the surface analysis, Li electrodes were collected from Li/Cu cells cycled 30 times at a current density of 0.5 mA cm^{-2} with a capacity of 1.0 mAh cm^{-2} , rinsed with DME to remove residual electrolyte, and dried for 24 h inside a glove box.

Raman spectroscopy studies of the electrolytes were conducted using a monochromator (Thermo Scientific, Nicolet Almega XR). Excitation was performed with a 780 nm line of Ar ion laser at room temperature with a resolution of 0.5 cm^{-1} .

Electrochemical impedance spectroscopy (EIS) measurements were carried out for the Li/Li cells cycled three times with a current density of 0.2 mA cm^{-2} and a capacity of 1.0 mAh cm^{-2} . The frequency range was 300 kHz–500 mHz, AC amplitude was 10 mV, and the DC bias voltage was 0.0 V.

4.3 Results and discussion

4.3.1 Physicochemical properties

Compared to the case with gHCE, gLHCE presented enhanced mass transport, wettability, and non-flammability due to the preferable nature of the TTE co-solvent; TTE features negligible solvating ability toward Li-ions, low viscosity (2.15 cP at 25 °C), and excellent fire-resistance. First, the ionic conductivities of gHCE and gLHCE were compared over $-25-60$ °C (Fig. 4.1a). gLHCE notably displayed higher ionic conductivity than that of gHCE below 30 °C. In particular, gLHCE presented ca. seven times higher ionic conductivity than that of gHCE at -25 °C (1.5 vs. 0.2 mS cm⁻¹, respectively). The ionic conductivity of gLHCE was lower than that of gHCE over 30 °C, but it was still high enough for practical applications (7.6 mS cm⁻¹ at 30 °C and 10.9 mS cm⁻¹ at 60 °C). In addition, gLHCE exhibited a much lower viscosity than that of HCE over the investigated temperature range (5–55 °C), as seen in Fig. 1b (4.9 cP vs. 36.2 cP at 25 °C, respectively). According to the Vogel-Tammann-Fulcher (VTF) plots (Fig. 4.2), gLHCE exhibited relatively low activation energies for the ionic conductivity (E_a^{ic}) and viscosity (E_a^{vis}) (1.80 vs. 4.21 for E_a^{ic} and 0.29 vs. 0.49 kJ mol⁻¹ for E_a^{vis}), suggesting that the enhanced ion conduction and fluidity of gLHCE may be associated with the transport mechanism altered by the presence of the TTE co-solvent.

Besides the improved transport properties, gLHCE exhibited markedly improved wettability toward conventional PE separators compared with the case of gHCE (Figs. 4.1c and 4.1d). Notably, gLHCE penetrated into the separators more rapidly than gHCE did and showed a lower contact angle on the separator (21.2° vs. 59.4°). The enhanced penetration and spreading of gLHCE can be attributed to its low viscosity (Fig. 4.1b) and low surface free energy (43.2 vs. 55.5 mJ m⁻², Table 4.1), respectively [20, 21].

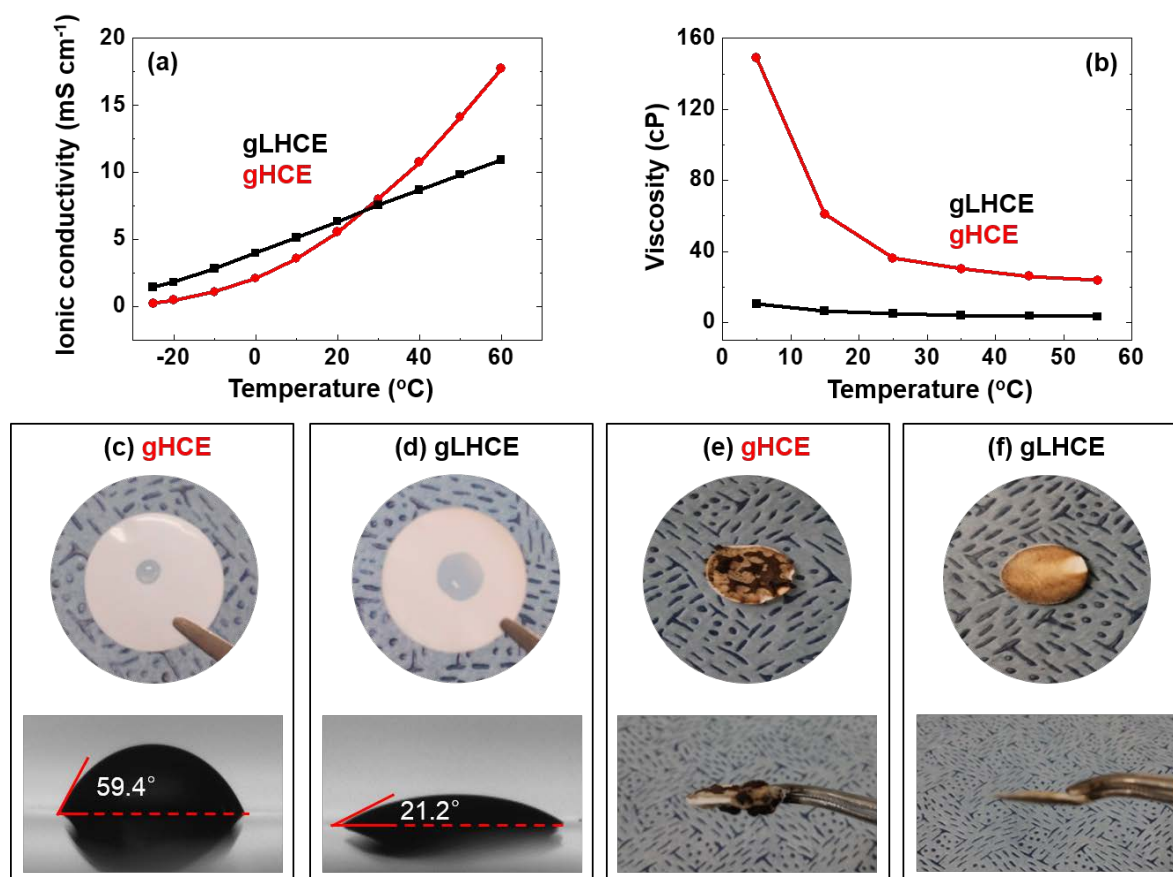


Fig. 4.1 (a) Ionic conductivities and (b) viscosities of gLHCE and gHCE at various temperatures. Photos of (c) gHCE and (d) gLHCE on a PE separator. Photos of a glass filter soaked with (e) gHCE and (f) gLHCE after the flame test.

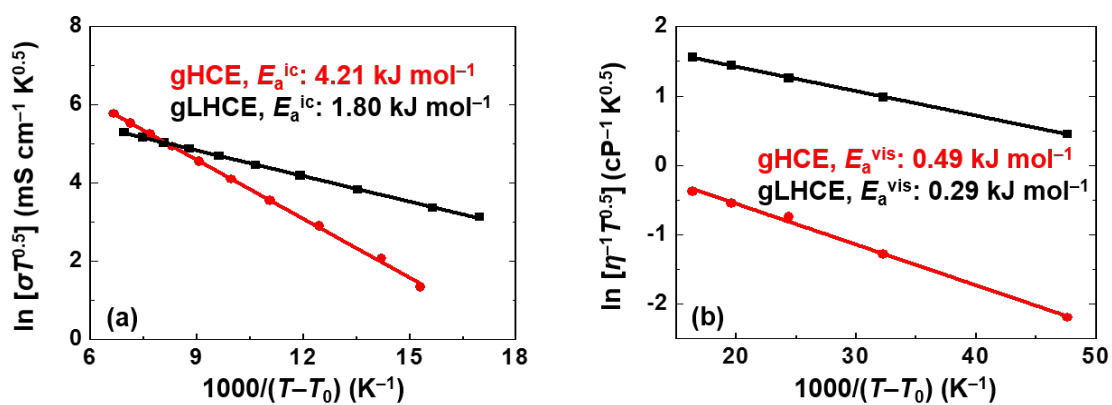


Fig. 4.2 Vogel-Tammann-Fulcher (VTF) plots of (a) Ionic conductivity and (b) viscosity of gHCE and gLHCE. Solid lines denote the best-fitting results of the VTF equation.

Table 4.1 Contact angle and surface tension of the electrolytes.

Electrolyte	Contact angle (degree)	Surface free energy (mJ m^{-2})
gHCE	59.4	55.5
gLHCE	21.2	43.2

4.3.2 Thermal and electrochemical stability

In addition, gLHCE inherited the non-flammable nature of TTE. After being exposed to the torch flame, the gHCE content contained in a glass filter was ignited immediately and burnt out completely (Fig. 4.1e). By contrast, gLHCE took a much longer time to be ignited, and exhibited self-extinguishing behavior when the torch was removed (Fig. 4.1f).

The oxidation behavior of gLHCE was comparable or slightly better than that of gHCE (Fig. 4.3). The corrosion of Al current collectors, a chronic issue associated with the Li-imide salt, was also examined (Fig. 4.3b). It was claimed that HCEs markedly suppress the Al corrosion^[22]. However, in gHCE, the corrosion current at an applied potential of 4.8 V (vs. Li/Li⁺) was gradually revived as the polarization time increased above 5 min. By contrast, the Al oxidation remained insignificant in gLHCE up to 20 min, indicating a superior corrosion inhibition ability of gLHCE compared to that of gHCE.

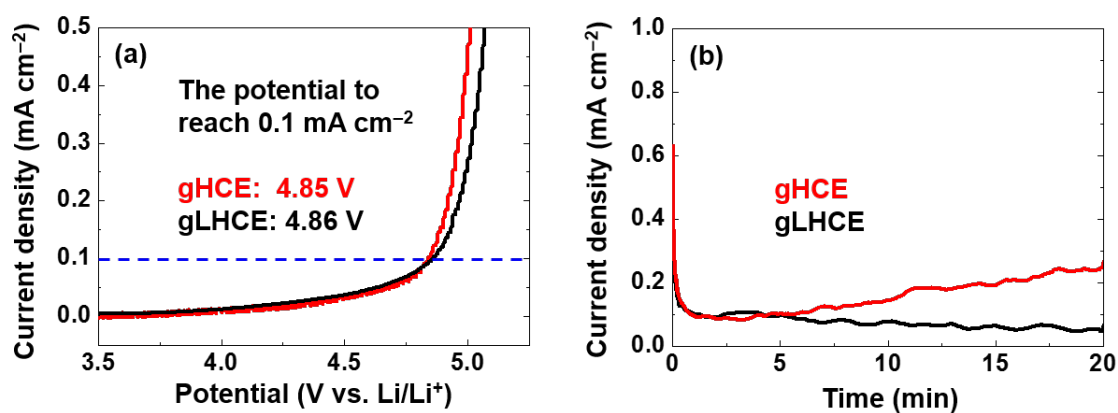


Fig. 4.3 (a) Linear sweep voltammograms in an anodic region on a Pt working electrode. (b) Chronoamperograms on an Al working electrode with an applied potential of 4.8 V (vs. Li/Li⁺).

4.3.3 Electrolyte optimization for Li cycling

To select an optimum combination of the main and co-solvent of gLHCE, we investigated the effects of the types of glyme and fluorinated ether solvents on the Li cycling performance using Li/Cu cells (Fig. 4.4). When DME in gLHCE was replaced with diglyme or triglyme, the Li cyclability deteriorated significantly (Fig. 4.4a), implying a negative influence of the long-chain glyme solvents. In addition, fluorinated ethers other than TTE, shorter (TTrE and BTfE) or longer (TOE), were found to be inferior to TTE (Fig. 4.4b). Recently, it was reported that fluorinated ethers could be divided into three groups based on their Li-solvating power^[23]. According to their classification, TTE and TTrE belong to the same group, displaying the lowest Li-solvating ability, while BTfE belongs to the group with the highest solvating power. This can rationalize the lowest Li CE value of BTfE observed in our study. However, the high Li CE in TTE compared to that in TTrE is not consistent with the classification, implying that the Li-solvating ability cannot be the only factor that determines the Li CE. The relative ratio of DME to TTE was also found to be a critical factor: 1:2 volume ratio (i.e., in gLHCE) displayed better Li cycling performance, resulting in lower accumulated Coulombic inefficiency ($\sum(100-CE_i)$; CE_i is the CE at the i^{th} cycle)^[24, 25] compared to the cases with 1:1 and 1:4 ratios (Fig. 4.5). While the Li cycling behavior associated with the 1:3 ratio was comparable to that associated with the volume ratio in gLHCE, gLHCE presented a relatively high ionic conductivity (6.9 vs. 5.4 mS cm⁻¹), and thus, it was employed in the following tests.

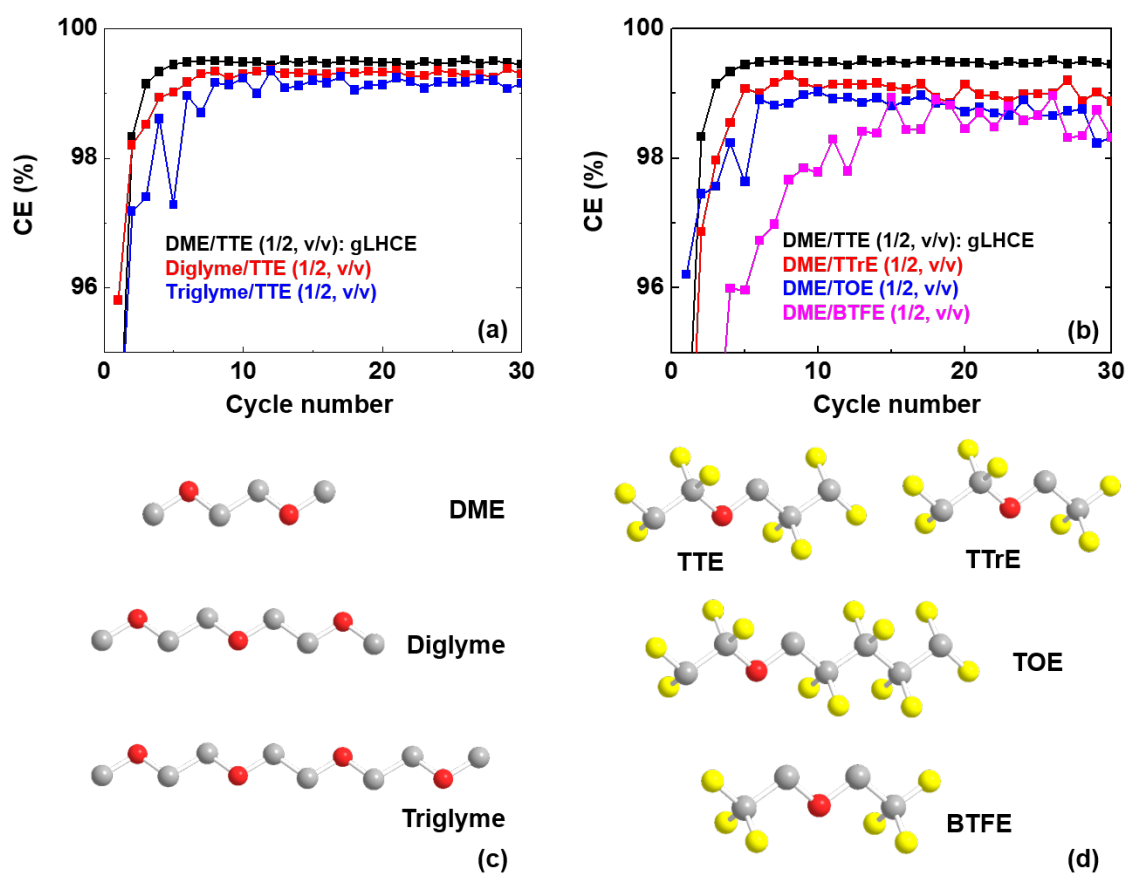


Fig. 4.4 The Li CE of the Li/Cu cells cycled in (a) various glymes with TTE and (b) fluorinated ethers with DME. Li deposition capacity was 1.0 mAh cm^{-2} with a current density of 0.5 mA cm^{-2} . The chemical structure of (c) DME, diglyme, triglyme and (d) fluorinated ethers: 1,1,2,2-tetrafluoroethyl 2,2,3,3-tetrafluoropropyl ether (TTE), 1,1,2,2-tetrafluoroethyl 2,2,2-trifluoroethyl ether (TTrE), 1,1,2,2-tetrafluoroethyl 2,2,3,3,4,4,5,5-octatetrafluoropentyl ether (TOE), and bis(2,2,2-trifluoroethyl) ether (BTFE). All the electrolytes contain 1 M LiFSI.

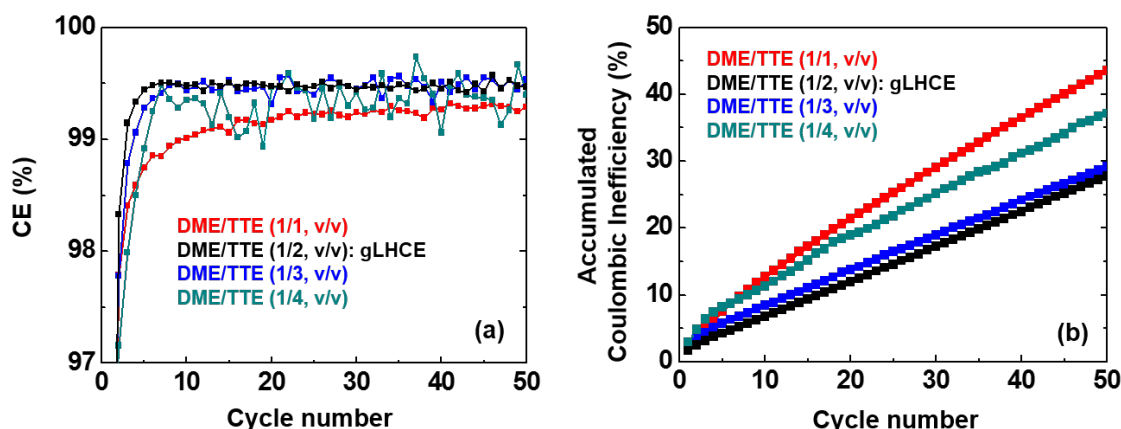


Fig. 4.5 (a) The Li CE and (b) accumulated Coulombic inefficiency of the Li/Cu cells cycled in DME/TTE with the volume ratio from 1:1 to 1:4. Li deposition capacity was 1.0 mAh cm^{-2} with a current density of 0.5 mA cm^{-2} .² All the electrolytes contain 1 M LiFSI.

4.3.4 Li cycling performances at various conditions

At the next step, the Li cycling behaviors of the Li/Cu cells using gHCE and gLHCE were compared under various conditions. As seen in Fig. 4.6, the CE values of the Li/Cu cells increased initially and stabilized at the following cycles. At a current density of 0.2 mA cm^{-2} (Fig. 4.6a), the CE value averaged over the 200 cycles was 99.09% for a Li/Cu cell with gHCE, which is close to the previously reported value^[2]. Notably, the CE value of a cell with gLHCE was stabilized relatively rapidly and attained a relatively high average value of 99.40%. Even a slight difference in the CE value, during accumulation, would cause a significant disparity in the long-term cycling of the LMBs^[24, 25]. Indeed, as shown in Fig. 4.7a, the accumulated Coulombic inefficiency during the 200 cycles was much lower in a cell with gLHCE than in that with gHCE (120.4% vs. 180.4%). The improved Li cycling efficiency in gLHCE was also confirmed at a relatively high current density of 2.0 mA cm^{-2} (Fig. 4.6b); a higher average CE (99.07% vs. 98.71%) and lower accumulated Coulombic inefficiency (186.3% vs. 258.5%) were obtained in gLHCE (Fig. 4.7b).

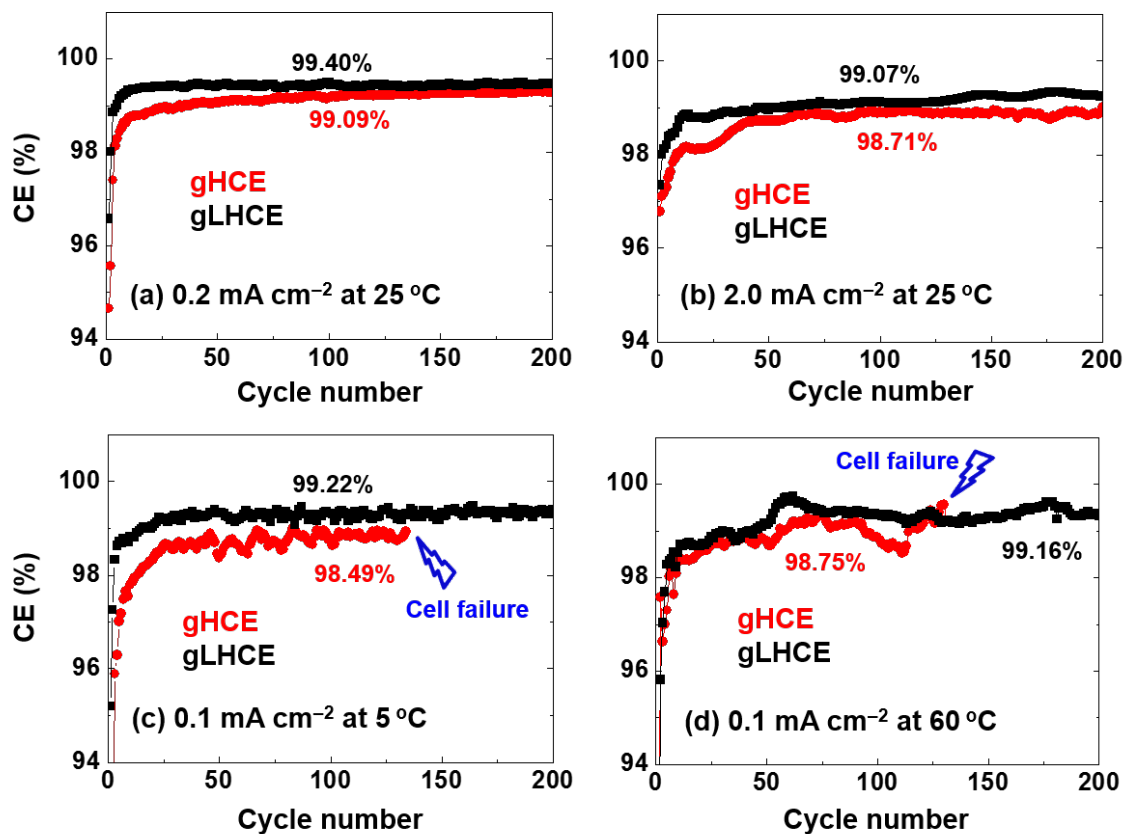


Fig. 4.6 Coulombic efficiency (CE) of Li/Cu cells at 25 °C cycled with a current density of (a) 0.2 mA cm⁻² and (b) 2.0 mA cm⁻². CE of the Li/Cu cells cycled at (c) 5 °C and (d) 60 °C with a current density of 0.1 mA cm⁻². The Li deposition capacity was 0.5 mAh cm⁻². The cell with gHCE failed during the 135th cycle at 5 °C and during the 132nd cycle at 60 °C.

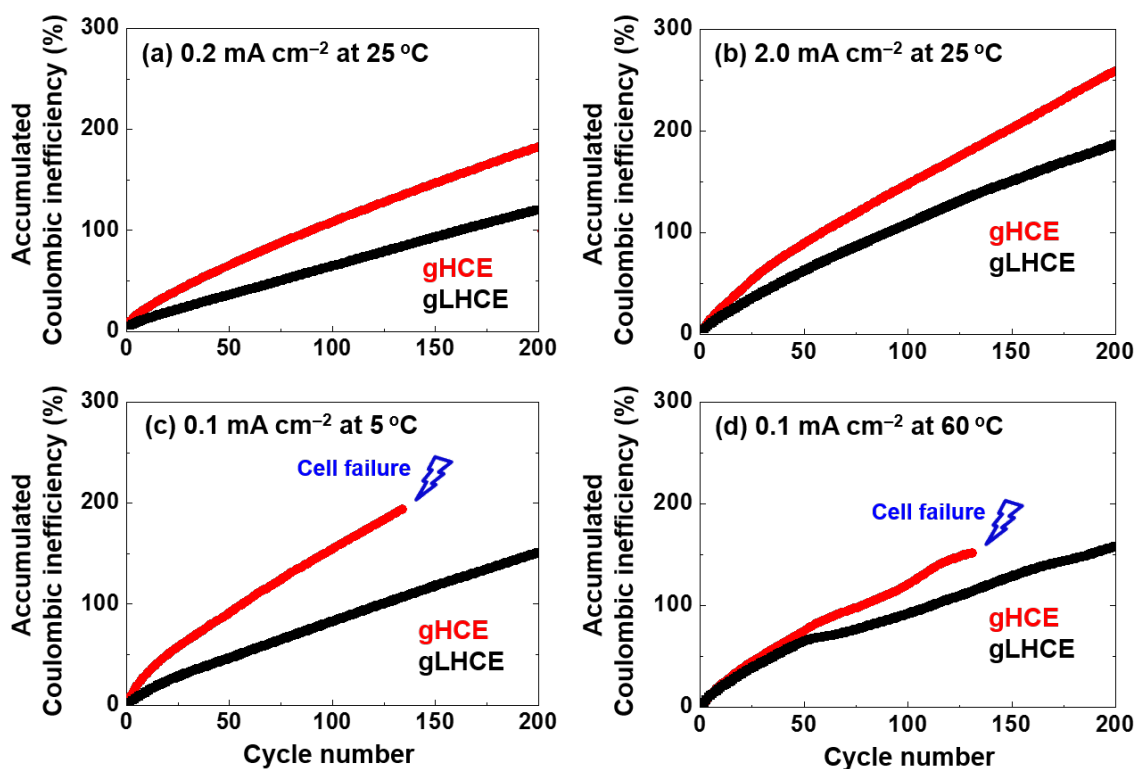


Fig. 4.7 Accumulated Coulombic inefficiency of the Li/Cu cells cycled at 25 °C with a current density of (a) 0.2 mA cm⁻², (b) at 25 °C with 2.0 mA cm⁻², (c) at 5 °C with 0.1 mA cm⁻², and (d) at 60 °C with 0.1 mA cm⁻². Li deposition capacity was 0.5 mAh cm⁻². The cell with gHCE failed during the 135th cycle at 5 °C and during the 132nd cycle at 60 °C.

Along with the high CE, gLHCE presented a low overpotential during the Li cycling (Fig. 4.8). The overpotential difference (the voltage difference at a normalized capacity of 50%) in a cell with gHCE was 68.3 mV at the 1st cycle and 42.0 mV at the 100th cycle; however, that with gLHCE was reduced to 28.8 mV at the 1st cycle and 13.1 mV at the 100th cycle. Consistent with the Li/Cu cell tests, the voltage profiles of the Li/Li cells with gLHCE (Fig. 4.9) showed stable cycling behaviors over 600 h (i.e., 600 cycles) without any sign of internal short-circuiting. A cell with gLHCE presented much lower overpotential (54.8 mV vs. 112.2 mV at the 600th cycle).

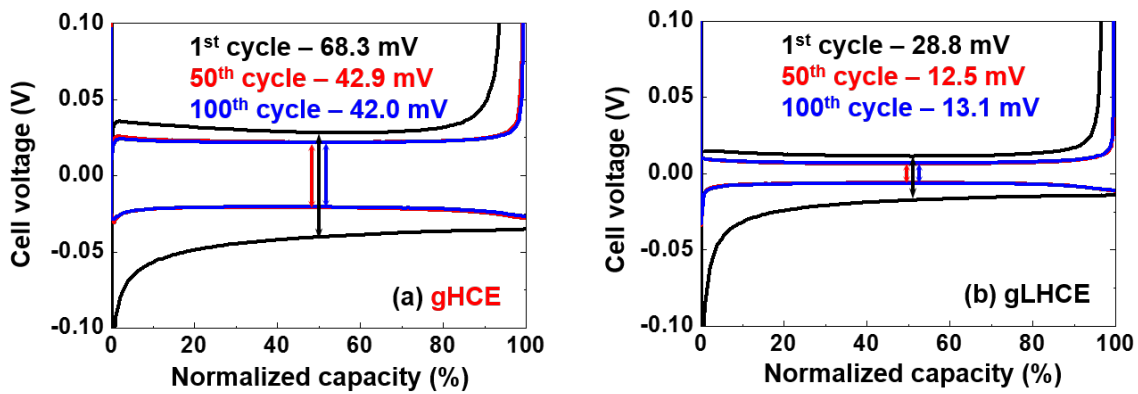


Fig. 4.8 Voltage profiles at the 1st, 50th, and 100th cycle in the Li/Cu cells: (a) gLHCE and (b) gHCE. Overpotential difference was defined as the voltage difference at a normalized capacity of 50%.

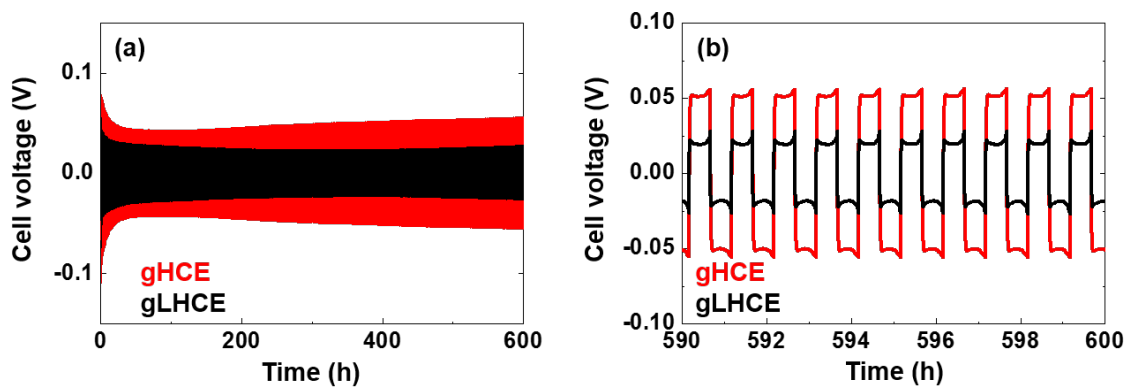


Fig. 4.9 (a) Voltage profiles of the Li/Li cells cycled 600 times in gHCE and gLHCE. Li deposition/dissolution capacity was 0.5 mAh cm^{-2} with a current density of 1.0 mA cm^{-2} (2 C). (b) Enlarged region of the voltage profiles for the last 10 cycles.

Importantly, the outstanding Li cycling behavior in gLHCE was preserved at both 5 °C and 60 °C. As seen in Fig. 4.6c, the cell with gLHCE enabled a higher average CE than that with gHCE at 5 °C (99.22% vs. 98.49%). Moreover, the cell with gHCE displayed marked fluctuation in the CE value and failed abruptly during the 135th cycle, possibly due to internal short-circuiting owing to Li dendrite formation. At the 60 °C test (Fig. 4.6d), gLHCE still exhibited better Li cycling performance than gHCE did, higher average CE (99.16% vs. 98.75%), and no drastic fading during 200 cycles. Once more, the outstanding Li cycling behavior in gLHCE at 5 °C and 60 °C was reflected in the relatively low accumulated Coulombic inefficiency (Figs. 4.7c and 4.7d, respectively).

4.3.5 Surface and ionic species analysis

The surface morphologies of the Li electrodes cycled with gHCE and gLHCE were compared using HR FE-SEM. A spherical morphology was observed in the Li electrode cycled in gHCE (Fig. 4.10a), which was consistent with the literature [2]. Similarly, the electrode cycled in gLHCE exhibited round-shape Li deposits with no dendrite formation (Fig. 4.10b).

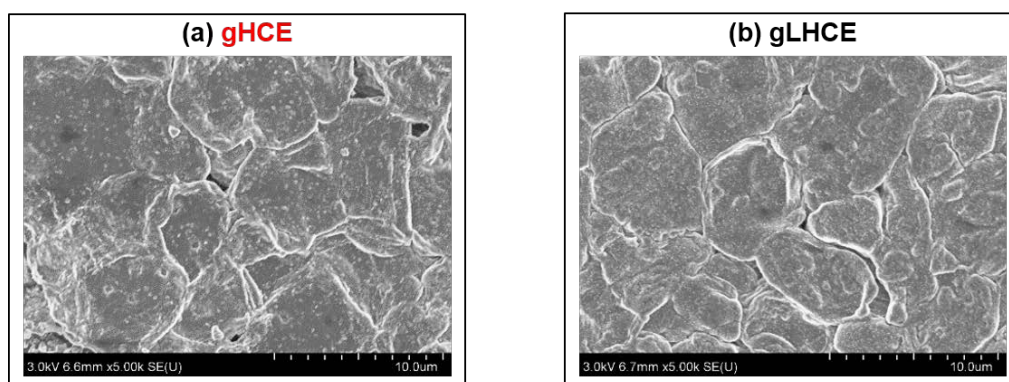


Fig. 4.10 SEM images of the Li electrodes collected from Li/Cu cells cycled 30 times in (a) gHCE and (b) gLHCE. The Li deposition capacity was 1.0 mAh cm⁻² with a current density of 0.5 mA cm⁻².

Since the similar morphologies of Li after cycled with both electrolytes did not give a clear interpretation of great performance of gLHCE compared to gHCE, the outstanding Li cycling behavior enabled by gLHCE

was assumed to be owing to the different nature of the SEI layers in the XPS measurements (Fig. 4.11 and Table 4.2). In both of the SEI layers induced in gHCE and gLHCE, distinct peaks of C–C in C_{1s} , LiF, S-F/C-F in F_{1s} , and salt-derivatives in S_{2p} spectra [26–30] were observed, suggesting that both the DME solvent and FSI-anion participate in the SEI formation (Figs. 4.11a–c).

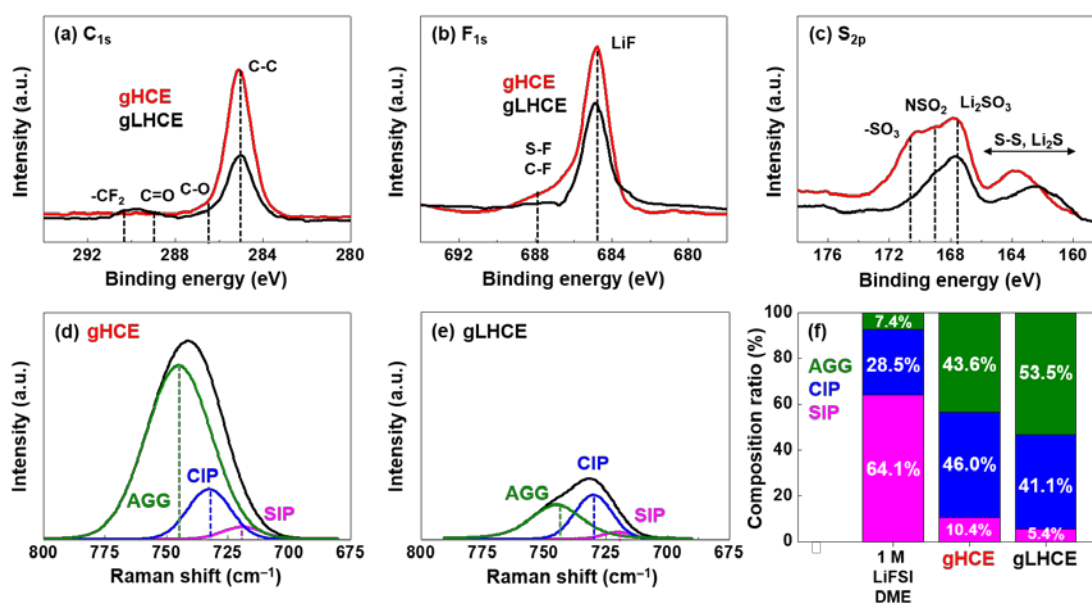


Fig. 4.11 (a) C_{1s} , (b) F_{1s} , and (c) S_{2p} XPS spectra of the Li electrodes collected from the Li/Cu cells cycled 30 times in gHCE and gLHCE. The Li deposition capacity was 1.0 mAh cm^{-2} with a current density of 0.5 mA cm^{-2} . Raman spectra of (d) gHCE and (e) gLHCE. (f) Fractional composition of the ionic species. The ionic speciation of 1 M LiFSI DME is also presented for comparison.

Table 4.2 Atomic composition, determined from XPS spectra, of the Li electrodes collected from the Li/Cu cells cycled 30 times in gHCE and gLHCE.

Species Position	C_{1s}				F_{1s}			S_{2p}			N_{1s}	
	C-C	C-O	C=O	-CF ₂	LiF	S-F/C-F	-SO ₃	NSO ₂	Li ₂ SO ₃	Li ₂ S/S-S	Li ₂ N ₂ O ₂	Li ₃ N
eV	285	287	288.7	290.5	685	688	170.6	169	167.3	Under 166	400	399
gHCE	52.1	2.3	0	0	20.3	5.5	4.2	3.4	3.3	3.6	2.4	2.8
gLHCE	36.7	2.3	4.1	5.7	24.7	4.7	4.8	1.6	5.3	6.3	1.5	2.2

Arguably, however, the SEI induced in the gLHCE contained lower fraction of C-C species (36.7% vs. 52.1%), but higher fraction of LiF and S-F/C-F in the F_{1s} spectra (29.4% vs. 25.8%), and FSI-anion related species in the S_{2p} spectra (18% vs. 14.6%), compared to those in gHCE. This indicates that the contribution of the Li salt becomes significant in gLHCE, leading to an inorganic-rich SEI formation [13, 16]. Accordingly, the excellent Li cycling performance observed in gLHCE is probably due to the inorganic-rich SEI derived in the electrolyte. In particular, the high fraction of LiF in the SEI layer appears to play a key role in the stability of Li over the wide temperature range. Arguably, it was confirmed that a high LiF content is beneficial in the operation of the graphite and silicon anodes of LIBs both at low and elevated temperatures [31–36].

In turn, the inorganic-rich SEI derived in gLHCE appears to be associated with its unique solution structure. To confirm this, the ionic speciation of gHCE and gLHCE was investigated by Raman spectroscopy (Figs. 4.11d and 4.11e). Three Raman peaks located at 720, 735, and 745 cm^{-1} were assigned to the FSI-anions in the forms of solvent-shared ion pair (SIP), contact ion pair (CIP), and agglomerate (AGG), respectively [37, 38]. The fractional compositions of the ionic species are compared in Fig. 4.11f. The ionic speciation of 1 M LiFSI DME is also presented for comparison. Notably, SIP (64.1%) was the dominant species, and CIP (28.5%) and AGG (7.4%) appeared as minor ones in 1 M LiFSI DME. In contrast, gHCE contained higher portions of CIP (46.0%) and AGG (43.6%) rather than SIP (10.4%), indicating the extensive participation of FSI-anions in the Li-ion solvation. The unique solvation structure in HCEs was revealed to cause a shift of the lowest unoccupied molecular orbital (LUMO) toward the FSI-anions, thus increasing the propensity of the anion reduction during the SEI formation [16, 37]. Arguably, in gLHCE, most FSI-anions exist as AGG (53.5%), while the fractions of CIP and SIP were further decreased (41.4% and 5.4%, respectively). This suggests that the presence of TTE leads to more extensive participation of FSI-anions in the Li-ion solvation, which will promote the participation of FSI-anions in the SEI formation in gLHCE. Based on the results of the XPS and Raman measurements, a possible scheme of the SEI formation in gHCE and gLHCE is presented in Fig. 4.12.

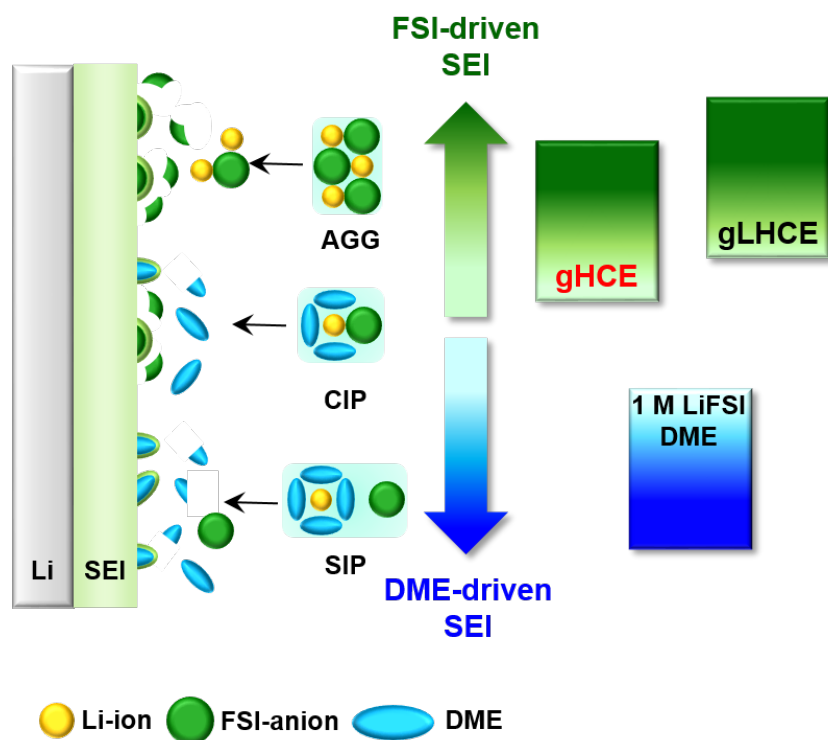


Fig. 4.12 Possible scheme of the participation of ionic species in the SEI formation. The presence of TTE in gLHCE increases the population of CIP and AGG, resulting in more FSI-driven SEI formation.

4.3.6 FeS₂/Li and anode free LFP cell performances

Subsequently, we determined if LMBs could benefit from the Li cycling performance improved by gLHCE. Fig. 4.13a summarizes the discharge capacities at the 4th and 100th cycles of FeS₂/Li cells using gHCE and gLHCE during the cycling at 5 °C, 25 °C, and 60 °C (see Fig. 4.14 for a detailed comparison of the cyclability and voltage profiles). The 4th cycle was selected because all the cycling tests were performed after three formation cycles at 25 °C. During the 25 °C cycling, an FeS₂/Li cell with gLHCE presented higher initial capacity and better retention than the cell with gHCE: 574 vs. 535 mAh g⁻¹ at the 4th cycle, and 253 vs. 194 mAh g⁻¹ at the 100th cycle. Importantly, the merit of gLHCE appeared more clearly at 5 °C and 60 °C tests; a cell with gLHCE retained significantly high capacities after the 100th cycle (218 vs. 122 mAh g⁻¹ at 5 °C, and 292 vs. 190 mAh g⁻¹ at 60 °C). A closer look at the voltage profiles of the FeS₂/Li cells reveals that the increase in the overpotential with the cycling is far less in the cell with gLHCE than in that with gHCE (Fig. 4.14).

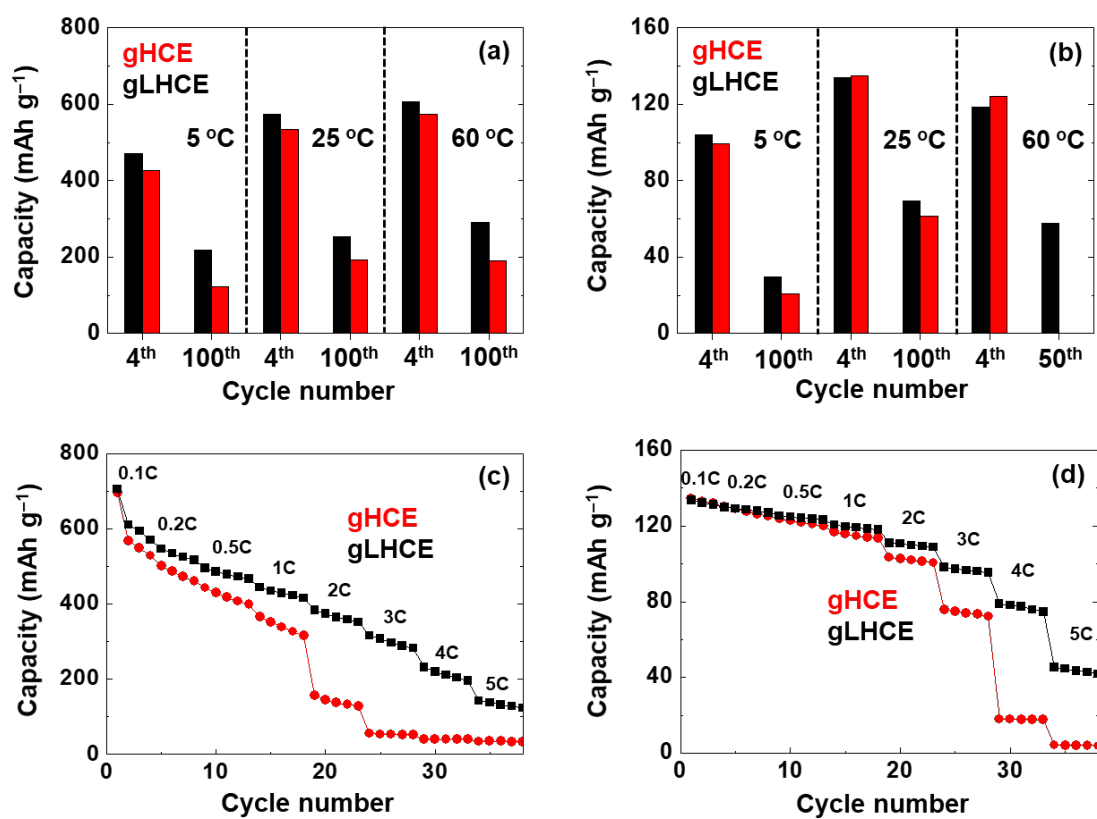


Fig. 4.13 Discharge capacities at the 4th and 100th cycle of the (a) FeS₂/Li and (b) LFP/Cu cells with gHCE and gLHCE at 5 °C, 25 °C, and 60 °C cycling. Discharge capacities of the (c) FeS₂/Li and (d) LFP/Cu cells with gHCE and gLHCE at discharge rates in the range of 0.1–5 C at 25 °C.

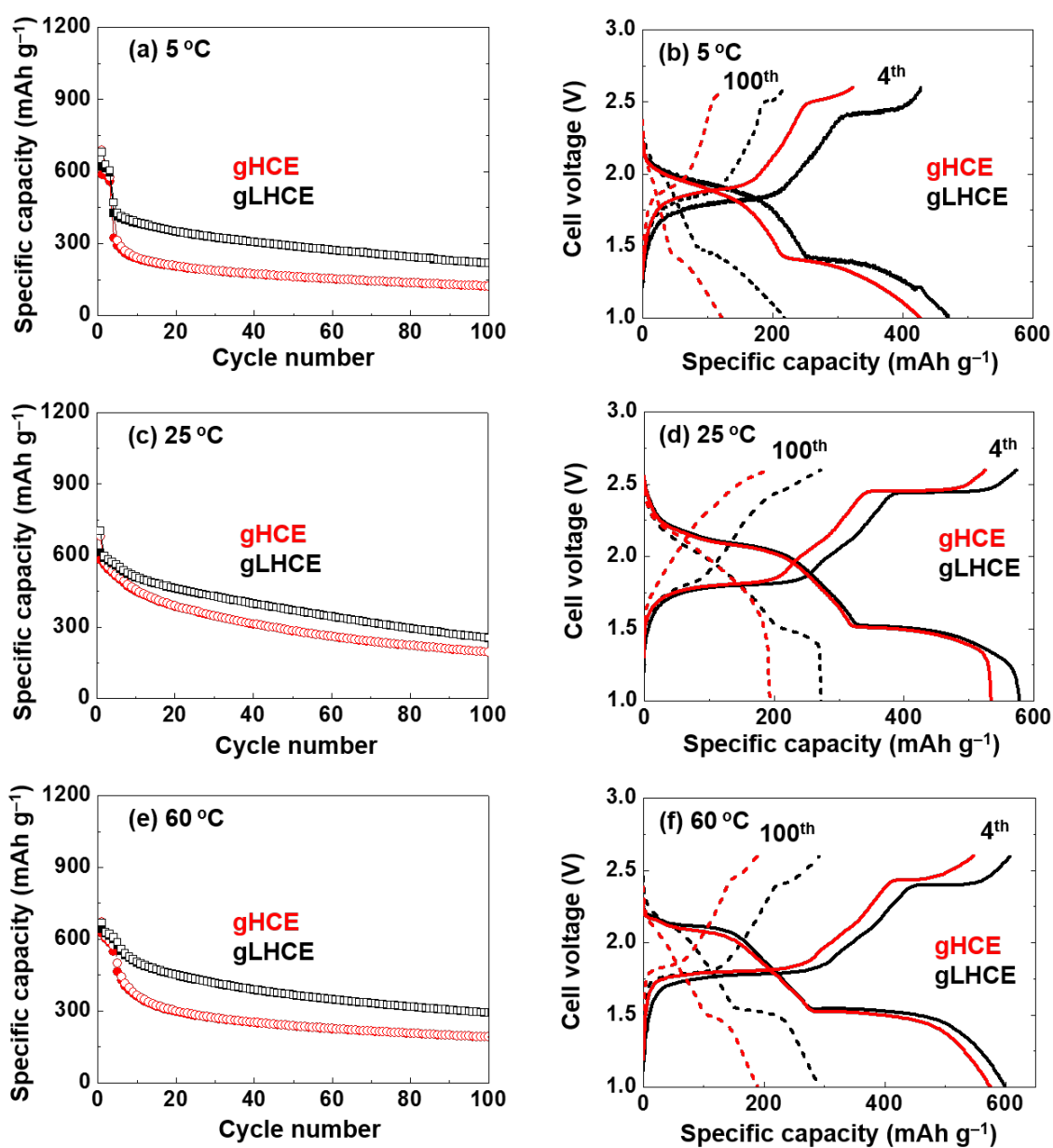


Fig. 4.14 Specific capacity of FeS₂/Li cells with gHCE and gLHCE at (a) 5 °C, (c) 25 °C, and (e) 60 °C. Voltage profiles at 4th and 100th cycle for the FeS₂/Li cells with gHCE and gLHCE at (b) 5 °C, (d) 25 °C, and (f) 60 °C. Cycling at 25 °C was performed at a 0.2 C constant current between 1.0 and 2.6 V. Cycling at 5 °C and 60 °C was performed at a 0.5 C constant current between 1.0 and 2.6 V after the cells were cycled three times at 25 °C with a 0.2 C constant current.

Recently, the anode-free cell with zero-excess Li was suggested as a rapid and effective platform to evaluate the Li CE in a full cell condition [39, 40]. Therefore, we evaluated the cycle performance of anode-free LFP/Cu cells at 5 °C, 25 °C, and 60 °C (Fig. 4.13b, see Fig. 4.15 for a detailed comparison of the cyclability and voltage profiles). Analogous to the results of the FeS₂/Li cells, the LFP/Cu cell with gLHCE exhibited superior cyclability to that of the cell with gHCE at 25 °C, and the advantage of gLHCE was more apparent in the 5 °C and 60 °C tests. In particular, during the 60 °C test, the cell with gLHCE presented decent cycle retention up to the 50th cycle, whereas that with gHCE suffered from severe side reactions from the 20th cycle and failed before the 40th cycle (Fig. 4.15e).

Besides the excellent cycle performance over a wide temperature range, 5–60 °C, gLHCE enabled fast operation of the LMBs as well. Fig. 4.13c presents the discharge behavior at 25 °C of the FeS₂/Li cells at various current densities in the range of 0.1–5 C. While the cell with gLHCE exhibited a similar capacity to that with gHCE at 0.1 C, the former retained a much higher capacity than that of the latter at a relatively high current rate. The cell with gLHCE delivered 384 mAh g⁻¹ at a 2 C rate, whereas the cell with gHCE achieved only 157 mAh g⁻¹. In addition, the outstanding rate capability of gLHCE was preserved in the LFP/Cu cells as well (Fig. 4.13d).

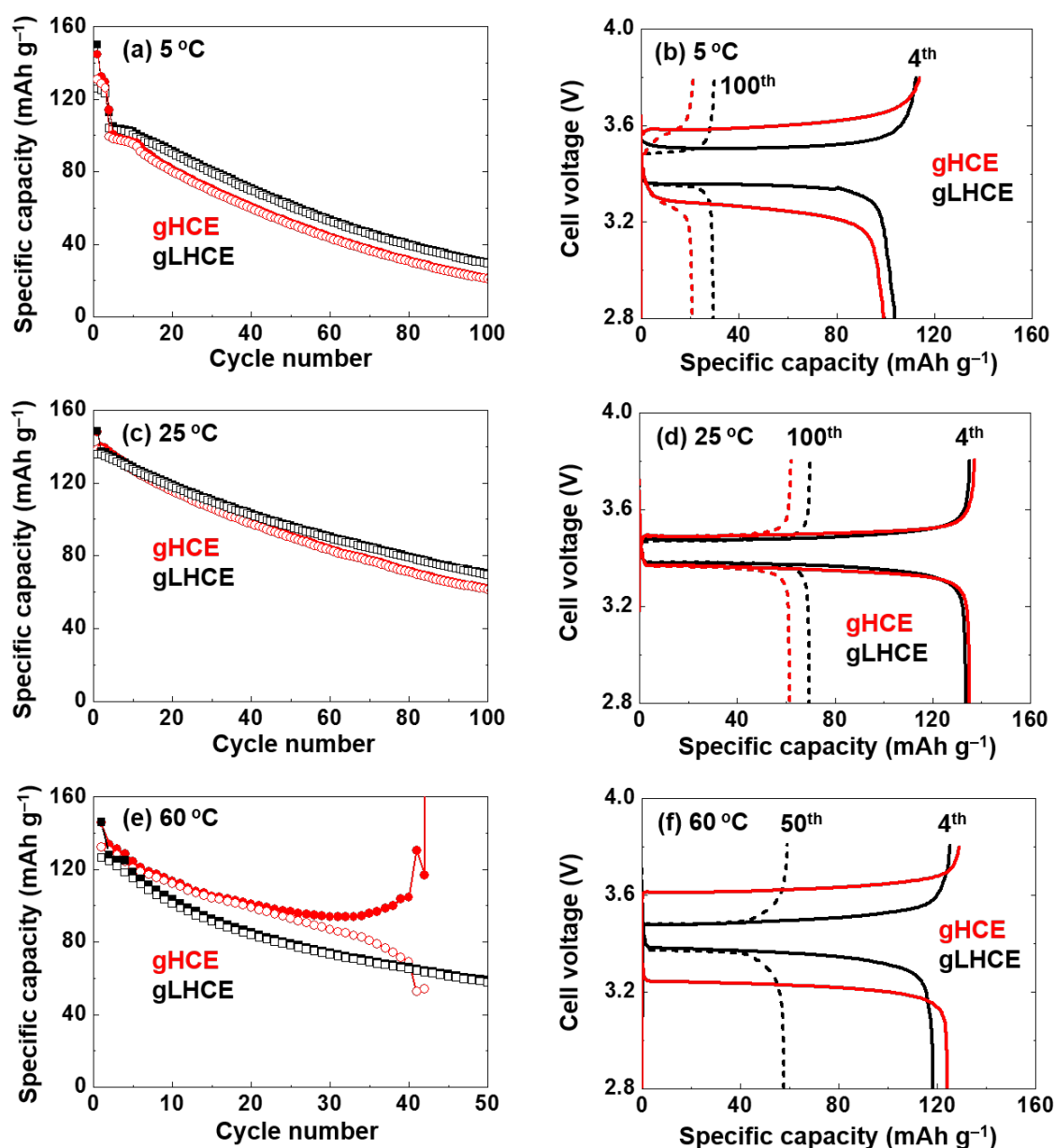


Fig. 4.15 Specific capacity of the LFP/Cu cells with gHCE and gLHCE at (a) 5 °C, (c) 25 °C, and (e) 60 °C. Voltage profiles at the 4th and 100th (50th) cycles for the LFP/Cu cells with gHCE and gLHCE at (b) 5 °C, (d) 25 °C, and (f) 60 °C. Cycling at 25 °C was performed at a 0.2 C constant current between 2.8 and 3.8 V. Cycling at 5 °C and 60 °C was performed at a 0.5 C constant current between 2.8 and 3.8 V after the cells were cycled three times at 25 °C with a 0.2 C constant current.

4.3.7 Internal resistance analysis

To better understand the interfacial kinetics of the Li electrodes, EIS measurements were conducted. Figs. 4.16a and 4.16b present the Nyquist plots of the Li/Li cells with gHCE and gLHCE measured over 5–55 °C. The fitted resistance values derived from the impedance spectra with an equivalent circuit (Fig. 4.16c) are presented in Table 4.3, where R_s , R_{SEI} , and R_{ct} are the ohmic resistance, SEI resistance, and interfacial charge transfer resistance, respectively [41, 42]. R_s is expected to be inversely proportional to the ionic conductivity of the electrolytes. Indeed, the R_s values of gHCE and gLHCE are inversely proportional to their ionic conductivities, as shown in Fig. 4.1a; the R_s (ionic conductivity) of gLHCE was smaller (higher) than that of gHCE from 5 °C to 25 °C, and increased (lower) over 35 °C. Importantly, the R_{SEI} and R_{ct} values of gLHCE were notably smaller than those of gHCE over the whole temperature range. Notably, over 35–55 °C, the lower R_{SEI} and R_{ct} of gLHCE overcompensates its slightly higher R_s . Therefore, the low internal resistance of Li anode in gLHCE, together with its excellent wettability account for the outstanding rate capability of the FeS₂/Li and LFP/Cu cells. With this respect, the lower overpotential of Li/Cu, Li/Li, FeS₂/Li, and LFP/Cu cells with gLHCE (Fig. 4.8, 4.9, 4.14, and 4.15, respectively) can be understood. The low internal resistance in LHCE compared to that in HCE was also reported in the previous studies [14, 18], of which origin deserves further study. As a tentative conclusion, we suppose that the lower R_{SEI} in gLHCE is associated with the inorganic-rich SEI layer derived in the electrolyte [33–35]. It appears that the low R_{ct} in gLHCE stems from the unique solvation structure of gLHCE.

Reportedly, the desolvation process of Li-ions at the electrode/electrolyte interface was identified as a decisive contributor to this type of resistance, demonstrating the important role of ion-solvent interactions in the interfacial kinetics [43, 44]. Indeed, as deduced from the Arrhenius plots (Fig. 4.16d), the activation energy of the charge transfer reaction (E_a^{ct}) of the Li/Li cell with gLHCE was found to be lower than that with gHCE (30.6 kJ mol⁻¹ vs. 36.5 kJ mol⁻¹). This reflects that gLHCE mitigates the activation barrier for Li-transfer at the interface, which should be associated with the favorable solvation structure of gLHCE.

Table 4.3 Fitted resistance values from Nyquist plots of the Li/Li cells measured at a SOC 50 shown in Fig. 4.16.

Temperature (°C)	Li/Li cell with gHCE			Li/Li cell with gLHCE		
	R_s (Ω)	R_{SEI} (Ω)	R_{ct} (Ω)	R_s (Ω)	R_{SEI} (Ω)	R_{ct} (Ω)
5	1.64	3.87	34.78	1.45	3.52	19.83
15	1.48	3.84	25.68	1.35	3.25	16.82
25	1.27	3.11	15.57	1.19	2.13	9.18
35	0.97	2.67	10.09	1.14	1.68	6.58
45	0.75	1.90	5.91	1.00	1.31	4.62
55	0.60	1.11	3.09	0.83	0.66	2.71

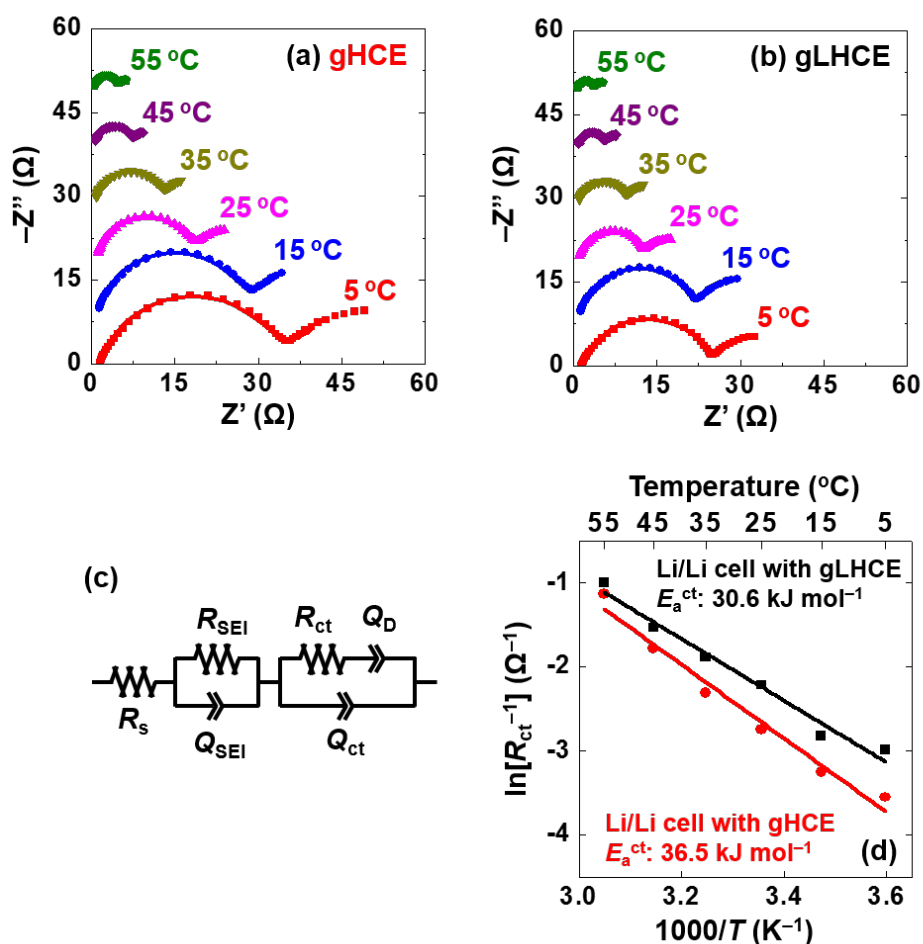


Fig. 4.16 Nyquist plots of the Li/Li cells with (a) gHCE and (b) gLHCE over 5–55 °C measured at a state-of-charge (SOC) 50. The Li/Li cells were cycled 3 times before the impedance measurements. (c) An equivalent circuit for fitting of impedance data. (d) Arrhenius plots of the charge transfer resistance (R_{ct}) for Li/Li cells with gHCE and gLHCE. Li deposition/dissolution capacity for the formation process was 1.0 mAh cm^{-2} at a current density of 0.2 mA cm^{-2} . The experimental spectra were plotted as solid dots and the best-fitted data were solid lines. The parameters, R_s , R_{SEI} , R_{ct} , Q_{SEI} , Q_{ct} , and Q_D were determined by the curve fitting with the equivalent circuit (Fig. 4.16c). Q_{SEI} and Q_{ct} are the constant phase elements (CPEs) coupled with R_{SEI} and R_{ct} , respectively. Q_D represents the finite diffusion of a Warburg element ^[45, 46].

4.3.8 Comparison

Finally, we compared gLHCE with various LHCEs reported thus far in the literature (Table 4.4). Arguably, gLHCE is comparable to or better than the other LHCEs in terms of the Li CE, ionic conductivity, viscosity, non-flammability, and electrochemical stability. Moreover, this study suggests that gLHCE markedly improves the cycle performance of LMBs over a wide temperature range.

Table 4.4 Comparison of the Li cycle test, ionic conductivity, viscosity, non-flammability, and electrochemical stability of various LHCEs and HCEs. The values of HCEs are denoted in parenthesis.

LHCE (HCE)	Li CE, cycles, current density, areal capacity	Ionic conductivity (mS cm ⁻¹)	Viscosity (cP)	Non-flammability	Oxidation potential (V) /Al corrosion	Cell Types
LiFSI/3TMS/3TTE (LiFSI/3TMS) ^[13]	98.8 % (98.2 %), 150 cycles, 0.5 mA cm ⁻² , 1 mAh cm ⁻²	ca. 3 (ca. 2)	14.1 (99.5)	O (O)	NA /X (O)	LNMO/Li
1.2 M LiFSI DMC/BTFE (1/2 by mol) (5.5 M LiFSI DMC) ^[14]	99.3 % (99.2 %), 200 cycles, 0.5 mA cm ⁻² , 5 mAh cm ⁻²	2.67 (1)	2.7 (180)	X (X)	NA /X (X)	NMC/Li
1.2 M LiFSI TEP/BTFE (1/3 by mol) (3.2 M LiFSI TEP) ^[15]	99.2 % (97.3 %), 10 cycles, 0.5 mA cm ⁻² , 1 mAh cm ⁻² after formation with 5 mAh cm ⁻²	1.29 (0.52)	2.9 (150)	O (O)	NA /X (X)	NMC/Li
LiFSI/1.2DME/3TTE (LiFSI/1.2 DME) ^[16]	99.3 % (99.2 %), 300 (200) cycles, 0.5 mA cm ⁻² , 1 mAh cm ⁻²	2.44 (4.18)	4.8 (48)	O (X)	4.5 (4.5) /NA	NMC/Li NMC/Cu
LiFSI/DME (1/1 by mol) + 50 wt% HFME (LiFSI/DME (1/1 by mol)) ^[17]	99.46 % (99.22 %), 500 cycles, 1 mA cm ⁻² , 1 mAh cm ⁻²	3.18 (1.74)	ca. 10 (82.6)	O (X)	4.8 (4.7) /NA	Sulfur/Li
1 M LiFSI DME/TTE (1/2 by vol) (4 M LiFSI DME)	99.4 % (99.09%), 200 cycles, 0.2 mA cm ⁻² , 0.5 mAh cm ⁻²	6.9 (5.7)	4.9 (36.2)	O (X)	4.86 (4.85) /X (O)	FeS ₂ /Li LFP/Cu

4.4 Conclusions

This study demonstrates the significant advantages of gLHCE over gHCE in the operation of LMBs under harsh temperature conditions. The TTE co-solvent exhibiting favorable properties, including non-solvating ability toward Li-ions, low viscosity, and non-flammability, played a crucial role in fulfilling the key requirements of LMB electrolytes: stable and reversible Li cycling, fast ion transport, facile wetting toward polyethylene separators, and thermal stability. In addition, among various combinations of glymes and fluorinated ethers, a pair of DME and TTE (1/2, v/v), i.e., gLHCE, was revealed to present the best Li cycling performance. Importantly, gLHCE exhibited Li CEs higher than those of gHCE, not only under ambient condition (25 °C) but also at low (5 °C) and elevated (60 °C) temperatures. XPS and Raman measurements evidenced that the excellent Li cycling performance in gLHCE is attributed to the dominance of associative solution species (AGG and CIP), which facilitate the formation of inorganic-rich SEI on the Li anode. The excellent compatibility with the Li anode together with the outstanding physicochemical properties of gLHCE led to the markedly improved long-term cyclability of the FeS₂/Li and anode-free LFP/Cu cells over the wide temperature range. In addition, gLHCE displayed the facile kinetics at the Li/electrolyte interface, which together with the high ionic conductivity and good wettability, resulted in the enhanced rate capabilities of the FeS₂/Li and LFP/Cu cells compared to the case with gHCE. Our findings indicate that LHCEs can expand the operating temperature range of LMBs, thus propelling LMBs one-step closer to the standard of the state-of-the-art Li-ion batteries.

4.5 References

- [1] S.-K. Jeong, H.-Y. Seo, D.-H. Kim, H.-K. Han, J.-G. Kim, Y. B. Lee, Y. Iriyama, T. Abe, Z. Ogumi, Suppression of dendritic lithium formation by using concentrated electrolyte solutions, *Electrochem. Commun.* 10 (2008) 635–638.
- [2] J. Qian, W. A. Henderson, W. Xu, P. Bhattacharya, M. Engelhard, O. Borodin, J.-G. Zhang, High rate and stable cycling of lithium metal anode, *Nat. Commun.* 6 (2015) 6362.
- [3] Q. Ma, Z. Fang, P. Liu, J. Ma, X. Qi, W. Feng, J. Nie, Y.-S. Hu, H. Li, X. Huang, L. Chen, Z. Zhou, Improved cycling stability of lithium-metal anode with concentrated electrolytes based on lithium (fluorosulfonyl)(trifluoromethanesulfonyl)imide, *ChemElectroChem* 3 (2016) 531–536.
- [4] Z. Fang, Q. Ma, P. Liu, J. Ma, Y.-S. Hu, Z. Zhou, H. Li, X. Huang, L. Chen, Novel concentrated Li[(FSO₂)(n-C₄F₉SO₂)N]-based ether electrolyte for superior stability of metallic lithium anode, *ACS Appl. Mater. Interfaces* 9 (2017) 4282–4289.
- [5] Z. Zeng, V. Murugesan, K. S. Han, X. Jiang, Y. Cao, L. Xiao, X. Ai, H. Yang, J.-G. Zhang, M. L. Sushko, J. Liu, Non-flammable electrolytes with high salt-to-solvent ratios for Li-ion and Li-metal batteries, *Nat. Energy* 3 (2018) 674–681.
- [6] P. Zhang, J. Zhu, M. Wang, N. Imanishi, O. Yamamoto, Lithium dendrite suppression and cycling efficiency of lithium anode, *Electrochem. Commun.* 87 (2018) 27–30.
- [7] S. Jiao, X. Ren, R. Cao, M. H. Engelhard, Y. Liu, D. Hu, D. Mei, J. Zheng, W. Zhao, Q. Li, N. Liu, B. D. Adams, C. Ma, J. Liu, J.-G. Zhang, W. Xu, Stable cycling of high-voltage lithium metal batteries in ether electrolytes, *Nat. Energy* 3 (2018) 739–746.
- [8] X. Fan, L. Chen, X. Ji, T. Deng, S. Hou, J. Chen, J. Zheng, F. Wang, J. Jiang, K. Xu, C. Wang, Highly fluorinated interphases enable high-voltage Li-metal batteries, *Chem.* 4 (2018) 174–185.
- [9] L. Suo, W. Xue, M. Gobet, S. G. Greenbaum, C. Wang, Y. Chen, W. Yang, Y. Li, J. Li, Fluorine-donating electrolytes enable highly reversible 5-V-class Li metal batteries, *Proc. Natl. Acad. Sci. U.S.A.* 115(6) (2018) 1156–1161.
- [10] J. Zhou, Y. Guo, C. Liang, L. Cao, H. Pan, J. Yang, J. Wang, A new ether-based electrolyte for lithium

sulfur batteries using a S@PAN cathode, *Chem. Commun.* 54 (2018) 5478–5481.

[11] B. Liu, W. Xu, P. Yan, X. Sun, M. E. Bowden, J. Read, J. Qian, D. Mei, C.-M. Wang, J.-G. Zhang, Enhanced cycling stability of rechargeable Li-O₂ batteries using high-concentration electrolytes, *Adv. Funct. Mater.* 26 (2016) 605–613.

[12] L. Suo, Y.-S. Hu, H. Li, M. Armand, L. Chen, A new class of solvent-in-salt electrolyte for high-energy rechargeable metallic lithium batteries, *Nat. Commun.* 4 (2013) 1481.

[13] X. Ren, S. Chen, H. Lee, D. Mei, M. H. Engelhard, S. D. Burton, W. Zhao, J. Zheng, Q. Li, M. S. Ding, M. Schroeder, J. Alvarado, K. Xu, Y. S. Meng, J. Liu, J.-G. Zhang, W. Xu, Localized high-concentration sulfone electrolytes for high-efficiency lithium-metal batteries, *Chem* 4(8) (2018) 1877–1892.

[14] S. Chen, J. Zheng, D. Mei, K. S. Han, M. H. Engelhard, W. Zhao, W. Xu, J. Liu, J.-G. Zhang, High-voltage lithium-metal batteries enabled by localized high-concentration electrolytes, *Adv. Mater.* 30(21) (2018) 1706102.

[15] S. Chen, J. Zheng, L. Yu, X. Ren, M. H. Engelhard, C. Niu, H. Lee, W. Xu, J. Xiao, J. Liu, J.-G. Zhang, High-efficiency lithium metal batteries with fire-retardant electrolytes, *Joule* 2(8) (2018) 1548–1558.

[16] X. Ren, L. Zou, X. Cao, M. H. Engelhard, W. Liu, S. D. Burton, H. Lee, C. Niu, B. E. Matthews, Z. Zhu, C. Wang, B. W. Arey, J. Xiao, J. Liu, J.-G. Zhang, W. Xu, Enabling high-voltage lithium-metal batteries under practical conditions, *Joule* 3(7) (2019) 1662–1676.

[17] F. Huang, G. Ma, Z. Wen, J. Jin, S. Xu, J. Zhang, Enhancing metallic lithium battery performance by tuning the electrolyte solution structure, *J. Mater. Chem. A* 6 (2018) 1612–1620.

[18] J. Zheng, S. Chen, W. Zhao, J. Song, M. H. Engelhard, J.-G. Zhang, Extremely stable sodium metal batteries enabled by localized high-concentration electrolytes, *ACS Energy Lett.* 3(2) (2018) 315–321.

[19] L. Yu, S. Chen, H. Lee, L. Zhang, M. H. Engelhard, Q. Li, S. Jiao, J. Liu, W. Xu, J.-G. Zhang, A localized high-concentration electrolyte with optimized solvents and lithium difluoro(oxalate)borate additive for stable lithium metal batteries, *ACS Energy Lett.* 3(9) (2018) 2059–2067.

[20] M.-S. Wu, T.-L. Liao, Y.-Y. Wang, C.-C. Wan, Assessment of the wettability of porous electrodes for lithium-ion batteries, *J. Appl. Electrochem.* 34 (2004) 797–805.

[21] J. Zhang, D. Y. Kwok, Calculation of solid-liquid work of adhesion patterns from combining rules for

intermolecular potentials, *J. Phys. Chem. B* 106 (2002) 12594–12599.

[22] J. Wang, Y. Yamada, K. Sodeyama, C. H. Chiang, Y. Tateyama, A. Yamada, Superconcentrated electrolytes for a high-voltage lithium-ion battery, *Nat. Commun.* 7 (2016) 12032.

[23] C.-C. Su, M. He, R. Amine, K. Amine, A selection rule for hydrofluoroether electrolyte cosolvent: Establishing a linear free-energy relationship in lithium-sulfur batteries, *Angew. Chem. Int. Ed.* 58 (2019) 10591–10595.

[24] J. O. Besenhard, M. W. Wagner, M. Winter, Inorganic film-forming electrolyte additives improving the cycling behaviour of metallic lithium electrodes and the self-discharge of carbon-lithium electrodes, *J. Power Sources* 43–44 (1993) 413–420.

[25] S. Krueger, R. Kloepsch, J. Li, S. Nowak, S. Passerini, M. Winter, How do reactions at the anode/electrolyte interface determine the cathode performance in lithium-ion batteries?, *J. Electrochem. Soc.* 160(4) (2013) A542–A548.

[26] V. Nilsson, R. Younesi, D. Brandell, K. Edström, P. Johansson, Critical evaluation of the stability of highly concentrated LiTFSI - Acetonitrile electrolytes vs. graphite, lithium metal and LiFePO₄ electrodes, *J. Power Sources* 384 (2018) 334–341.

[27] M. Wang, L. Huai, G. Hu, S. Yang, F. Ren, S. Wang, Z. Zhang, Z. Chen, C. Shen, D. Wang, Effect of LiFSI concentrations to form thickness- and modulus-controlled SEI layers on lithium metal anodes, *J. Phys. Chem. C* 122 (2018) 9825–9834.

[28] R. Younesi, F. Bardé, Electrochemical performance and interfacial properties of Li-metal in lithium bis(fluorosulfonyl)imide based electrolytes, *Sci. Rep.* 7 (2017) 15925.

[29] H. Kim, F. Wu, J. T. Lee, N. Nitta, H.-T. Lin, M. Oschatz, W. I. Cho, S. Kaskel, O. Borodin, G. Yushin, In situ formation of protective coatings on sulfur cathodes in lithium batteries with LiFSI-based organic electrolytes, *Adv. Energy Mater.* 5 (2015) 1401792.

[30] J. Alvarado, M. A. Schroeder, T. P. Pollard, X. Wang, J. Z. Lee, M. Zhang, T. Wynn, M. Ding, O. Borodin, Y. S. Meng, K. Xu, Bisalt ether electrolytes: a pathway towards lithium metal batteries with Ni-rich cathodes, *Energy Environ. Sci.* 12 (2019) 780–794.

[31] X. Sun, H. S. Lee, X. Q. Yang, J. McBreen, Improved elevated temperature cycling of LiMn₂O₄ spi-

nel through the use of a composite LiF-based electrolyte, *Electrochem. Solid-state Lett.* 4 (2001) A184–A186.

[32] I. A. Profatilova, S.-S. Kim, N.-S. Choi, Enhanced thermal properties of the solid electrolyte interphase formed on graphite in an electrolyte with fluoroethylene carbonate, *Electrochim. Acta* 54 (2009) 4445–4450.

[33] B. Liu, B. Li, S. Guan, Effect of fluoroethylene carbonate additive on low temperature performance of Li-ion batteries, *Electrochem. Solid-state Lett.* 15(6) (2012) A77–A79.

[34] B. Yang, H. Zhang, L. Yu, W. Z. Fan, D. Huang, Lithium difluorophosphate as an additive to improve the low temperature performance of $\text{LiNi}_{0.5}\text{Co}_{0.2}\text{Mn}_{0.3}\text{O}_2$ /graphite cells, *Electrochim. Acta* 221 (2016) 107–114.

[35] X.-Q. Zhang, X. Chen, X.-B. Cheng, B.-Q. Li, X. Shen, C. Yan, J.-Q. Huang, Q. Zhang, Highly stable lithium metal batteries enabled by regulating the solvation of lithium ions in nonaqueous electrolytes, *Angew. Chem. Int. Ed.* 57 (2018) 5301–5305.

[36] S.-J. Kang, K. Park, S.-H. Park, H. Lee, Unraveling the role of LiFSI electrolyte in the superior performance of graphite anodes for Li-ion batteries, *Electrochim. Acta* 259 (2018) 949–954.

[37] Y. Yamada, K. Furukawa, K. Sodeyama, K. Kikuchi, M. Yaegashi, Y. Tateyama, A. Yamada, Unusual stability of acetonitrile-based superconcentrated electrolytes for fast-charging lithium-ion batteries, *J. Am. Chem. Soc.* 136 (2014) 5039–5046.

[38] S.-D. Han, O. Borodin, D. M. Seo, Z.-B. Zhou, W. A. Henderson, Electrolyte solvation and ionic association V. Acetonitrile-lithium bis(fluorosulfonyl)imide (LiFSI) mixtures, *J. Electrochem. Soc.* 161(14) (2014) A2042–A2053.

[39] J. Qian, B. D. Adams, J. Zheng, W. Xu, W. A. Henderson, J. Wang, M. E. Bowden, S. Xu, J. Hu, J.-G. Zhang, Anode-free rechargeable lithium metal batteries, *Adv. Funct. Mater.* 26 (2016) 7094–7102.

[40] M. Genovese, A. J. Louli, R. Weber, S. Hames, J. R. Dahn, Measuring the Coulombic efficiency of lithium metal cycling in anode-free lithium metal batteries, *J. Electrochem. Soc.* 165(14) (2018) A3321–A3325.

[41] D. Aurbach, K. Gamolsky, B. Markovsky, Y. Gofer, M. Schmidt, U. Heider, On the use of vinylene carbonate (VC) as an additive to electrolyte solutions for Li-ion batteries, *Electrochim. Acta* 47 (2002) 1423–1439.

[42] T. Abe, H. Fukuda, Y. Iriyama, Z. Ogumi, Solvated Li-ion transfer at interface between graphite and

electrolyte, *J. Electrochem. Soc.* 151 (2004) A1120–A1123.

[43] Y. Yamada, Y. Iriyama, T. Abe, Z. Ogumi, Kinetics of lithium ion transfer at the interface between graphite and liquid electrolytes: Effects of solvent and surface film, *Langmuir* 25(21) 2009 12766–12770.

[44] K. Xu, A. von W. Cresce, Li⁺-solvation/desolvation dictates interphasial processes on graphitic anode in Li ion cells, *J. Mater. Res.* 27 (2012) 2327–2341.

[45] C. Zhuang, T. Wei, L. L. Du, Y. L. Cui, L. Fang, S. G. Sun, An electrochemical impedance spectroscopic study of the electronic and ionic transport properties of spinel LiMn₂O₄, *J. Phys. Chem. C* 114 (2010) 8614–8621.

[46] Y. Qiu, Q. C. Zhuang, Q. Q. Zhuang, R. Cao, P. Z. Ying, Y. H. Qiang, S. G. Sun, Electrochemical and electronic properties of LiCoO₂ cathode investigated by galvanostatic cycling and EIS, *Phys. Chem. Chem. Phys.* 14 (2012) 2617–2630.

V. Analysis of rate performance of high-concentration electrolytes and localized high-concentration electrolytes

5.1 Introduction

It has been reported that LiFSI-acetonitrile (AN) HCEs exhibited excellent capacity retention at high charge/discharge rate in graphite cells, contrast to the belief that LiFSI-AN electrolytes undergo severe cycling failure with Li metal anode owing to poor reductive stability^[1].

In the report, reversible cycling behaviors were shown in LiTFSI-AN HCEs unlike AN based diluted electrolytes (DEs) (Fig. 5.1). In HCEs, a stable anion-derived SEI layer could be formed because anions are preferably reduced rather than AN solvents during the Li intercalation process of the graphite in such HCEs^[1]. Also, LiFSI-AN HCEs provided a great capacity retention at fast charging of graphite/Li cells compared to the conventional electrolytes (Fig. 5.2).

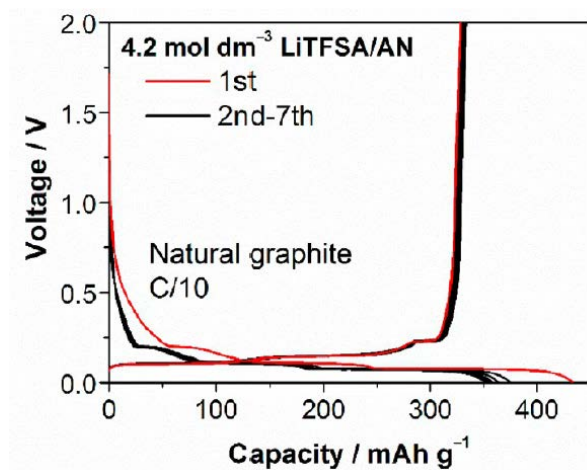


Fig. 5.1 Charge/discharge profiles of graphite/Li cells with 4.2 M LiTFSI-AN solution. The charge/discharge rate is 0.1C^[1].

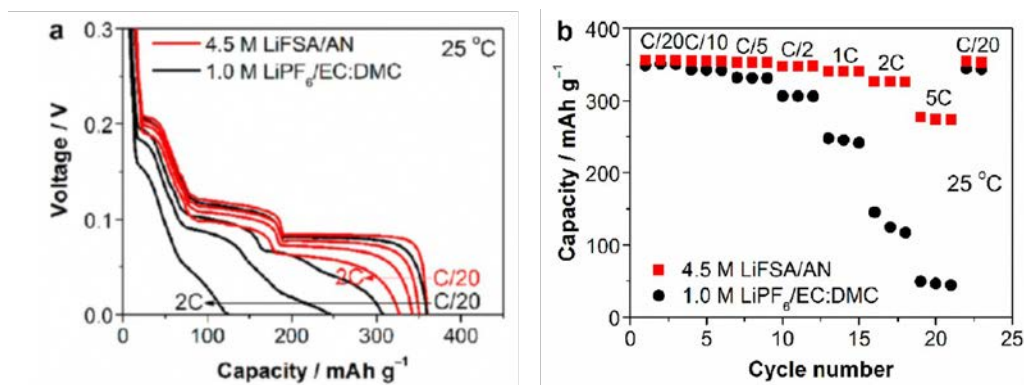


Fig. 5.2 (a) Lithium intercalation voltage profiles of graphite/Li cells at various C-rates from 0.05C to 2C. (b) Lithium deintercalation capacity of graphite/Li cells at various C-rates from 0.05C to 5C. The current density during charge and discharge was set to the same C-rate and the cells were charged/discharged with only constant current mode^[1].

As shown in Table 5.1, the physicochemical properties of LiFSI-AN HCEs (> 4 M) are revealed to be very poor than LiFSI-AN DEs (1 M) and it is also widely known that the conventional electrolytes exhibited much greater ionic conductivity and lower viscosity than such HCEs. Nevertheless, the exact reason for excellent rate capability of HCEs still remains elusive.

Table 5.1 Physicochemical properties of LiFSI-AN electrolytes at 30 °C^[1].

Concentration (mol dm ⁻³)	Density (g cm ⁻³)	Ionic conductivity (mS cm ⁻¹)	Viscosity (cP)
1	0.89	50	0.69
3	1.14	29	4.0
4	1.26	16	9.0
5	1.37	7.1	37.7
6	1.48	3.3	153

To assess the relation between the characteristics of the electrolyte and the rate capability of cells, LiFSI-DMC DE, HCE, and LHCEs are utilized with electrochemical techniques including EIS, electromotive force (EMF) of concentration cells, and galvanostatic intermittent titration technique (GITT).

5.1.1 Overpotential

In electrochemistry, overpotential (η) is the additional voltage for the reactions to occur in experimental conditions. The reactions are driven by applying more potential than thermodynamically determined potential. There are three types of overpotentials during charge/discharge of cells, and they influence the electrochemical performance of cells severely. As shown in Table 5.2 and Fig. 5.3, charge transfer overpotential (η_{ct}) is related to kinetics and presented due to charge transport at the interfaces. It depends on rate constant such as charge transfer activation energy (E_a^{ct}) and exchange current (i_0). Ohmic, ionic, and concentration overpotential are related to mass transport in batteries and presented owing to the ohmic losses in the electrical and ionic conductors, ionic losses in electrode pores, and mass depletion/accumulation, respectively. Influencing parameters on mass transport related overpotential are ionic conductivity, contact resistance, porosity, thickness, transference number, Li salt diffusion and Li salt activity. These overpotentials closely affect the electrochemical performances of the cells as shown in Fig. 5.4. η_{ohm} , η_{ion} , and η_{ct} affect at the early stage of discharge process due to the rapid time-scale of ionic conduction and charge transfer reactions while η_{ct} significantly reduces the electrochemical performance at the late time of discharge process due to the cumulative concentration gradient. It is noted that when cycled slowly the influence of overpotentials is not severe but it becomes much critical during fast cycling. This means for the accomplishment on the fast operation of the batteries the overpotentials should be taken care of precisely. Thus, I investigated the effects of these overpotentials on the rate capability of cells with DE, HCE, and LHCEs.

Table 5.2 Explanation of types of overpotential, adapted from the handouts of the “Electrochemistry” class.

Overpotential type	Due to	Depends on	
Kinetics	η_{ct} :charge transfer, activation	Charge (electron /ions/charged species) transport at the interfaces	Rate constant (E_a^{ct} , i_0)
	η_{ohm} :ohmic	Ohmic losses in the electrical and ionic conductors(=IR drop)	Ionic conductivity, contact resistance
Mass transport	η_{ion} :ionic in pores	Ionic resistance in electrode pores	Ionic conductivity, porosity, thickness
	η_{conc} :concentration	Mass (ions/charged species) depletion/accumulation	Transference number, Li salt diffusion, Li salt activity

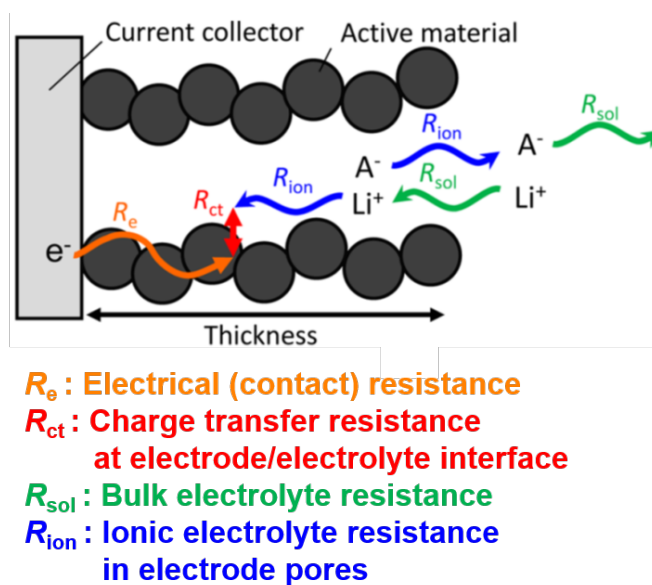


Fig. 5.3 Scheme for the types of resistance caused by the overpotential in the cells with porous electrodes. The ionic resistance in electrode pores (R_{ion}) should be considered in the porous electrodes^[2].

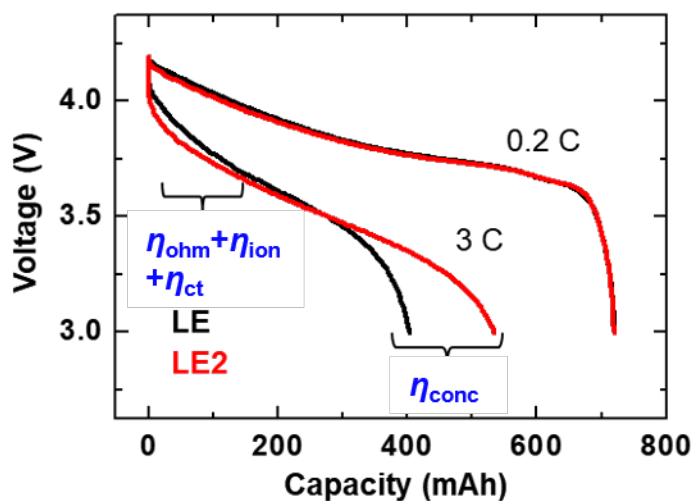


Fig. 5.4 The effect of overpotentials in the electrochemical performance of the cells, adapted from the handouts of the “Electrochemistry” class. η_{ohm} , η_{ion} , and η_{ct} affect at the early stage of discharge process due to the rapid time-scale of ionic conduction and charge transfer reactions while η_{ct} significantly reduces the electrochemical performance at the late time of discharge process due to the cumulative concentration gradient.

5.2 Experimental

5.2.1 Chemicals

LiFSI (purity: 98.0%) was provided by TCI Co., Ltd., TTE (99.0%) was provided by Apollo scientific Ltd.. Anhydrous DMC (99.5%) was purchased from Samchun chemicals. LCO electrode (1.6 mAh, 1.54 cm² area) was provided by Wellcos Corp. The preparation of LiFSI-DMC based electrolytes (1 M LiFSI DMC: DE, 5 M LiFSI DMC: HCE₂ and 2.5 M LiFSI DMC/TTE (1/1, v/v): LHCE) was conducted in an Ar-filled globe box (H₂O and O₂ levels < 1 ppm and 25 ± 5 °C), and their water contents, measured by Karl-Fisher (Metrohm), were less than 35 ppm. LCO electrode and PE separator (Tonen) were dried at 100 °C and 60 °C under vacuum for over 12 h prior to use, respectively.

5.2.2 Methodology

The ionic conductivities of the electrolytes were measured from 10 °C to 60 °C using an ionic conductivity meter (MCS 10, Biologic), and the viscosity of the electrolytes at 25 °C was measured by a viscometer (A&D). Prior to each measurement, the electrolytes were maintained for at least 30 min at a given temperature.

A three-electrode system was employed to determine Al corrosion behaviors of the electrolytes. An Al rod (99.999% purity, 3.0 mm diameter) was used as the working electrode, and a Li chip and Pt wire were employed as the reference and counter electrodes, respectively. To evaluate the oxidative stability of the electrolytes, cyclic voltammetry (CV) was conducted at a scan rate of 10 mV s⁻¹ from 2.7 to 4.7 V (vs. Li/Li⁺).

Battery tests were carried out using 2032-type SUS coin cells (Wellcos Corp.) assembled in an Ar-filled glove box. To prevent SUS corrosion issues at the cathode side, an Al-deposited SUS cell case (Wellcos Corp.) was introduced. For the rate capability test, LCO/Li cells composed of an LCO cathode (1.54 cm²) and a Li foil disk (2.01 cm²) were assembled. The cells were cycled three times at 25 °C with a 0.2 C current within a cutoff voltage range of 2.5–4.25 V to complete the formation process. The current densities for rate capability test were 0.5C, 1C, 2C, 5C, 10C, 15C, and 20C for three cycles, respectively.

GITT was introduced by placing the rest time in the middle of discharge process to eliminate Li salt concentration gradient. LCO/Li cells with DE, HCE, and LHCE were cycled for three times without intermission as the formation process, and then charged at 0.2C. The cells were discharged at 5C with 20 min rest for nine times.

EIS was conducted with LCO/LCO symmetric cells in DE, HCE, and LHCE electrolytes. LCO/LCO coin cells were stored at 25 °C for 20 h after they were assembled with 150 μL of electrolytes and PE separator in the glove box to distinguish the ionic resistance in electrode pores (R_{ion}). After measurement of R_{ion} at SOC 0, the cells were disassembled and each LCO electrode was reused with fresh Li foils (e.g. LCO/Li coin half cells) to complete the three-cycles-formation process which was ended at SOC 50. Electrochemical impedance was then measured for SOC 50 LCO/LCO symmetric cells which were reassembled with three-cycle-cycled LCO/Li coin half cells. For those SOC 50 LCO/LCO cells, the overall impedances can be classified into R_{sol} (bulk electrolyte resistance), R_{hf} (high-frequency resistance related to film, SEI, contact resistance), R_{ion} , and R_{ct} . Especially, R_{ion} can be precisely fitted due to the independence of R_{ion} to the SOC changes^[3] in LCO/LCO cells as shown in

Nyquist plots at SOC 0 and 50 (Fig. 5.5). The frequency range was 300 kHz to 0.1 Hz, and the ac voltage amplitude was 5 mV with no dc potential polarization.

To estimate the Li activity (a_{Li^+}), EMFs of the concentration cell were measured by a portable digital voltmeter in the glove box. The configuration of the concentration cell is illustrated in detail in Fig. 5.6.

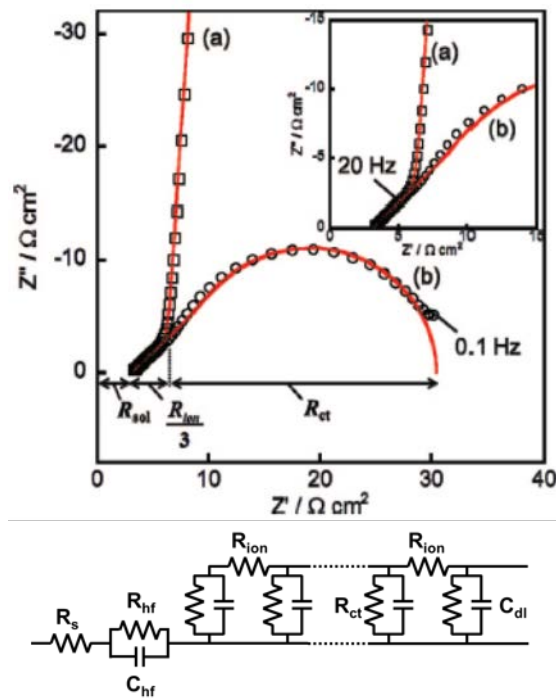


Fig. 5.5 Nyquist plots of LiNiO_2 cathode symmetric cells in the conventional electrolyte at 20°C : (a) SOC 0, and (b) SOC 50. The solid lines are the best-fitted results from the equivalent circuit^[3].

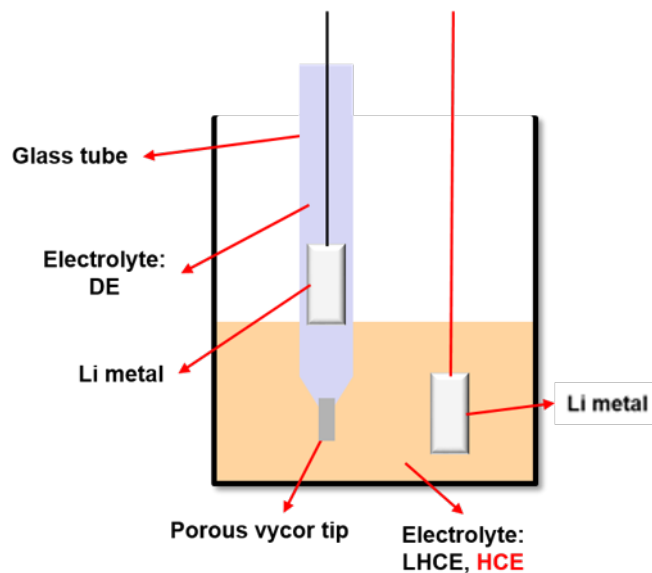


Fig. 5.6 Illustration of concentration cell configuration. Li metal immersed in DE-filled glass tube with porous vycor tip is a reference electrode, and the other Li metal is immersed in HCE or LHCE-filled beaker as a working electrode. EMFs between two Li metals were measured by a portable digital voltmeter.

5.3 Results and discussion

5.3.1 Physicochemical properties

As previously concluded, the physicochemical properties of the electrolyte crucially affect the electrochemical performance of LMBs. Fig. 5.7 and Table 5.3 display the ionic conductivities and activation energy for ionic conduction (E_a^{sol}) at various temperatures and the ionic conductivity and viscosity at 25 °C for DE, HCE, and LHCE.

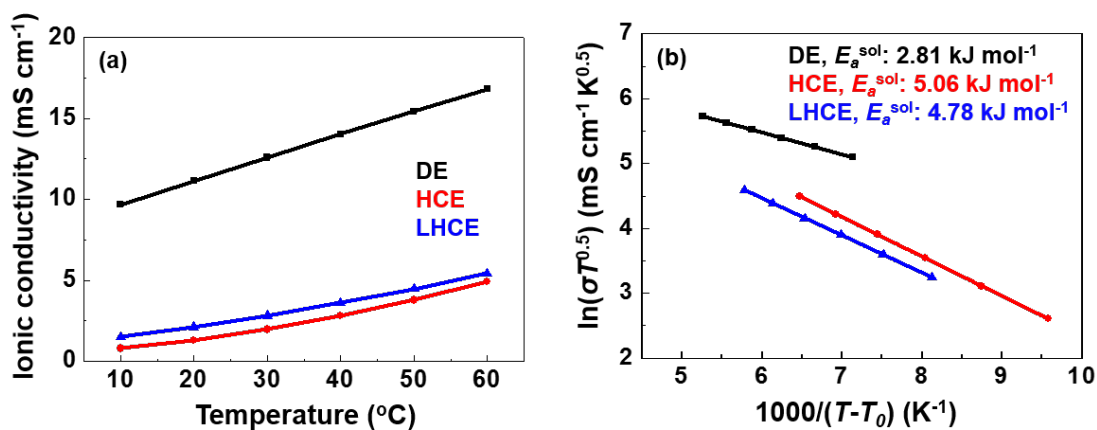


Fig. 5.7 (a) Ionic conductivities of DE, HCE, and LHCE at various temperatures. (b) Vogel-Tamman-Fulcher (VTF) plots of ionic conduction for DE, HCE, and LHCE. Solid lines denote the best-fitting results of the VTF equation.

Table 5.3 Ionic conductivity and viscosity of DE, HCE, and LHCE at 25 °C.

Electrolyte	Ionic conductivity (mS cm ⁻¹)	Viscosity (cP)
DE	12	3.2
HCE	1.7	145
LHCE	2.5	21

DE exhibited superior ionic conductivity and quite lower viscosity, and also the activation barrier for ionic conduction is lowest (2.81 kJ mol^{-1}) among the three electrolytes. Since the ionic conductivity of the electrolyte surely influences the mass transport, large η_{ohm} and η_{ion} (e.g. R_{sol} and R_{ion}) of HCE and LHCE are expected to limit the cell performance. Importantly, LHCE appeared to have better mass transport by the fact that LHCE presented higher ionic conductivity and seven times lower viscosity.

5.3.2 Al corrosion inhibition

Before the electrochemical tests of LCO/Li cells, the oxidation stability of the electrolyte must be guaranteed to separate and interpret the origin of degradation in the cells from the electrolyte decomposition. Fig. 5.8 presents CVs for an Al rod working electrode immersed in the three electrolytes. All CVs exhibited Al corrosion inhibition ability (For the detailed description of corrosion resistive behaviors, see Fig. 3.3 and explanation of Fig. 3.3). Thus, the cells with three electrolytes are not going to suffer from the oxidative decomposition of the electrolytes or Al current collector of cathodes.

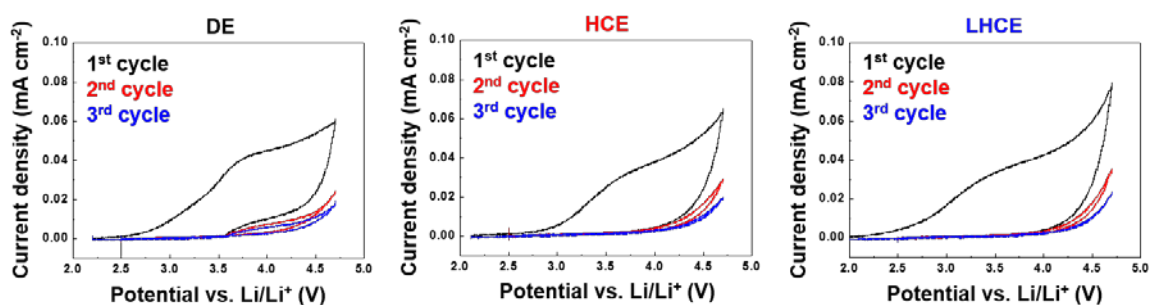


Fig. 5.8 CVs of Al electrodes at the first, second, and third cycle in DE, HCE, and LHCE. The current density decreases in the subsequent cycles after first cycle, which indicates the passive film layer is formed on the Al electrodes.

5.3.3 LCO/Li rate performance

Rate capability of LCO/Li cells with DE, HCE, and LHCE was investigated from the cycling of LCO/Li cells at 0.2C–20C. Fig. 5.9 shows the discharge capacity of LCO/Li cells with DE, HCE, and LHCE. At low rate (i.e. 0.5C), the capacity retentions of HCE and LHCE were superior to DE. The higher capacity retention was observed up to 10C for both HCE and LHCE. However, the discharge capacity at 15C for HCE was dramatically decreased, and even became lower than DE. It is noted that the capacity of LCO/Li cells with LHCE was retained highest as the discharge rate was fastest (20C).

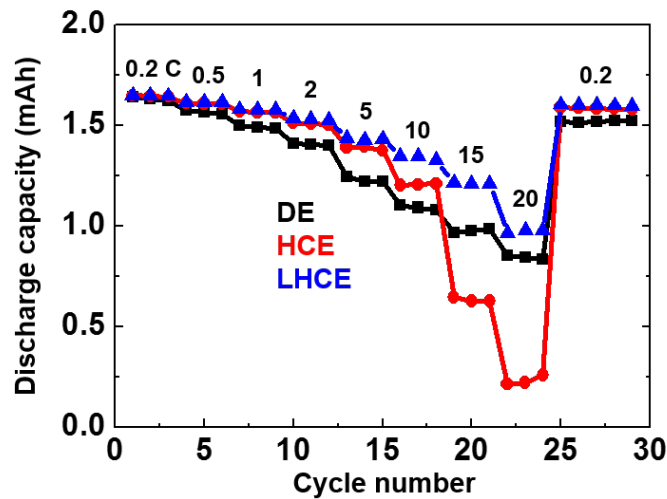


Fig. 5.9 The discharge capacity of LCO/Li cells with DE, HCE, and LHCE at various C-rates from 0.2C to 20C.

Voltage profiles can provide the information about the rapid decrease of discharge capacity retention of HCE at 10C and great capacity retention of LHCE up to 20C. Fig. 5.10 exhibits the voltage profiles of DE, HCE, and LHCE at 0.2C, 5C, 10C, and 20C. No discharge capacity difference among LCO/Li cells with three electrolytes was observed at 0.2C, but the overpotential in HCE increased at 5C, indicating η_{ohm} , η_{ion} , and η_{ct} for HCE increased. These overpotentials became serious, inducing the decrease of discharge capacity and energy density while other two LCO/Li cells with DE and LHCE were governed by much mitigated overpotentials. At 20C, HCE suffered from all the overpotentials including η_{conc} , and thereby huge decrement of discharge capacity was exhibited. LHCE began to be influenced by increased ohmic, ionic, and charge transfer overpotentials but it still

provided higher discharge capacity than DE. However, the exact overpotential change is not able to be separated from the voltage profiles (Namely, the mass transport and kinetics at the early stage of discharge are not distinguishable).

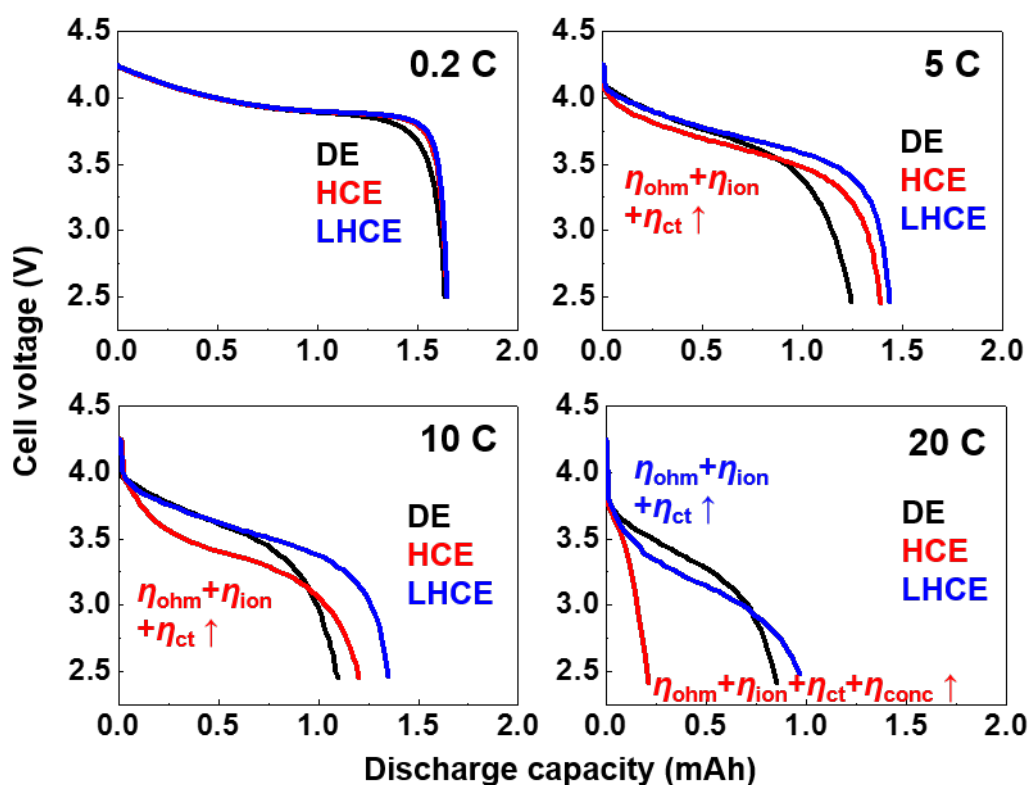


Fig 5.10 Voltage profiles of LCO/Li cells at 0.2C, 5C, 10C, and 20C with DE, HCE, and LHCE.

5.3.4 Internal resistance and overpotential

It was found that DE exhibits most favorable mass transport (e.g. highest ionic conductivity), LHCE shows better migration of ions in the cells than HCE, and η_{ohm} , η_{ion} , and η_{ct} are seriously degrading the rate capability of HCE at higher rate. Since the overall overpotentials of DE at the beginning of discharge were similar to other two electrolytes with lowest η_{ohm} , and η_{ion} , η_{ct} is predicted to contribute to the decrease in discharge capacity at low and moderate rate (0.2C–5C). EIS then gives an insight into the overpotentials, and thus impedance spectra of LCO/LCO symmetric cells with DE, HCE, and LHCE was examined. The spectra and best-fitted resistances are displayed in Fig. 5.11. R_{sol} and R_{ion} in the high frequencies were in the following order: DE \ll LHCE $<$

HCE, which is in good agreement with the ionic conductivities in Table 5.2 and Fig. 5.7. However, R_{ct} was found to be highest in DE and lowest in LHCE, and thus the overall internal resistance is highest in DE. This indicates the capacity retention at low and moderate rate was poor in DE due to the sluggish charge transfer reactions and importantly it seems to be more affected by the kinetics than mass transport because HCE and LHCE presented better capacity retention owing to fine charge transfer reactions.

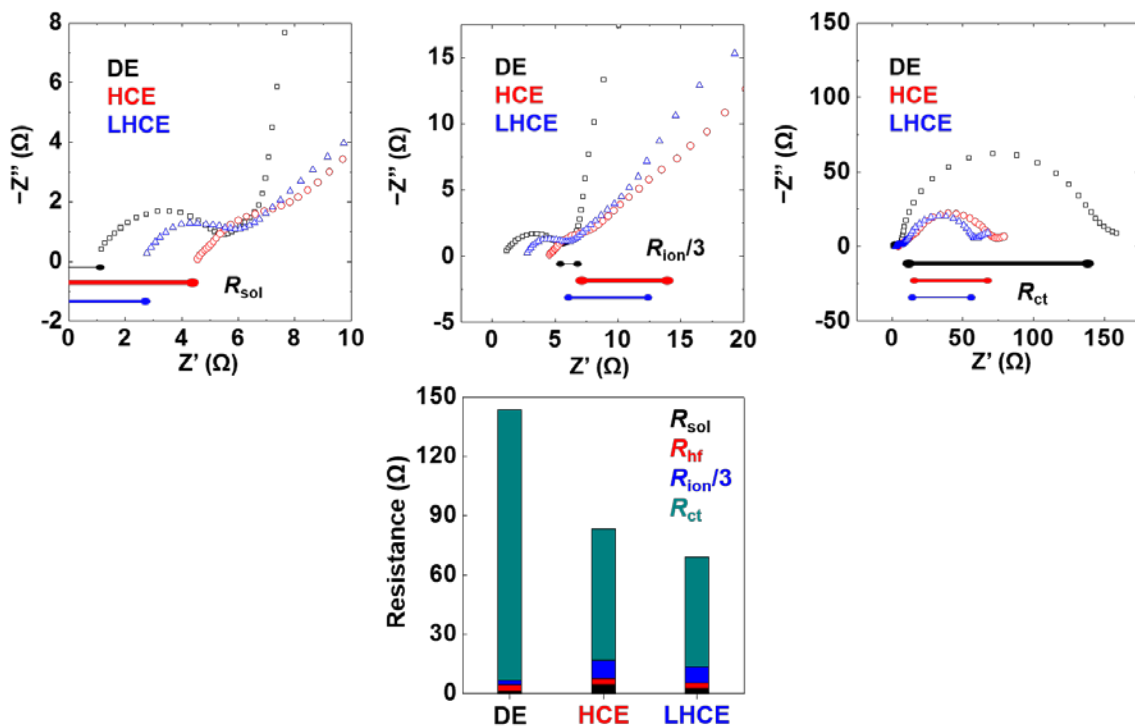


Fig. 5.11 Nyquist plots of LCO/LCO symmetric cells at SOC 50 for DE, HCE, and LHCE. Left and middle are expanded view of right plot. Each resistance is described as a bar with various length and thickness in Nyquist plots and accumulated column bar graph.

Meanwhile, it seems the sophisticated consideration of the origin of charge transfer for HCE and LHCE would be needed, despite poor mass transport, because it considerably affects the electrochemical performances of the cells at moderate rate (~5 or 10C). As mentioned in Table 5.2, the charge transfer is determined by the rate constant such as E_a^{ct} and i_0 from the equation below^[4, 5]:

$$i_o = \frac{RT}{R_{ct}} = \frac{A}{\tau_L} \sqrt{a_{Li^+}} \exp\left(-\frac{\Delta G^*}{RT}\right)$$

where R is a gas constant, A is the solvent-independent pre-exponential factor, τ_L is the longitudinal relaxation time of the solvent which is proportional to the viscosity by the relation of Stokes-Einstein-Debye equation, a_{Li^+} is Li-ion activity, and ΔG^* is the activation energy for charge transfer. To compare the kinetics quantitatively, the ratio of i_o is calculated from R_{ct} ratio as displayed in Table 5.4.

Table 5.4 The ratio of $i_{o,HCE}$ to $i_{o,LHCE}$ from R_{ct} .

Electrolyte	R_{ct} (Ω)	$i_{o,HCE}/i_{o,LHCE}$
HCE	66.1	0.84
LHCE	55.6	

The ratio of $i_{o,HCE}$ to $i_{o,LHCE}$ is revealed to 0.84, standing for the better kinetics of LHCE than HCE. This better kinetics of LHCE must be coming from the relation between viscosity, a_{Li^+} , and ΔG^* . Thus, the confirmation of the same exchange current ratio calculated from these parameters will guarantee the better kinetics of LHCE and the exact origin of it. For the calculation of the i_o ratio, the ratio of viscosity, a_{Li^+} , and ΔG^* need to be calculated. Thus, R_{ct} of LCO/LCO symmetric cells with HCE and LHCE at various temperatures was measured and Arrhenius plot is displayed in Fig. 5.12. First of all, the better kinetics of LHCE was ascertained by the result that E_a^{ct} of LHCE (note that E_a is the rate constant depending on the kinetics) was revealed to be lower than HCE, and the ratio of $\exp(-E_a^{ct,HCE}/RT)$ to $\exp(-E_a^{ct,LHCE}/RT)$ was 0.35.

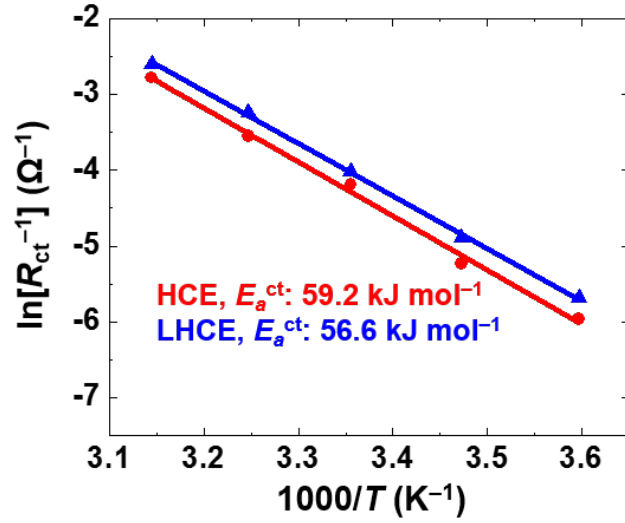


Fig. 5.12 Arrhenius plots for E_a^{ct} of HCE and LHCE. The solid lines are the best-fitted result from the equivalent circuit in Fig. 4.16c.

Next, to assess the ratio of $\tau_{L,HCE}^{-1}$ to $\tau_{L,LHCE}^{-1}$, the viscosity ratio of $\text{viscosity}_{HCE}^{-1}$ to $\text{viscosity}_{LHCE}^{-1}$ was calculated to be 0.15. Lastly, a_{Li^+} ratio was estimated from EMFs of the concentration cells by the following equation adapted from the handouts of “Electrochemistry” class.

$$EMF = \frac{2(1-t_+)RT}{F} \ln \frac{a_{Li^+}}{a_{Li^+_{ref}}}$$

where t_+ is the Li-ion transference number, $a_{Li^+_{ref}}$ is the Li-ion activity in the reference electrolyte (DE). The EMF of Li electrode in HCE and LHCE against the Li metal in DE reference electrolyte was measured to be 0.43 V and 0.29 V by a portable voltmeter, respectively. Assuming t_+ of HCE and LHCE, such solvated ionic liquids[5], to be 0.5, $a_{Li^+}/a_{Li^+_{ref}}$ is $\exp(EMF \cdot F/RT)$. Thus, the ratio of $a_{Li^+,HCE}$ to $a_{Li^+,LHCE}$ is equal to the ratio of $\exp(EMF_{HCE} \cdot F/RT)$ to $\exp(EMF_{LHCE} \cdot F/RT)$, which is calculated to be 15.6. Therefore, the ratio of $i_{o,HCE}$ to $i_{o,LHCE}$ is a product of these three ratios and it is eventually calculated to be 0.80, leading to very good agreement with the exchange current ratio from R_{ct} (Table 5.5).

Table 5.5 The ratio of $i_{o,HCE}$ to $i_{o,LHCE}$ from E_a^{ct} of LCO/LCO symmetric cells with HCE and LHCE, viscosity, and EMF of the concentration cells. i_o ratio is obtained by a product of all factor ratios.

Factor	Relation	Calculated ratio (HCE/LHCE)
$\exp(-E_a^{ct}/RT)$	E_a^{ct}	0.35
Viscosity ⁻¹	τ_L	0.15
$\exp(EMF \cdot F/RT)$	a_{Li^+}	15.6
i_o	kinetics	0.80

In summary, the better kinetics of LHCE compared to HCE is attributed to lower activation energy for charge transfer reaction, considerably lower viscosity of the electrolyte, and therefore higher rate constant than HCE, resulting in the better capacity retention up to moderate rate (~10C).

The effect of η_{conc} on the electrochemical performance of the cell was already confirmed in the voltage profiles in Fig. 5.10: largest η_{conc} for HCE. As shown in Fig. 5.13, the discharge capacity was, indeed, recovered by reducing the Li salt concentration gradient (e.g. η_{conc}) using GITT method in LCO/Li cells. The recovery was largest in HCE, and smallest in DE, which means the mass transport caused by Li salt concentration difference owing to the poor diffusion of HCE seriously diminished the capacity retention at high rate (> 15C) and thereby the energy density of the cells.

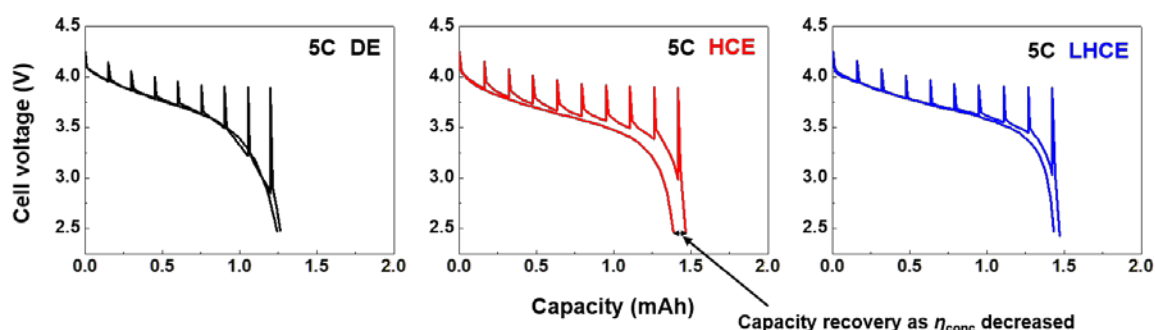


Fig. 5.13 Voltage profiles of LCO/Li cells at 5C with DE, HCE, and LHCE using CC only and GITT method.

The intermittent rest time is 20 min.

5.4 Conclusions

The relation between the characteristics of the electrolyte and the rate capability of cells was assessed by utilizing LiFSI-DMC DE, HCE, and LHCEs with electrochemical techniques including EIS, electromotive force (EMF) of concentration cells, and galvanostatic intermittent titration technique (GITT). Despite the poor mass transport of HCE, the rate capability of LCO/Li cells with HCE exhibited quite better than DE at moderate C-rate because HCE presented much mitigated charge transfer overpotential as compared to DE, which means for better electrochemical performance of the cells the facile charge transfer should be basically guaranteed. Especially, LHCE exhibited the best charge transfer due to the lowest activation energy for charge transfer reaction and lower viscosity of the electrolyte.

However, at very high rate, HCE suffered from mass transport limit conditions, so the capacity retention was very poor at 15C. LHCE had strong advantages at such high rate since it has not only the lowest charge transfer overpotential but also much better physicochemical properties which is closely related to the mass transport of the cells. Lastly, the Li concentration gradient (e.g. concentration overpotential) was obviously confirmed to reduce the capacity retention and the energy density of the cells especially in HCE. Thus, the optimized LHCE was eventually recommended owing to much improved mass transport as well as the facile charge transfer in the cells.

5.5 References

- [1] Y. Yamada, K. Furukawa, K. Sodeyama, K. Kikuchi, M. Yaegashi, Y. Tateyama, A. Yamada, Unusual stability of acetonitrile-based superconcentrated electrolytes for fast-charging lithium-ion batteries, *J. Am. Chem. Soc.* 136 (2014) 5039–5046.
- [2] N. Ogihara, Y. Itou, T. Sasaki, Y. Takeuchi, Impedance spectroscopy characterization of porous electrodes under different electrode thickness using a symmetric cell for high-performance lithium-ion batteries, *J. Phys. Chem. C* 119 (2015) 4612–4619.
- [3] N. Ogihara, S. Kawauchi, C. Okuda, Y. Itou, Y. Takeuchi, Y. Ukyo, Theoretical and experimental analysis of porous electrodes for lithium-ion batteries by electrochemical impedance spectroscopy using a symmetric cell, *J. Electrochem. Soc.* 159 (2012) A1034–A1039.
- [4] Y. Kato, T. Ishihara, Y. Uchimoto, M. Wakihara, Charge-transfer reaction rate of Li^+/Li couple in poly(ethylene glycol) dimethyl ether based electrolytes, *J. Phys. Chem. B* 108 (2004) 4794–4798.
- [5] J. Xu, G. C. Farrington, A microelectrode study of lithium electrokinetics in poly(ethylene glycol dimethyl ether) and 1,2-dimethoxyethane, *J. Electrochem. Soc.* 142 (1995) 3303–3309.

요 약 문

전극과의 계면 반응에서 리튬 이온 전지 및 리튬 금속 전지용 이미드 전해액의 역할

본 논문은 리튬 이온 전지 및 리튬 금속 전지에서 리튬 이미드 염 기반 전해액의 가용성에 대해 연구이다. 리튬 이미드 염, 그 중에서도 lithium bis(fluorosulfonyl)imide (LiFSI)나 lithium bis(trifluoromethanesulfonyl)imide (LiTFSI) 등의 경우 lithium hexafluorophosphate (LiPF₆)보다 우수한 용해도, 열적 안정성, 좋은 이온 전도도와 HF 형성으로 인한 문제점이 없다는 다양한 장점들로 인해 리튬 이온 전지 및 리튬 금속 전지에서의 활용방안이 무궁무진하다. 따라서 본 논문은 상기된 장점을 가진 리튬 이미드 염을 활용하여 리튬 이온 전지 및 리튬 금속 전지에 적용하고 분석을 진행하였다. 이를 정리하면 다음과 같다.

우선적으로 리튬 이온 전지에서 리튬 이미드 염의 적합성에 대해 연구하였다. 상기된 다양한 장점에도 불구하고 리튬 이미드 염은 양극의 집전체인 알루미늄의 부식 문제가 심하기 때문에 활용에 큰 제한을 받고 있다. 리튬 이미드 염 기반 전해액 및 다양한 리튬 보레이트 염 첨가제를 사용한 전해액에서의 체계적인 알루미늄 부식 거동 비교를 통해 알루미늄 부식 이 첨가제들에 의해 크게 감소하였으며, 부식 억제 능력은 다음 순서를 따른다. Lithium difluoro(oxalato)borate (LiDFOB) > lithium tetrafluoroborate (LiBF₄) ≈ LiPF₆ > lithium bis(oxalato)borate (LiBOB). 특히, LiDFOB 첨가제를 사용한 리튬 이미드 전해액의 부식 억제 능력은 알루미늄 부식이 없는 LiPF₆ 전해액과 유사하였다. X-ray photoelectron spectroscopy (XPS)를 통한 표면 분석에 의하면 LiDFOB의 우수한 부식 억제 능력은 알루미늄/전해액 계면 상에 Al-F, Al₂O₃, B-O 화합물로 이루어진 피막을 형성하기 때문으로 밝혀졌다. 이 전해액을 활용하여 LiCoO₂/흑연 전지의 율속 특성을 분석한 결과 LiPF₆와 비교 될만한 율속 성능을 보였으며, LiDFOB가 첨가되지 않은 LiFSI 전해액을 사용한 전지는 심각한 알루미늄 부식으로 인해 출력 특성이 좋지 못함을 확인하였다.

한편, 리튬 금속 음극은 높은 이론 용량 및 낮은 레독스 전위를 가지므로 낮은 쿨롱 효율과 덴드라이트 형성으로 인한 안전성 문제만 해결되면 급속도로 발전하는 에너지 시장 수요를 당장에 충족시킬 수 있는 흑연 음극의 대체제로서 각광받고 있다. 최근 리튬 이미드 염과 비용매 불화 에테르 용매를 활용한 전해액이 우수한 리튬 수명 성능을 가진다는 보고가 있었으나, 이러한 국부 고농도 전해액 (LHCE)의 보다 거친 조건 하에서 성능을 규명하는 연구는 거의 없는 실정이다. 따라서, 본 논문에서는 넓은 온도 범위에 걸친 글라임 계 LHCE (gLHCE)의 성능을 불화 에테르의 유익한 역할에 초점을 맞춰 분석하였다. 글라임 계 고농도

전해액 (gHCE)과 비교하여 gLHCE 는 불화 에테르의 혼용을 통해 우수한 물성, 젖음성, 난연성 등의 장점을 가진다. 상세 분석들을 통해 gLHCE 는 대부분의 FSI 음이온들이 접촉 이온 쌍 및 agglomerate 형태로 존재하여 리튬 음극 상에 무기물이 풍부한 solid electrolyte interphase (SEI)를 형성함으로써 전해액과의 부반응을 줄임과 더불어 내부 전하 이동 또한 용이하게 만듦을 밝혀냈다. 이러한 표면 피막의 우수성 때문에 gLHCE 는 뛰어난 리튬 수명 성능 및 FeS₂/Li, 음극이 없는 LiFePO₄/Cu 전지 등에서의 저온 및 고온 장기 수명 안정성 확보를 가능하게 하였다.

뿐만 아니라, 통상적으로 더 높은 이온 전도도와 낮은 점도를 갖는 전해액에 비해 고농도 전해액 (HCE)는 전기화학적 성능이 좋지 못할 것이라는 생각과는 달리 HCE 에서 우수한 율속 특성이 나타난다는 보고를 토대로 디메틸 카보네이트 (DMC) 기반의 저농도 전해액 (DE), HCE, 그리고 LHCE 에 대해 율속 특성을 파악하였다. 이어서 다양한 종류의 과전압을 분류하고 전기화학적 임피던스 분석 및 농도차전지의 기전력 측정, 충방전 프로파일 분석, galvanostatic intermittent titration technique (GITT) 등을 통하여 각 전해액에서의 LCO/Li 전지가 갖는 과전압의 영향력을 파악하였다. 고속 방전 하에서도 가장 우수한 율속 특성을 보인 LHCE 의 경우 가장 낮은 전하 이동 과전압 및 상대적으로 낮은 물질 전달 과전압을 보유하고 있었으며, 이를 통해 율속 특성에 영향을 미치는 과전압은 물질 전달 과전압 뿐만 아니라 두 종류의 과전압이 모두 낮아야 함을 규명하였다.

상기 리튬 이온 전지 및 리튬 금속 전지 분야 본 연구에서는 전지용 전해액의 활용 가능성은 전해액 자체의 물성만의 영향보다는 이온 및 전하 이동에 영향을 줄 수 있는 전극 및 전극/전해액 계면의 특성 또한 종합적으로 고려해야 한다는 결론을 도출하였다.

핵심어: lithium bis(fluorosulfonyl)imide (LiFSI), lithium ion batteries, lithium metal batteries, passive layer, solid electrolyte interphase (SEI), interface